4-30-2018

p-TypeE InAs/GaAs Quantum Dot, Dot-In-Well, and Low-Frequency Noise Properties of Infrared Photodetectors

Seyoum G. Wolde
Georgia State University

p-TYPE InAs/GaAs QUANTUM DOT, DOT-IN-WELL, AND LOW-FREQUENCY NOISE PROPERTIES OF INFRARED PHOTODETECTORS

by

SEYOUM G. WOLDE

Under the Direction of Prof. A. G. UNIL PERERA

ABSTRACT

Several types of *p*-doped Infrared detectors were studied. These include InAs/GaAs quantum dot (QDIP), and dots-in-well (DWELL) and split off band-based heterojunction detectors. In these structures, IR absorption leading to detection is based on valence-band inter-sublevel hole transitions. For a QDIP and DWELL, at 80 K, two response bands observed at 1.5 – 3 and 3 – 10 μm were identified as due to optical transitions from the heavy hole to spin–orbit split-off QD level and from the heavy-hole to heavy/light-hole level, respectively. Unlike the *n*-type with bias dependent spectral response, the *p*-type hole response displays a well-preserved spectral profile (independent of the applied bias) observed in both QDIP and DWELL detectors. At a response peak of ~ 5.2 μm, QDIP and DWELL exhibit an external quantum efficiency of 17 % and 9 % respectively. At elevated temperatures between 100 and ~120 K (for QDIP), 130 K (for DWELL), both QDIP and DWELL detectors exhibit a strong far-infrared or terahertz (THz) response up to 70 μm which show promising potential of *p*-type QDs for developing THz infrared photodetectors.

Based on the dark current and noise power spectral density analysis, structural parameters such as the numbers of active layers, the surface density of QDs, and the carrier capture or relaxation rate, type of material and electric field are some of the optimization parameters identified to improve the photoconductive and dark current gain of detectors. The capture

probability of DWELL is found to be more than two times higher than the corresponding QDIP. Based on the noise analysis, QDs based structures suppressed phonon scattering and enhanced carrier life time or photoconductive gain. Furthermore, in a GaAs/$Al_xGa_{1-x}As$ heterostructure, for a given width of $A_xlGa_{1-x}As$ barrier, the barrier thickness can be varied by varying the Al mole fraction *x*, which is referred to as a graded barrier. Grading the barrier and optimizing the emitter thickness of GaAs/AlGaAs heterostructures enhance the absorption efficiency, the escape probability and lower the dark current; hence, enhances the responsivity and specific detectivity of detectors.

The two important methods (Arrhenius plot and Temperature Dependent Internal photoemission (TDIPS)) of determining detectors threshold wavelengths or band offsets were compared. For detectors with long threshold wavelength (>> 9.3 μm), the Arrhenius plot used to extract activation energy leads to energy values with deviation higher than ~ 10 % from the corresponding TDIPS values and results from the temperature dependent Fermi distribution tailing effect and Fowler–Nordheim tunneling current. Therefore, TDIPS or other methods, that take the temperature effects on the band offset and Fowler–Nordheim tunneling current into account, are needed for a precise band offset characterization of a long threshold wavelength detectors.

INDEX WORDS: Quantum dot, Quantum dot-in-well, Terahertz, Noise, Gain, Capture probability, Activation energy.

p-TYPE InAs/GaAs QUANTUM DOT, DOT-IN-WELL, AND LOW-FREQUENCY NOISE PROPERTIES OF INFRARED PHOTODETECTORS

by

SEYOUM GIRMA WOLDE

A Dissertation Submitted in Partial Fulfillment of the Requirements for the Degree of

Doctor of Philosophy

in the College of Arts and Sciences

Georgia State University

2018

p-TYPE InAs/GaAs QUANTUM DOT, DOT-IN-WELL, AND LOW-FREQUENCY NOISE PROPERTIES OF INFRARED PHOTODETECTORS

by

SEYOUM G. WOLDE

Committee Chair: A. G. Unil Perera

Committee: Vadym Apalkov

Alexander Kozhanov

Douglas R. Gies

Steve T. Manson

Electronic Version Approved:

Office of Graduate Studies

College of Arts and Sciences

Georgia State University

May 2018

DEDICATION

This dissertation is dedicated to my mom Aselefech Desalegn Woldeyes, to my Dad Girma Wolde Habtewolde, and to my wife (Queen) Misrak T. Gebremichael. My mom, Dad, and my wife, it is a blessing to have all of you in my life and next to me all the time. Thanks to God.

ACKNOWLEDGEMENTS

I would like to express my gratitude to my supervisor Dr. Unil Perera for his guidance and encouragement throughout this study. Deepest gratitude is also expressed to the members of my dissertation committee: Dr. Vadym Apalkov, Dr. Alexander Kozhanov, Dr. Douglas Gies, and Dr. Steve Manson for fruitful discussions, technical assistance, and effort in reading and providing me with comments. I wish to thank Dr. Sanjay Krishna and his group in University of New Mexico for their help in the growth of the quantum dot and dot-in-well samples, and Dr. L. H. Linfield and his group for their help in the growth of the GaAs/AlGaAs samples.

I would like to convey special acknowledgement to former members and colleagues, Dr. Yang-Feng Lao, Dr. Jito Titus, Dr. Sanjib Kabi, and Dr. Divya Somvansi and present colleagues in the group, Mr. Dilip Chauhan, Mr. Hemendre Ghimire, Mr. Sameera Kelum, and Mr. Nurul Azam for valuable discussions on the subject matter. I wish to thank all the individuals of the Department of Physics, and friends for their contribution, and friendship.

I also acknowledge funding agencies as: this material is based upon work supported in part by, the U. S. Army Research Laboratory and the U. S. Army Research Office under contract/grant numbers W911NF-15-1-0018 and W911NF-12-2-0035, and the US National Science Foundation under grant numbers ECCS-1232184 to Dr. Perera. We are also grateful for support from the UK's EPSRC (EP/E048811/1), the European Research Council program 'TOSCA' (247375), the Wolfson Foundation, and the Royal Society for support of Dr. Linfield at the School of Electronic and Electrical Engineering, University of Leeds. The Shanghai group (Y. H. Zhang and T. M. Wang) acknowledges supports from the 863 Program of China (2011AA010205) and the Natural Science Foundation of China (91221201, 61234005, and

11074167). A fellowship provided by The Center for Diagnostics and Therapeutics, at Georgia State University, to Seyoum Wolde is also acknowledged.

TABLE OF CONTENTS

LIST OF TABLES

LIST OF FIGURES

LIST OF ABBREVIATIONS

- 1D, 2D, and 3D – One-, Two-, Three- Dimensional
- AFM – Atomic Force Microscope
- AlAs – Aluminum Arsenide
- $Al_xGa_{1-x}As$ - Aluminum Gallium Arsenide, x- Aluminum mole fraction
- AlGaN – Aluminum Gallium Nitride
- BC - Bottom Contact
- BLIP – Background Limited Performance
- CB - Conduction Band
- CdSe – Cadmium Selenide
- CQD – Colloidal Quantum Dot
- C-V-T – Capacitance-Voltage-Temperature
- DC - Direct Current
- DOS – Density Of State
- DUT – Device Under Test
- DWELL - Quantum Dot-in-Well Infrared Photodetector
- D* - Specific Detectivity
- e – Electronic charge
- eV - Electron Volts
- FD – Fermi-Dirac
- FE – Field Emission
- FN – Fowler-Nordheim

- FFT – Fast Fourier Transform
- FIR - Far-Infrared
- FTIR - Fourier Transform Infrared
- FTE – Field assisted Thermal Emission
- FP – Frenkel-Poole
- FWHM – Full Width Half Maximum
- Ge/Si – Germanium/Silicon
- g - Photoconductive Gain
- h – Planck constant
- GaAs - Gallium Arsenide
- GaIn – Gallium Indium
- GaInSb – Gallium Indium Antimony
- GaN – Gallium Nitride
- G-R - Generation-Recombination
- GaSb – Gallium Antimony
- HEIWIP - Heterojunction Interfacial Work Function Internal Photoemission
- HH - Heavy Hole
- InAs - Indium Arsenide
- InAlAs – Indium Aluminum Arsenide
- InGaAs - Indium Gallium Arsenide
- InP – Indium Phosphide
- IVB - Inter-Valence Band
- I-V-T - Current-Voltage-Temperature

- IR – Infrared
- LA – Longitudinal Acoustic
- LO – Longitudinal Optic
- LH - Light Hole
- LFN - Low-Frequency Noise
- LWIR – Long Wavelength Infrared
- HgCdTe – Mercury Cadmium Telluride
- MBE - Molecular Beam Epitaxy
- MCT – Mercury Cadmium Telluride
- MIR - Mid- Infrared
- ML - Mono-Layer
- MOCVD - Metal-Organic Chemical Vapor Deposition
- MOST - Metal Oxide Semiconductor Transistor
- NIR - Near Infrared
- *n*-type – free electron charge carrier
- PbS – Lead(II) Sulfide
- PSD – Power Spectral Density
- PtSi – Thallium Silicon
- *p*-Type – free Hole charge carrier
- R – Responsivity
- $\mathcal{R}$ - Resistance
- QD - Quantum Dot
- QDIP - Quantum Dot Infrared Photodetector

- QE – Quantum Efficiency
- QWIP - Quantum Well Infrared Photodetector
- SO - Spin-Orbit Split-off band
- SK - Stranski–Krastanov
- TC - Top Contact
- TE – Thermal Emission
- TEF – Thermal assisted Field Emission
- THz – Terahertz
- Ti/Pt/Au – Thallium/Platinum/Gold
- T-QDIP - Tunneling Quantum Dot Photodetector
- T-rays – THz Radiation
- VB - Valence Band
- XTEM - Cross-section Transmission Electron Microscopy

1 *p*-TYPE InAs/GaAs QUANTUM-DOT AND DOT-IN-WELL INFRARED PHOTODETECTORS

1.1 Introduction

Infrared (IR) radiation is electromagnetic radiation invisible to the human naked eye of a wavelength longer than that of visible light, shorter than that of micro waves[1]. Infrared detection is important for a variety of applications, ranging from commercial applications in astronomy, industry, and public safety, to defense applications. In the IR detection, the most common IR imaging technology is based on bulk narrow band-gap HgCdTe.[2, 3] The HgCdTe ternary alloy is close to an ideal IR detector material system due to three reasons[4]: composition dependent tailorable energy band gap over entire 1 - 25 μm range, large optical coefficient that enables high quantum efficiency (QE), and a favorable inherent recombination mechanism that leads to long carrier life time and high operating temperature. However, these II–VI semiconductor materials are difficult in epitaxial growth, detector processing, and uniformity, which results in high cost. Therefore, various alternative technologies and materials, such as those based on quantum dots, have been investigated. Quantum dots (QDs) are nanostructures with dimensions smaller than de Broglie wavelength of electrons or holes or three-dimensional (3D) quantum confinement of carriers.

Generally, there are two groups of quantum dots. The first is colloidal QD (CQD), such as CdSe and PbS.[5-7] This method usually involves nucleation and growth of particles in the vapor phase or in solutions. The CQD can be synthesized in various sizes and forms. The CQD have a dimension of 3-5 nm in diameter and their emission or absorption occurs in the visible or near IR region depending on the size of the QDs. The second type is epitaxial QDs, such as InAs, that are self-assembled nano-structures grown by molecular beam epitaxy (MBE) or metal organic

chemical vapor deposition (MOCVD) through the Stranski–Krastanov (SK) growth mode.[8, 9] The epitaxial QDs have dimensions usually ~ 20 - 40 nm in base and ~ 5 - 8 nm in height,[10, 11] and absorptions and/ or emissions are from near infrared (NIR) through far infrared (FIR) regions.

QDs exhibit discrete energy levels (atomic-like properties) within the conduction and valance bands, and delta-function-like density of states (DOS) which suppress electron (or hole)-phonon scattering[12] and enhance overlap of wave functions.[13, 14] These quantum confinements of energy levels open a new area of possibilities for unipolar detectors sensitive to a broad wavelength range from mid-infrared (MIR) through terahertz (THz).[15, 16] The advances of research and technology in epitaxially grown semiconductor QDs pave ways to optoelectronics detectors such as the quantum dot infrared photodetector (QDIP) and quantum dot-in-a-well infrared photodetector (DWELL) for the mid-wave and long-wave infrared applications.[17, 18]

Studies have reported that QDIPs are capable of operating at elevated temperatures,[18-20] which, however typically leads to detectors operation responding in the mid-wave infrared regime. The development of Terahertz sources[21] and progress required Terahertz detectors. Detectors in THz region have huge potential of applications to biological imaging, chemical, gas sensing, and bimolecular, etc. characterization. For example, a detector responding in THz region (T-rays) has the ability to penetrate through the living body like X-rays do, but unlike X-rays they will not damage cells or DNA, so THz radiation is intrinsically safe, non-destructive and non-invasive.[1]

One of the difficulties lies in the absorption of THz radiation corresponding to very small energy which is typically about 4.1- 41 meV (1-10 THz), below the range of thermal energy for room temperatures ~300 K (25.8 meV). The dark current at temperatures, as high as 78 K is dominant over the photocurrent in the lower energy range of THz detection. Therefore, THz

detectors are very sensitive to temperature variation and are usually unable to operate at high temperatures. For instance, most of the terahertz detectors in the range of ~ 3 - 10 THz operate at low temperatures (4.6 K to 80 K).[10, 22, 23] In this chapter, I investigate *p*-type In(Ga)As/GaAs QDIP and DWELL MIR and THz detectors with a response up to ~ 4.28 THz (~70 μm) operating at 130 K.

Most detectors with QDIP and DWELL structures are based on the intersubband transitions from ground state of the QD to an excited state close to the barrier or GaAs band edge.[10, 24] The bound to continuum transitions have an escape probability of ~ 100 % for photoexcited carriers and lead to a high photocurrent at lower bias. On the other hand, due to better wave function overlap between the two states, the bound to bound transitions have better absorption coefficients, but lower escape probability at lower biases. For any THz detector, the transition energy between the two states should fall in the THz energy range of 4.1 – 41 meV[25, 26] (1 – 10 THz). To match the excited state with the continuum and have the energy spacing between the states in the terahertz region, the width and height of the well, and the size and shape of the QD must be adjusted. The ground and excited state energies can be tuned by changing the width and height of the well. However, in practice, size of a QD is very limited due to the inability to make the dot size as desired in Stranski-Krastanov (SK) growth mode[8]. An alternative approach for small energy spacing in a terahertz QD based detector is a *p*-type-doped structure, which has higher density of states as compared to its *n*-type counterpart. Moreover, at a given temperature, a higher effective mass of holes in the valence-band will result in lower hole transport as compared to the electrons in conduction band and, consequently, a reduction in dark current.[27, 28]

Most of the THz investigations thus far have been made with *n*-type QDIP and used resonant tunneling[29] or dark current blocking layers.[8] Using dark current blocking layers, an *n*-

type Tunneling quantum dot photodetector (T-QDIP) operating at 150 K with spectral response up to ~ 55 μm[29] in THz region and a Quantum ring detector operating at 120 K with spectral responses up to ~ 30 μm have been reported.[23] So far, little or no attention has been paid to *p*-type QDIP/DWELL structures responding in the THz region. Therefore, the motivation of this work is to achieve THz *p*-type QDIP and DWELL detection up to ~ 4.28 THz (~ 70 μm) at an operating temperature of 130 K or higher.

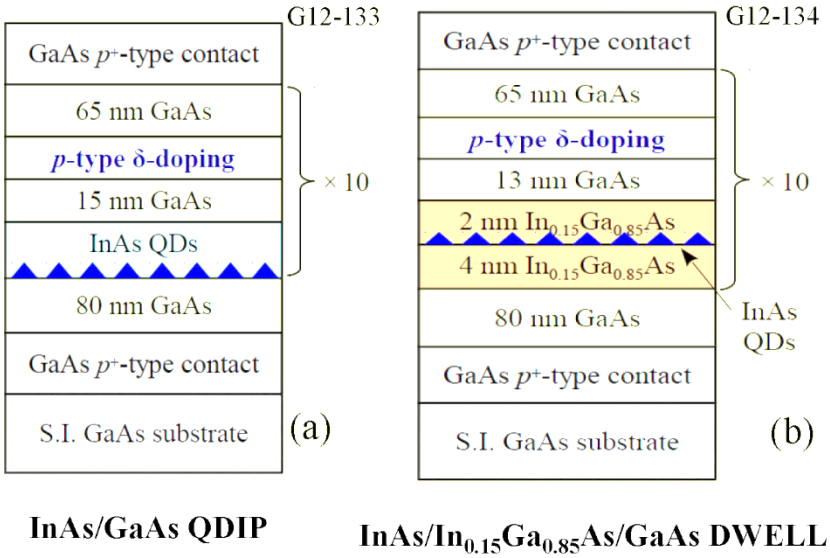

Figure 1.1 Schematics of the *p*-type detector heterostructures for (a) QDIP labeled as G12-133 and (b) DWELL labelled as G12-134. Free holes are introduced into QDs by δ-doping above the QD layer.

Here I investigate, MIR and a THz QDIP and DWELL detectors based on *p*-type intersubband transition, where the InAs dots are placed in $In_{0.15}Ga_{0.85}As$ (in the case of DWELL) which in turn is positioned in a GaAs matrix as shown in Figure 1.1 (a) and (b). Figure 1.2 shows a 3D architectural design of the detector. The measured responsivity shows that as the temperature changes from ~ 100 K to 130 K, the longer wavelength (> 14 μm) responses increase while MIR (3- 10μm) responses decrease. Comparison of the calculated hole energy

levels in QD as shown in Figure 1.3 with the measured spectral response shows that the MIR response peak at ~ 5.2 μm corresponds to a transition of heavy holes from the ground state to the quasi-bound or continuum state.[30] The THz response at high temperature is attributed to the transitions from the excited state to quasi-bound state or continuum. The probability of occupying excited states increases with increasing temperature. The excited states have a higher degeneracy than the ground state. Hence, despite the low occupation probability, the total number of carriers in excited states are comparable to that of the ground states at higher temperatures.[11] Furthermore, for the same incident power, there are more photons at 32.6 μm than at 5.4 μm. Therefore, as the temperature increases from ~ 100 K to 130 K, due to

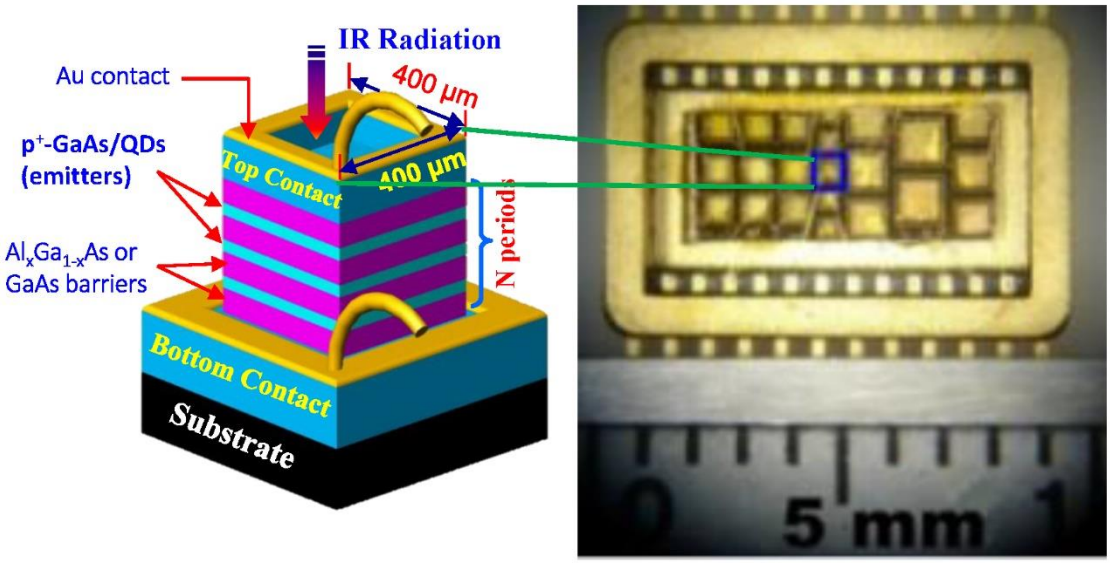

Figure 1.2 A 3D architectural design with a real picture of detectors in a wafer. The optical window at the top is 260 × 260 μm^2.The absorbers are either *p*-type InAs QDs with a GaAs barrier or *p*-type GaAs with an $Al_xGa_{1-x}As$ barrier.

broadening of Fermi-Dirac distribution, carriers will have appreciable concentrations at higher energy levels and leads to the THz response.

1.2 Detector structures and growth

The *p*-type detector structures, shown in Figure 1.1 (a) and (b) were grown by molecular beam epitaxy (MBE) which consists of 10 stacks of QDIP or DWELL structures sandwiched between two highly doped p^+-GaAs contact layers, grown on a semi-insulating GaAs substrate.[30, 31] The active region contains InAs QDs (placed in a 6-nm thick $In_{0.15}Ga_{0.85}As$ QW in the case of DWELL), which in turn was surrounded by GaAs barrier layers. The dot density was about 5×10^{10} cm^{-2}. A δ-doping (two-dimensional doping) technique was used, with a sheet density of 5×10^{11} cm^{-2} *p*-type dopants placed above the QDs layer, (with a 15 and 13 nm thick GaAs spacer for QDIP and DWELL, respectively) which introduce about 10 free holes in each QD. The QDs have nearly pyramidal shape with the average base widths of ~ 20 - 25 nm and height of ~ 5 nm.[10]

1.2.1 QDs Growth by MBE

Molecular beam epitaxy is a process in which an epitaxial layer is formed on a substrate of a different material. Ge/Si, InAs/GaAs, InAs/InP, GaN/AlGaN, InP/GaAs, and InAlAs/AlGaAs are some of the typical examples of epitaxial layer and substrate combinations. The lattice mismatch between the epitaxial layer, and substrate can lead to the growth of a strained layer. In the process of layer-by-layer film growth, the strain accumulated in the epitaxial layer will reach maximum value for a certain critical thickness, beyond which the growth mode switches from 2D film to 3D islands (QDs). This self-assembled QDs growth mode is known as the Stranski-Krastanov (SK) mode. As the thickness increases, the strain build up in the layer at critical thickness leads to instability and favors a release of the strain by transforming from 2D to 3D or island formation.[32, 33]

SK mode epitaxial growth of QDs by using MBE or MOCVD[34, 35] is generally used to obtain high-quality, defect-free QDs with very good size uniformity.[36] This method utilizes highly lattice-mismatched growth of In(Ga)As on GaAs. The GaAs substrate has a lattice constant of ~ 5.66 Å while that of InAs is 6.06 Å. In this InAs/GaAs system, the 7 % lattice mismatch between InAs and GaAs leads to the formation of InAs QDs on a GaAs (100) substrate. The initial InAs growth occurs layer by layer on the GaAs substrate because of the small interface energy between the substrate and the grown material. However, as the layers or InAs thickness increases, the strain energy will increase. At a certain thickness (~ 1.7 ML for InAs[37]), the strain energy will reach the limit where the system cannot afford to remain in the 2D growth mode, and the layer favorably releases the strain by forming the subsequent InAs 3D islands (QDs) on the already-grown 2D layer. These strain-induced InAs islands or QDs are formed randomly in an attempt to recover the bulk InAs lattice constants of ~ 6.06 Å.[38]

The growth temperature can be measured by an optical pyrometer, and the typical growth temperature for GaAs is around 620°C. InAs QDs are formed around 470°C by depositing a few monolayers (~ 1.7 ML) of InAs on GaAs or InGaAs.[36] A different QD size and density can be obtained by changing the QD growth temperature and the amount of InAs deposited. The QD size and density can be measured using atomic force microscopy (AFM) and cross-section transmission electron microscopy (XTEM). The height and lateral size of typical QDs grown by MBE are ~ 5 nm[36, 39] and from 20 ~ 25 nm respectively. The lateral density of the QDs is ~ 5×10^{10} cm^{-2}.[39]

After the growth, the wafer was processed into square mesas of different sizes, 1000×1000 μm^2, 800×800 μm^2, 600×600 μm^2, and 400×400 μm^2, with corresponding different optical windows which allow front-side illumination using standard photo-lithography and wet-

etching as shown in Figure 1.2. To characterize the device, the square mesas and the ohmic contacts on the top and bottom layers were fabricated using standard wet chemical etching which was followed by evaporation of Ti/Pt/Au ohmic contacts on the top and bottom *p*-type GaAs contact layers.

QDIP and DWELL characterization includes the detection spectrum, photo responsitivity and photo detectivity calculation, dark and noise current, noise and photoconductive gain calculation, and temperature dependent performance. Hence, the device was mounted on the cold

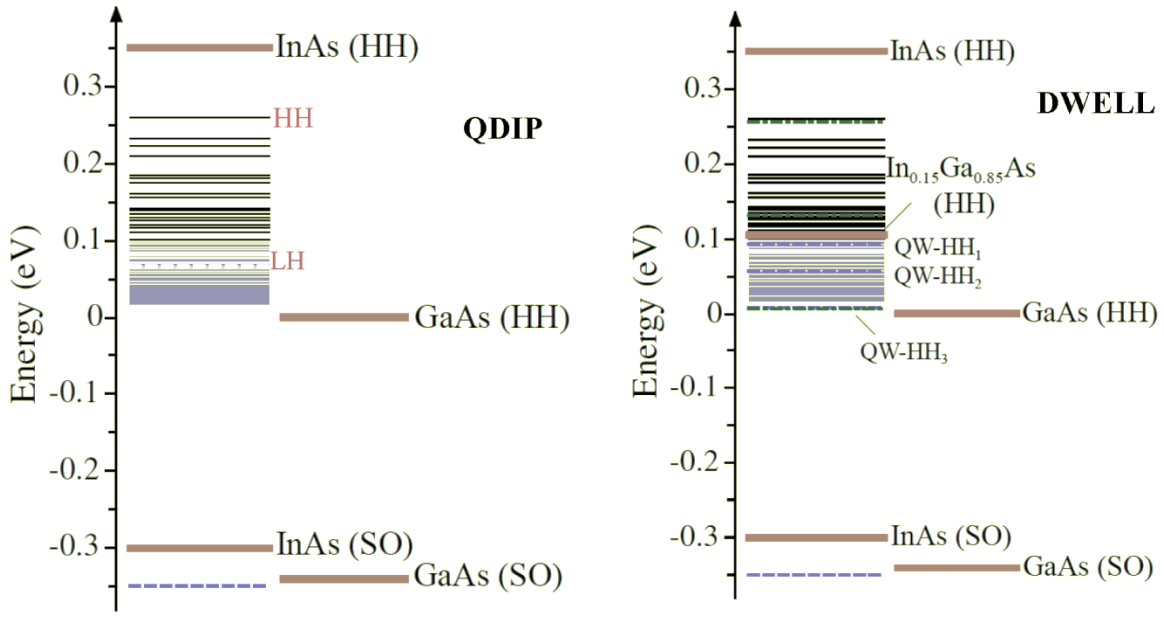

Figure 1.3 The valence band energy levels of the QDIP and DWELL detectors for hole states obtained by using an 8 × 8 k.p model. In DWELL, solid horizontal lines represent hole energy levels in QD while the dashed lines are the calculated HH states of the $In_{0.15}$ $Ga_{0.85}As$/GaAs QW. The thick lines are the band edges.

head of the liquid nitrogen-cooled Dewar and liquid helium-cooled cryostat to allow measurements of spectral response, noise, and dark current, respectively. The normal incidence spectral response was measured using a Perkin-Elmer system 2000 Fourier transform infrared

spectrometer. A bolometer with known sensitivity was used for background measurements, and the measured data were corrected by the background spectra.

1.3 Results and Discussions

The hole states were calculated using a computer program developed by Dr. Hongtao Jiang and Prof. Jasprit Singh of University of Michigan for InAs/GaAs QDs based on an eight-band **k**.**p** model with the effects of strain included with the valence force field model,[40] whereas the QW levels were calculated using the effective-mass method.[41] The input parameters for the program were electron or hole state, QD height, QD base area, Lattice constant, band gap, splitoff energy, α-bond stretching, β-bond bending, and deformation potentials. Unlike the case of an electron state in conduction band, many hole states are allowed in the valence band of the dots.

Table 1.1 Input parameters for k.p program of InAs/GaAs QDs at 0K.

	GaAs	**InAs**
Bandgap [eV]	1.5192	0.419
Splitoff energy [eV]	0.341	0.38
Lattice constant [A]	5.6533	6.0584
alpha--bond stretching [N/m]	41.19	35.18
beta--bond bending [N/m]	8.95	5.50
ac--deformation potential [eV]	-7.17	-5.08
av--deformation potential [eV]	1.16	1.00
b--deformation potential [eV]	-1.6	-1.8
d--deformation potential [eV]	-4.23	-3.1

From the numerical computation point of view, this means a large number of eigenvalues need to be solved simultaneously from the eight-band Hamiltonian, which becomes even more difficult in the higher hole energy range where dense states[42] are included. To make the computation easier, the spin-orbit split-off (SO) states were treated separately and obtained by

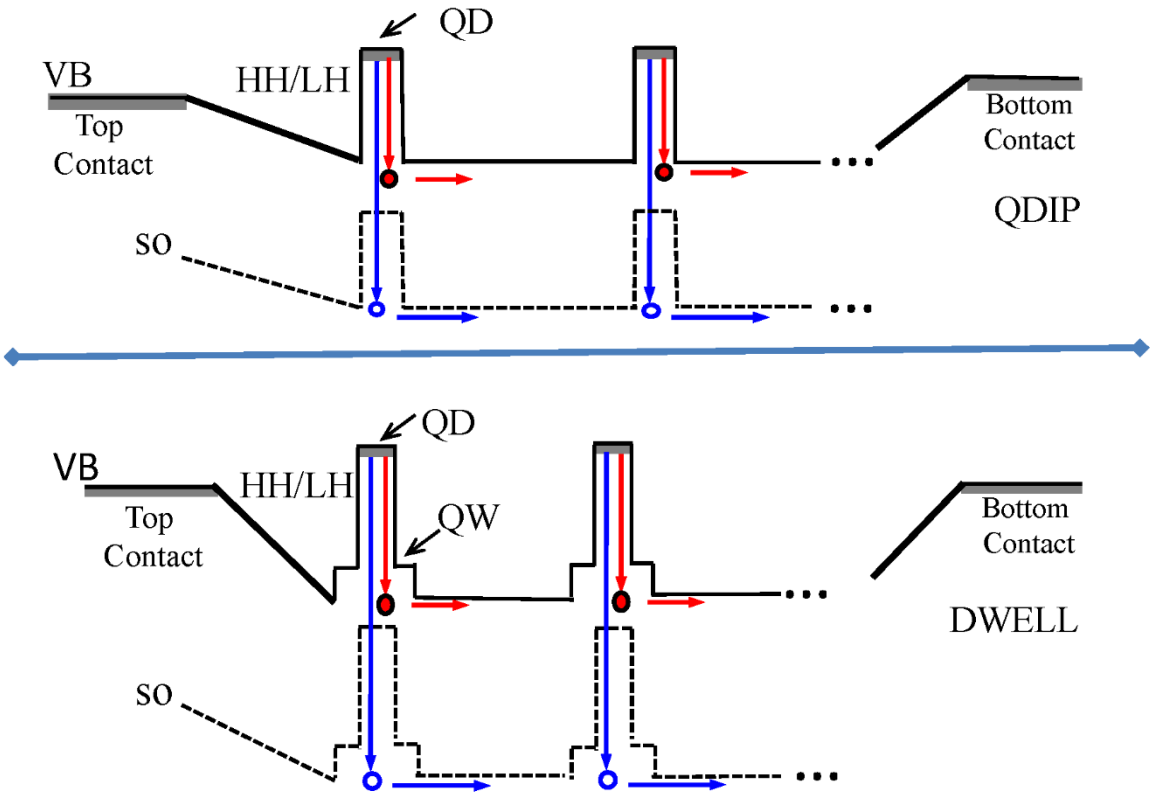

Figure 1.4 Schematic valence band energy levels of QDIP and DWELL. The intersubband transitions; HH to HH and HH to SO levels are schematically shown. There are many other possible intersubband transitions. The distribution of energy levels inside the QD and QW are shown in Figure 1.3.

treating the QD as a quantum well (QW) and using an effective-mass method.[41] The much wider in-plane dimension of the dots than the height partially validates such a treatment.

The heavy-hole (HH), light-hole (LH), and SO levels in the QD and DW structures are shown in Figure 1.3 QDIP and DWELL. The GaAs or QW SO state represents the QD SO hole

and interpret the spectral response, which should be acceptable for analysis on distinguishing respective contributions of VB hole transitions to the response. In the DWELL energy levels of Figure 1.3 (b), the $In_{0.15}Ga_{0.85}As/GaAs$ QW was designed to have three heavy holes (HH1, HH2, and HH3) which are obtained using an effective-mass method[41] with an almost continuous set of QD HH and LH levels. Therefore, DWELL detectors represent a hybrid of the quantum well infrared photodetector (QWIP) and quantum dot infrared photodetector (QDIP).[39] Hole transitions can be either from bound to bound or from bound to quasi-bound (or to the continuum). The schematic valence band profiles with the two possible transitions (from HH to HH or HH to SO) of holes for QDIP and DWELL are shown in Figure 1.4.

1.3.1 MIR response of QDIP versus DWELL

The spectral response of *p*-QDIP and DWELL are interpreted using the possible transitions in computed valence band energy levels of QDs and QW, as shown in Figure 1. 3. At 78 K, there are two primary response bands at 1.5 – 3 and 3 – 10 μm for both QDIP as shown in Figure 1.5 (a) and DWELL as well. Even though, the QDIP and DWELL samples contain a much thinner absorbing region than the heterojunction, the responsivity of *p*-QDIP is about 10 – 20 times higher than that of the heterojunction detector with nearly the same threshold wavelength as shown in Figure 1.5 (b). This indicates that due to the long carrier life time in QDs structures,[30] the origin of response is due to QDs, and not to the *p*-type GaAs contact layers. The response of QDIP is also higher than that of the DWELL detector, owing to the higher hole escape probability in the QDIP.[43]

The experimental short-wavelength response peak at 0.552 eV (2.25 μm) corresponds to the hole transition from the HH ground state to the SO state transition I of Figure 1.5 (a), while the long-wavelength peak at 0.247 eV corresponds to the hole transition from the HH ground state to the state near the GaAs barrier (transition II). This hole transition which contributes to the primary response peak at 0.247 eV (5.02 μm) is from ground state to quasibound states. The broad nature of the response peak with $\Delta\lambda/\lambda = 0.44$, where λ and FWHM, Δλ are 5.02 μm and

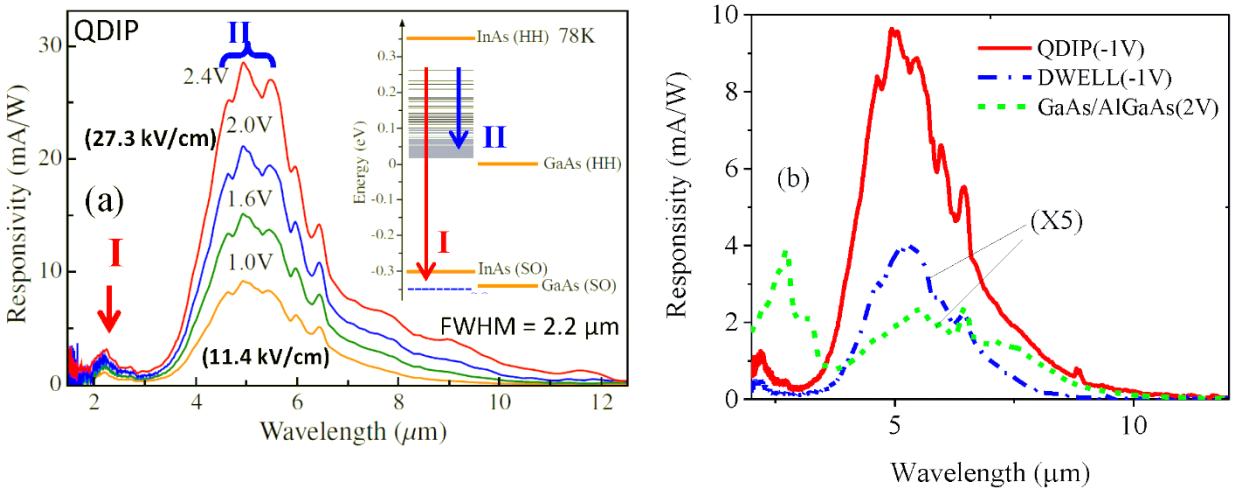

Figure 1.5 (a) Spectral response of the *p*-type QDIP at 78 K. Inset shows the two transitions for experimentally measured response bands at 1.5 – 3 and 3 – 10 μm. (b) Response spectra of the *p*-type QDIP, DWELL and GaAs/AlGaAs heterojunction detectors are compared. The bias voltages are selected such that they lead to nearly the same electric field.

2.2 μm, respectively, is due to the higher density of hole states compared to the corresponding electron states and QDs size fluctuations.[44, 45] The hole states become denser[42] at the higher energy portion of the HH confinement potential as shown in the inset of Figure 1.5 (a), due in

part to the larger hole effective mass and to the light-hole (LH) confinement potential, which leads to a continuum of lightly bound states.[46] However, the HH bound-to-HH quasibound transition may dominate over the HH bound-to-LH continuum transition, as the bound-to-

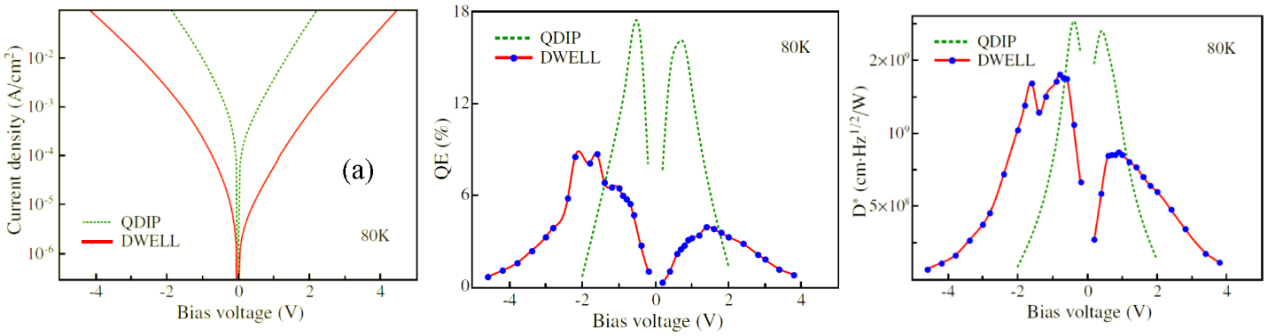

Figure 1.6 (a) Dark current density of the *p*-type QDIP and DWELL at 80 K. (b) and (c) (shown as insets) are the QE and specific detectivity (at 5.2 μm), respectively. The QE is obtained by assuming that the photoconductive gain equals the noise gain.

quasibound transition has higher absorption than the bound-to-continuum transition.[47] The short-wavelength response contributed by the HH to the SO transition is not as strong as in the heterojunction case, as compared to the HH to HH response. A possible cause is the impact of strain on the local band edges,[48] leading to a much shallower SO confinement potential than the HH band and giving rise to continuum SO states. Additionally, scattering events are required to transfer holes in the SO states to the HH states of the barrier to facilitate transport, which somewhat reduces the escape efficiency.

DWELL has the same GaAs barrier and hole concentration in the absorber as the QDIP, hence, their dark currents due to the thermionic emission should be comparable. However, the experimental dark current of DWELL is about 40 times less than that of QDIP, as shown Figure 1.6 (a). This can thus be explained by that the distribution of holes in DWELL is sharply

different from QDIP due to possible interaction between QD and QW.[10] This may partially explains DWELL response is caused by transitions from the HH in QDs to HH in the QW (bound state).

The improvement of the performance can be achieved by enhancing the absorption. One of the possibilities is to utilize transitions between the bound and bound states, which have the stronger wave-function overlapping than the transitions between the bound and the quasibound/continuum states.[31] One of the advantages of using *p*-type response is its stationary spectral response without showing the bias selectivity (bias independent).[31] The need of tailoring spectral response can be achieved by designing the QW. The QDs size determine the energy levels spacing and the dot size is hardly possible to control using Stranski Krastanov method. However, the QW levels can easily be controlled by changing the width and height of QW. It is expected that bias dependency can be obtained by moving the HH level closer to the potential barrier to increase the tunneling probability. The well-preserved hole response will facilitate the control of the response and designing multicolor response is also possible by integrating different DWELL structures.[31]

The noise gain (g) can be calculated through the expression $g = I_n^2/4eI_d$, where I_n is the experimentally measured noise current, and I_d is the dark current (to be discussed in detail in chapter 3). The comparison of QE for QDIP and DWELL (as shown in Figure 1.6 (b)) is obtained using $QE = Rhc/g\lambda e$, where R is the responsivity. The maximum QE of the QDIP and DWELL detector were obtained to be 17 % and 9 %, respectively. The specific detectivity is given by $D^* = R\sqrt{A \times \Delta f}/I_n$, where A is the detector area and Δf is the bandwidth. The maximum values of detectivity at 78 K of QDIP and DWELL for the response peak at ~ 5.2 μm were 1.8×10^9 and 1.4×10^9 cm $Hz^{1/2}$/W, respectively. These results suggest optimization of the

QW levels in the DWELL detector will lead to optimum escape hole probabilities allowing for higher responsivity and detectivity.

1.3.2 Far infrared (THz) response of QDIP and DWELL

The spectral responses were measured over temperature range from 78 K to 130 K. The 5.4 μm (0.230 eV) peak corresponds to hole transition from the ground state of QD to states near the GaAs barrier.[49] At 78 K, holes lie in the ground states which lead to the main response peak in the MIR range. The elevated temperature results in a broadening of the Fermi distribution

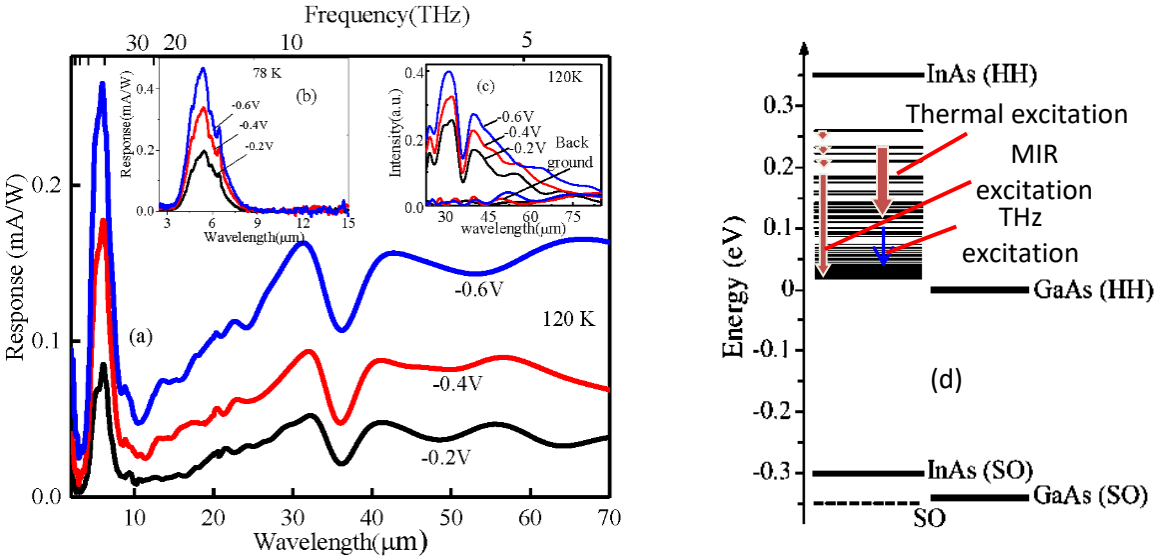

Figure 1.7 (a) Responsivity versus wavelength measured at T = 120 K for three different bias values. (b) Response versus wavelength measured at T = 78 K. There are no low energy transitions or THz response at 78 K. (c) Comparison of raw data of THz response and background noise level. The THz response spectrum is broad and extends beyond ~ 70 μm. The lower energy response (lower than 17.7 meV or ~ 70 μm) is below back ground noise level. (d) MIR Transitions from ground state of QD to states near the GaAs band edge, thermal excitation followed by optical or THz transitions. Modified after reference 25.

function and more carriers occupying the upper energy states where the energy spacing is of the order of the THz energy range. Hence the corresponding bound-to-continuum or quasi-bound transitions result in a THz response that increases with temperature.

Similarly, the QDIP has THz response with the same thermal and optical transitions as DWELL. As shown in Figure 1.6 (a), since the dark current in QDIP is higher than the corresponding DWELL, the dark current in QDIP overwhelm the response signals at temperatures above ~ 120 K. THz response at 110 K is shown in Figure 1.8.

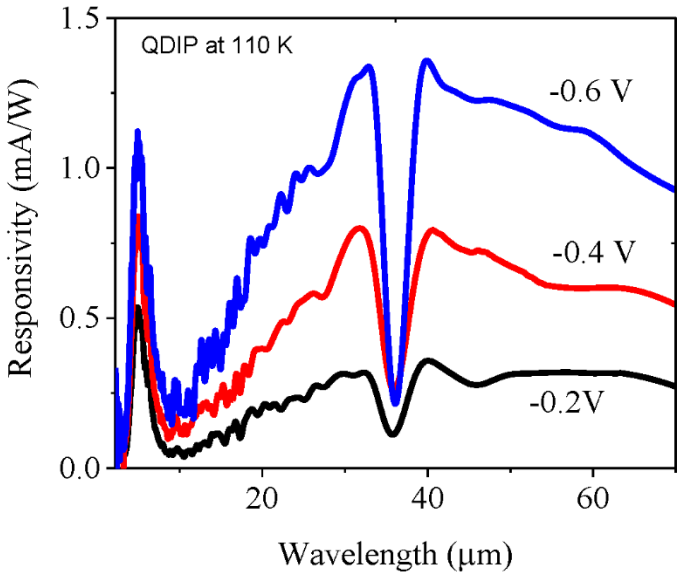

Figure 1.8 THz response of the QDIP at 110 K. Like DWELL, the THz response of QDIP extends up to 70 μm and increases with bias voltages.

Comparison of MIR and THz responses at three different bias values is shown in Figure 1.9 (a). At low temperature, such as 78 K, free holes occupy the lower energy levels (ground state, first, and second excited states). Excitation from these lower energy levels needs energy in the MIR energy ranges and hence, there is no FIR (THz) response as shown in Figure 1.9 (b). The THz response spectra start to appear for temperatures higher than ~ 100 K, and the response has

a broad spectral range over ~ 70 μm. Although, the detection of terahertz radiation up to 1 THz could be expected due to closely spaced upper energy states, the background noise level due to high dark current dominates the photocurrent at wavelengths higher than 70 μm as shown in Figure 1.7 (c). The variation of MIR and THz response spectra with temperature at a fixed applied bias of - 0.4 V (or field of ~ 4.54 kV/cm) is shown in Figure1.7 (a). The THz response

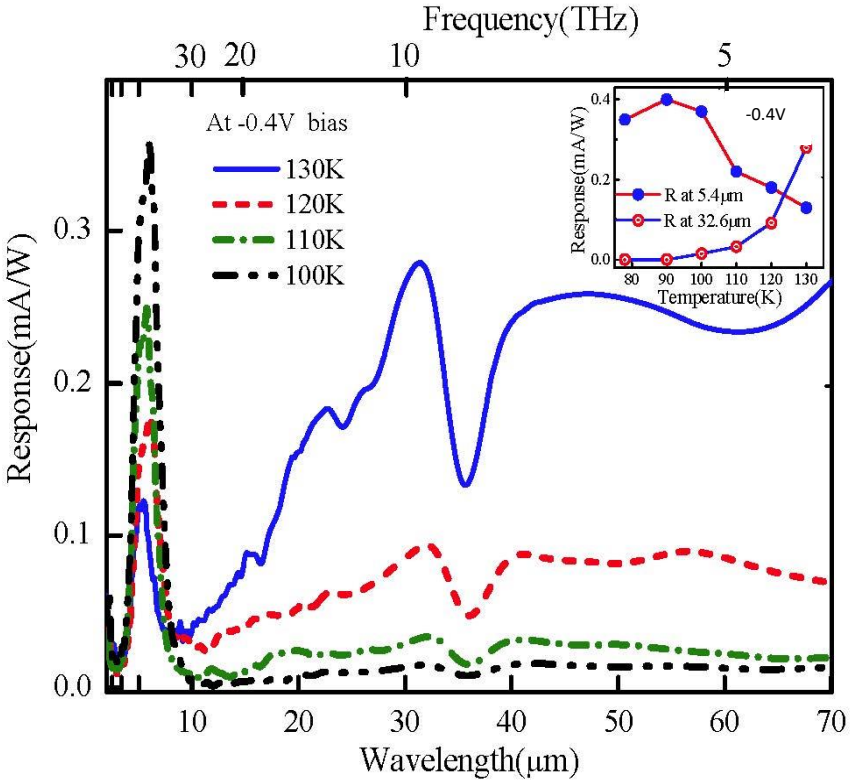

Figure 1.9 The variation of MIR and THz response spectra with temperature at a fixed applied bias of - 0.4 V. As the temperature increases, carriers are excited to higher levels reducing the rate of transitions that give rise to MIR response whereas it enhances lower energy transitions or THz responses. The inset shows a comparison of the MIR and THz responses variation with temperature. After reference 25.

increases with increasing temperature which contrasts with a decreasing MIR peak at higher temperatures. For a temperature increase from 80 K to ~ 90 K, the MIR response increases reaching the highest response at ~ 90 K. QD holes are confined due to energy quantization in all

three dimensions and electron-hole scattering is greatly reduced.[50] Since the intersubband energy between ground state and continuum is larger than the phonon energy, the optical phonon emission is not allowed. As a result, the hole relaxation time from the continuum states increases due to phonon bottle neck.[50]

This increase in response with the temperature may be related to reduced relaxation of carrier back to QD from the continuum states[20] and to enhanced escape of excited carriers. As the temperature is further increased, due to a decrease in carrier's occupation in the ground state and an increase in carrier population in excited states, MIR response starts to decrease while the THz response starts to appear and increases with temperature. In the temperature ranges (~ 100 to 130 K) where we see the THz response emerge, the MIR response decreases with increasing temperature (see Figure 1.9).

Furthermore, it is experimentally confirmed that the THz region (or the broad response peak) starts to appear only for temperatures beyond ~ 100 K and increases as the temperature rises from 100 K to 130 K. The calculated energy spacing between the dot levels varies from ~ 5 meV to 28 meV. There is no peak shift with either bias voltage or temperature. The DWELL dark current increases from 2.4×10^{-3} A/cm^2 to 0.12 A/cm^2 which is about 50 times increase for temperature changes from 100 to 130 K. At 130 K and - 0.6 V bias, the thermal noise calculated from the equation $I_{th} = \sqrt{4k_B T/\mathcal{R}}$, where k_B is Boltzmann constant, T is temperature and $\mathcal{R}$ is differential resistance of the detector, is 1.18×10^{-12} A/$\sqrt{Hz}$. The corresponding shot noise, $I_d^n = \sqrt{2eI_d}$ is 7.1×10^{-12} A/$\sqrt{Hz}$, which is close to the measured noise current of 7.5×10^{-12} A/$\sqrt{Hz}$ indicating the dominant role of dark current noise at a temperature of 130 K. From 78 K to 130 K, the DWELL peak responsivity of the 5.4 μm absorption peak decreases by ~ 65 %, while the

responsivity of much longer wavelengths around the ~ 32.6 μm absorption peak increases by ~ 100 % as the temperature change from 100 K to 130 K. Hence, it can be said that the THz response possibly originates from thermal excitation of carriers in QD states and is strongly dependent on temperature. The longer wavelength (~ 32.6 μm) response was measured up to a

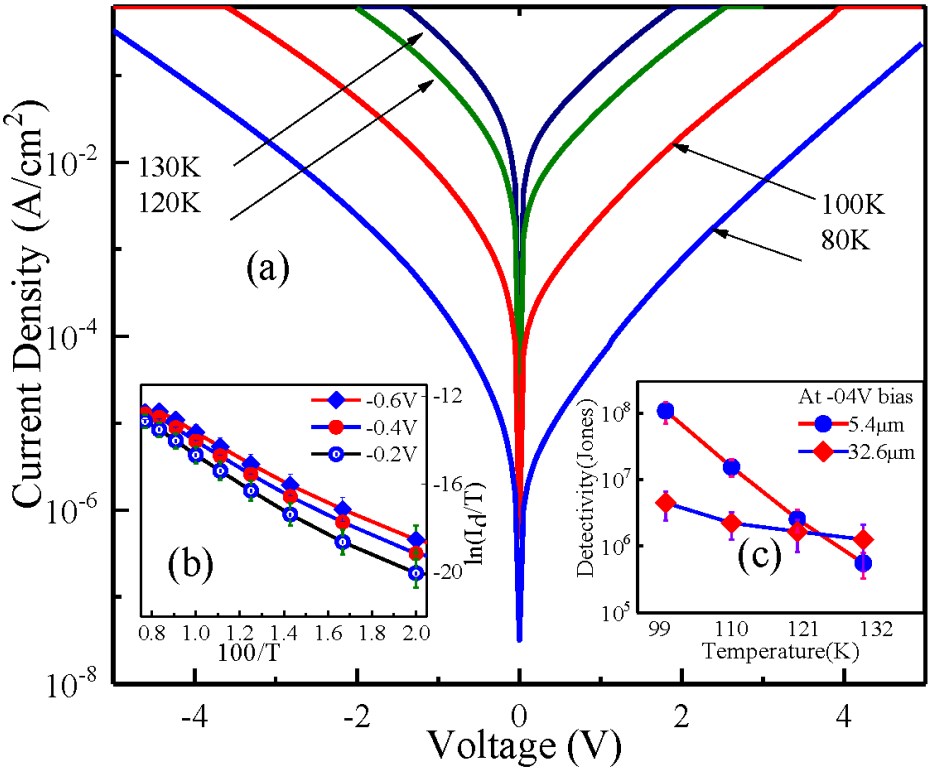

Figure 1.10 (a) Variation of dark current density as a function of bias at different temperatures. (b) The Arrhenius plot of dark current to temperature ratio versus inverse temperature (100/T) for bias voltages of - 0.2 V, - 0.4 V, and - 0.6 V. (c) Temperature variations of specific detectivity at 5.4 μm and 32.6 μm. Modified after reference 25.

highest temperature of 130 K with peak responsivity of ~ 0.54 mA/W (at an applied bias of - 0.6 V), which is a very high operating temperature as compared to other THz QW and QD detectors.[10, 51]

Moreover, using a high-speed mid-IR photoconductivity technique, long carrier lifetimes of 3 - 600 ns in an InAs/ $In_{0.15}Ga_{0.85}As$ DWELL heterostructures have been observed suggesting their potential for high temperature operation[52] and for fabrication of LWIR imaging focal plane arrays (FPA).[53] DWELL structures can also reduce the thermionic emission by controlling the energy levels (states) of the QW with respect to the GaAs band edge, and this enables the detector to operate on transitions from the ground state of InAs QD to a state in the InGaAs QW.[24] Hence, by optimizing the doping level and well width of DWELL for longer carrier lifetime or higher escape probability, detector responses and detectivity can be improved and extend the THz detection with operating temperatures up to 130 K or higher. Figure 1.10 (a) shows the dark current density versus voltage characteristics for temperature in the range 80 – 130 K.

As the temperature increases from 70 K to 150 K, the dark current density increased sharply from 7.8×10^{-7} A/cm^2 to 0.26 A/cm^2 at - 0.2 V and from 6.34×10^{-6} to 0.62 A/cm^2 at - 0.6 V which is still lower than the dark current values of other IR devices operating at lower or the same temperature in a comparable wavelength region.[23, 29, 54] At lower temperatures, the increase in dark current density with applied bias was due mainly to the lowering of the potential barriers. In the Arrhenius plot shown in Figure 10 (b), the natural logarithm of dark current to temperature (I_d/T) ratio versus inverse temperature (100/T) plot was found to be linear for the temperature range from ~ 60 K to ~ 130 K. As the bias voltage ranges from - 0.2 V to - 0.6 V, nearly the same activation energy is determined from the Arrhenius plot, ~ 108 meV. The exponential behavior observed in dark current indicates that carrier thermal excitation to higher energy states is possible and confirms the dominant role of thermionic emission in THz response.

The specific detectivity (D*) is calculated from the measured peak responsivity R_p and the noise density spectra i_n at different temperature and bias voltage using the relation $D^* = R_p \sqrt{A \times \Delta f}/i_n$, where A is the detector area and Δf is the frequency band width. The dark current noise density i_n was measured with low-noise voltage preamplifiers and a SRS760 fast Fourier transform spectrum analyzer. The value of D* calculated for 5.4 μm absorption peak is 1.3×10^9 Jones at 78 K (- 0.8 V bias) and 2.7×10^5 Jones at 130 K (- 0.4 V bias). As shown in Figure 9, at the 9.2 THz absorption peak, 130 K, and - 0.4 V, the D* value is 1.4×10^6 Jones. Significant improvement can be achieved by using a double barrier resonant tunneling heterostructure which suppresses most of the dark current without blocking the photocurrent.[29] The low dark current enhances detectivity and operation at high temperatures. Optimization of the number and density of QDs will also enhance the absorption. The other concern regarding *p*-type carriers is lower mobility as compared to electrons. Since the dot layer is thinner, the hole mobility mainly depends on the GaAs barrier. Optimizing the thickness of the GaAs barrier between the dot layers can prevent multiple defects throughout the structure and enhance the photocurrent.

1.4 Summary

The *p*-type InAs/GaAs, MIR ($\lambda_p \sim 5.4$ μm) detector at 78 K, demonstrated the promise of using hole transitions to develop QDIP and DWELL, with a QE of 17 % and 9 % respectively. Two response bands at 1.5 – 3 and 3 – 10 μm were confirmed as being due to hole transitions from the HH to SO level and from the HH to HH level, respectively. Furthermore, this study reports a *p*-type THz (broad response with a peak response at ~ 9.2 THz) detector based on intersubband transitions in InAs/InGaAs QDIP/DWELL structures. MIR peaks are associated with transitions from ground state of QD to continuum states or near-barrier QW state, whereas

the THz responses originated due to higher temperatures (~ 100 K - 130 K) and possibly to transitions between excited QD levels, bound-to-quasi-bound or continuum states. Therefore, the detector response was extended to THz range up to ~ 4.28 THz (~ 70 μm) at a highest operating temperature of 130 K. Further optimization, such as doping level, width of the well, barrier thickness, using a double barrier tunneling heterostructure or a thin dark current blocking layer to reduce dark current, could enhance and extend the response of terahertz detection at temperatures higher than 130 K and improve detectivity.

2. LOW-FREQUENCY NOISE PROPERTIES OF *p*-DOPED GaAs/AlGaAs HETEROJUNCTION PHOTODETECTORS

2.1 Introduction

All solid-state devices exhibit inherent random fluctuations in the voltage or current (or electronic noise) at their terminals, which limits device performance or sensitivity. Understanding the physical origins and mechanisms responsible for different types of electronic noise is important in optimizing the performance of a broad range of electronic devices. Different types of noise, both internal and external, are observed in many optoelectronic devices. External noise is generated by outside sources such as power supply units (from 60 Hz wall sockets), cell phones, amplifiers, antenna effects in connecting wires, and many devices which transmit and collect signals. Often, these sources of interference can be identified and reduced from the signal by shielding.

Internal sources of noise are more difficult to eliminate and can be generated by the device's material properties[55] and structures.[56, 57] Hence, the internal noise come from dark currents, temperature fluctuations, and trap states within the structures. These appear as thermal noise, shot (and or G-R) noise and flicker or *1/f* noise. Shot noise and thermal noise are the fundamental noise components which are frequency independent (white noise), and can be controlled to some extent by the choice of device architecture and through optimizing the detailed design,[58] including the choice of active materials, growth technique, operating temperature, and doping levels.

Noise can also originate from defects and impurities within the structures and result in large fluctuations in electronic conductivity through fluctuations of carrier density,[59] mobility[60] or a combination of the two.[61-63] The emission and capture of carriers determine the net charge of

carriers. A defect trap is charged upon carrier emission and neutralized upon carrier capture. These charging-discharging of traps fluctuate carrier numbers, and in some cases phonon scattering, which lead to generation-recombination (G-R) noise. Hole traps in unintentionally *p*-type doped GaAs layers have been investigated,[64] the low-frequency noise properties of beryllium-doped GaAs/AlAs[58] quantum well, and epitaxial layers of $Al_{0.5}Ga_{0.5}As$[65] grown by molecular beam epitaxy (MBE) have been studied so far.

In this chapter, I discuss the Low frequency noise properties of *p*-type beryllium-doped infrared photodetectors in which a GaAs emitter is sandwiched between undoped AlGaAs barriers.[66] Doping the emitter can lead to excess noise owing to traps formed by ionized clustering of dopant and impurities,[67] which can reduce the gain of optoelectronic devices. This G-R noise has the general property that the noise spectral density increases at lower frequencies and so low-frequency noise (LFN) measurement can be utilized as a diagnostic tool to characterize devices.[68] Therefore, the aim of this study is to characterize the various contributions of noise on the performance of an infrared photodetector, and specifically their effect on device responsivity or photoconductive and dark current gain.

Noise is a random process, and hence analysis of noise in the time domain does not give useful information regarding its average magnitude**.** Therefore, a very important parameter in noise signal processing is the noise power spectrum density (PSD) of set of samples. The PSD is the voltage or current noise power per unit of bandwidth. It has dimension of voltage/current squared over frequency. The PSD can help us to identify the frequencies that carry the signal power or signal energy. I investigate how the noise and dark current gain mechanisms associated with carrier transport for different barriers and emitter thicknesses are related to a range of

parameters used for optimizing devices, including the dark current, photo absorption, and capture probability.

2.2 Detector structures and experimental procedures

Four GaAs/AlGaAs detectors with different emitter thickness and graded barriers were investigated (Table 2.1), with the valence band profile of the structures being shown in Figure 2.1. In all structures the highly *p*-doped (1×10^{19} cm^{-3}) GaAs emitter is sandwiched between two undoped AlGaAs barriers. The AlGaAs barrier heights are determined by Al mole fractions (X).

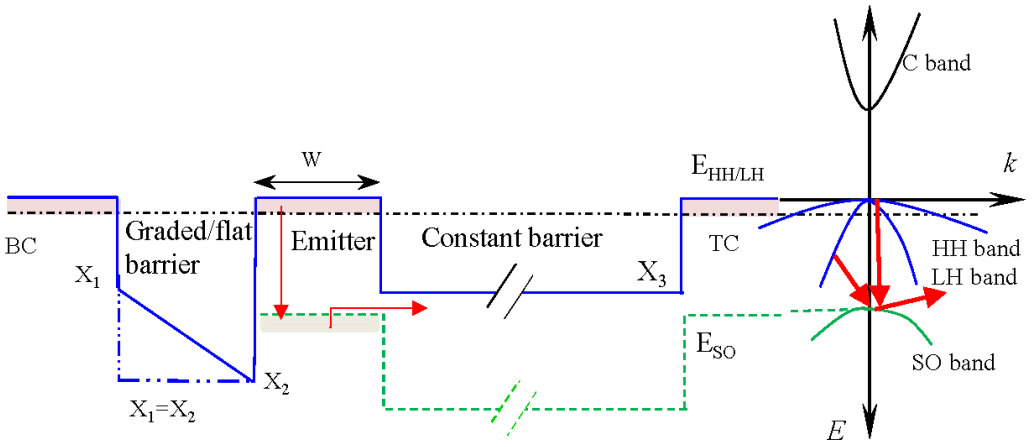

Figure 2.1 Schematic diagram of the valence band structure at wave vector k = 0 and E–k diagram for an emitter region of the detector: for the graded barrier structures $X_1 < X_2$ and in the constant barrier structure $X_1 = X_2$. The emitter thicknesses (W) and Al mole fractions (X_i) are tabulated in Table 2.1. The top contact (TC), bottom contact (BC), and the emitter are *p*-doped (10^{19} cm^{-3}). The dashed-dotted line represents the Fermi level of the heavy hole (HH)/light hole (LH) band. The dashed line represents split-off (SO) band in the detector. The arrows indicate the possible transition mechanisms: a direct or indirect transition from LH to SO band followed by scattering back to LH band. Modified after reference 66.

In three of the structures (SP1005, SP1006, and SP1007), one of the barriers is graded, whilst in the fourth structure (SP1001), both barriers have constant two different heights (X_1 =

0.45 and X_2 = 0.57). The width of the graded barrier is 80 nm in SP1005, SP1006 and SP1007, and the aluminum mole fraction is changed uniformly from 0.45 (X_1) to 0.75 (X_2) by adjusting the cell temperatures during growth to give a "continuous" (also known as "averaging") approach to the grading. The width of the barrier with the lower aluminum mole fraction (X_1) and X_2; next to the bottom contact is 80 nm for all structures.

Table 2.1: Detector structure details listing the different aluminum mole fractions (X_1, X_2, and X_3) used for the barriers, as illustrated in Figure 2.1. All emitters are *p*-doped at 1×10^{19} cm^{-3}. After reference 66.

Detectors No.	Lower edge (X_1)	Higher edge (X_2)	Constant barrier (X_3)	Emitter thickness (W)
SP1001	0.75	0.75	0.57	80 nm
SP1005	0.45	0.75	0.57	20 nm
SP1006	0.45	0.75	0.57	50 nm
SP1007	0.45	0.75	0.57	80 nm

A second barrier with a constant 0.57 (X_3) aluminum mole fraction then separates the emitter from the top contact and has a width of 400 nm. SP1005, SP1006, and SP1007 differ from each other by the emitter thickness as shown in the fifth column of Table 2.1. In SP1001, both barriers have a constant height: the first barrier has a mole fraction of 0.75 ($X_1 = X_2$), and the second barrier 0.57 (X_3). Figure 2.1 shows, for all detectors, photo-absorption in the emitter excites carriers from the light/heavy hole (HH/LH) bands into the split-off (SO) band. The excited carriers then escape from the emitter layer after scattering out of the split-off band back into the light/heavy hole band at the emitter-barrier interface[69] as shown in Figure 2.1. Detailed

explanations of the detection mechanisms, as well as details of the growth of all structures, have been reported previously in Pitigala, et al.[69, 70]

2.3 Experimental Procedures

A schematic and simplified experimental set up is shown in Figure 2.2. To determine the low frequency noise, detectors were biased with a DC voltage source. The voltage and current noise spectra were then amplified using a Stanford Research System SR560 low-noise voltage amplifier with a fixed gain of G = 1000 and an SR570 low-noise current preamplifier with a right sensitivity, respectively, and measured using an HP SRS-SR785 spectrum analyzer. This two-channel dynamic signal analyzer is a Fast Fourier Transform (FFT) signal analyzer covering the frequency range from 1 Hz to 102 kHz which is sufficient for the Low-Frequency Noise measurement.

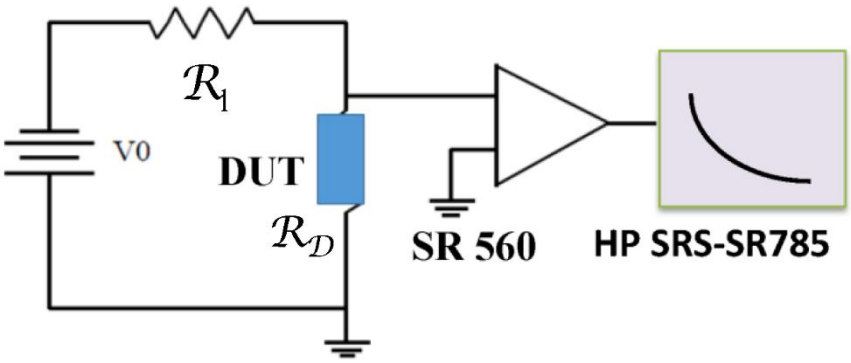

Figure 2.2 A Simplified experimental setup for the low frequency noise measurements, where DUT is the d detector under test, V_o is bias voltage, $\mathcal{R}_l$, is the load resistance, SR560 is a low-noise voltage amplifier and HP SRS-SR785 is the spectrum analyzer.

Detectors were mounted on a holder placed on the cold head of a liquid nitrogen-cooled Dewar, and the temperature was measured using a 330 Lake Shore Auto Tuning Temperature

Controller with an accuracy of ± 0.01 K. The detector, amplifier, and dry battery providing the bias voltage were shielded in a grounded aluminum box to prevent the external environment influencing the background noise. The bias voltage from batteries can significantly lower the interference from the measurement system itself, because batteries are more stable power sources. The noise spikes introduced by the power supply at the frequency of 60 Hz and its multiples are reduced by operating the preamplifier in the battery mode with a DC battery power source, and the spikes in the noise curves are ignored during the data analysis. The input voltage noise of the apparatus was determined by shorting out the sample and was found to be independent of temperature.

In the signal analyzer FFT analysis, the frequency axis, or “span" is divided into 800 equal intervals called “bins". The noise power spectral density was then measured in three to four different overlapping frequency spans. At low frequencies below ~ 10 Hz, the small bin width of 0.125 Hz is used to ensure better frequency resolution and accuracy of the measurements. A software, LabVIEW program was used to set these values and measure the PSD in the system.

Finally, the detector noise measurement is followed by data calibration with the measured noise floor (residual) of the system. To get the voltage noise power spectral density of DUT, $S_D^V(f)$, it is necessary to take in to account the noise floor of voltage noise PSD of system, $S_{floor}^V(f)$. Furthermore, the fact that the load resistance $\mathcal{R}_l$, contributes only thermal noise that acts in parallel with the DUT or sample impedance, $\mathcal{R}_D$, as shown in Figure 2.2. Hence, the total voltage noise PSD, $S_{meas}^V(f)$ (in V^2/Hz), measured at the output of the amplifier is given as the sum as $S_{meas}^V(f) = S_{floor}^V + S_{\mathcal{R}_l \, ll \, \mathcal{R}_D}^V$, where $S_{\mathcal{R}_l ll \mathcal{R}_D}^V$ is the voltage noise PSD of load resistance and DUT, $\mathcal{R}_l \, ll \, \mathcal{R}_D$ is the parallel combination of device and load resistances. The latter term is

given by $S^V_{R_l\, ll\, R_D} = (\mathcal{R}_D ll \mathcal{R}_l)^2 (S^I_D + 4k_B T/\mathcal{R}_l)$, where S^I_D is the current noise PSD of DUT, and the voltage noise is $S^V_D = \mathcal{R}^2_D \times S^I_D$. Then the voltage noise PSD of DUT is

$$S^V_D(f) = \left(\frac{\mathcal{R}_D}{\mathcal{R}_D\, ll\, \mathcal{R}_l}\right)^2 \left(S^V_{meas} - S^V_{floor}\right) - 4k_B T \left(\frac{\mathcal{R}^2_D}{\mathcal{R}_l}\right). \tag{2.1}$$

The corresponding current noise PSD is

$$S^I_D(f) = \left(\frac{1}{\mathcal{R}_D\, ll\, \mathcal{R}_l}\right)^2 \left(S^V_{meas} - S^V_{floor}\right) - \left(\frac{4k_B T}{\mathcal{R}_l}\right). \tag{2.2}$$

2.4 Theoretical discussion and Results

The four most common noise components are thermal, shot, G-R, and *1/f*. The thermal noise (or Nyquist noise) is generated by the equilibrium fluctuations of the electric current regardless of any external power supply, due to the random thermal motion of the charged carriers. In general, the thermal noise power spectral density (PSD) of voltage is given by

$$S_v(f) = 2\mathcal{R}hf/\left(e^{hf/k_B T} - 1\right) \tag{2.3}$$

where h is the Planck constant, f is frequency, and k_B is the Boltzmann constant, T is the temperature and $\mathcal{R}$ is the resistance of the device. In the low frequency range, up to ~10 kHz, $f \ll \frac{k_B T}{h}$, the voltage thermal noise power spectral density $S_v(f) = 4k_B \mathcal{R} T$ and the corresponding current noise PSD is given by $S_I = 4k_B T/\mathcal{R}$, which is frequency independent (or white noise). There is always thermal noise as long as temperature is not at absolute zero, and it is generally the white noise floor observed at high frequency and low temperature for resistors.

Shot noise is caused by fluctuations of current across the potential barrier or hetero-interface due to the discrete nature of carriers, and it is also white in nature. Except in ohmic devices like resistors where there is no homo- or hetero-junctional interface, shot noise occurs

virtually in all active detectors. It appears as a fluctuating current with power spectral density proportional to the number of charge carriers (e) or the current I through the interfaces within the device. It is given by $S_{sh} = 2eI$, where the current I is supplied by the DC source. In general, shot noise prevails at low temperature where the thermal noise is low enough depending on the impedance of the device.

Defects, impurities, and band discontinuities can, however, trap carriers, interrupting the current flow. If the trap levels are all identical, then there is a continuous emission and capture of holes (for *p*-type cases) between the traps and the valence band. Hence, the number of trapped and free carriers will fluctuate with the Lorentzian generation-recombination (G-R) spectrum, $S_n(f)$ of the carriers and is given by:[71, 72]

$$S_n(f) = \langle(\Delta n)^2\rangle \frac{4\tau}{1+(2\pi f\tau)^2}, \tag{2.4}$$

where $\langle(\Delta n)^2\rangle$ is the variance of the number of trapped carriers, f is frequency and τ is the characteristic (relaxation) time. At a given temperature, the maximum G-R noise level is observed when $2\pi f\tau = 1$. For frequencies much less than the characteristic frequency, $f \ll \tau^{-1}$, the G-R PSD is constant, while for $f \gg \tau^{-1}$, $S_n(f) \propto \frac{1}{f^2}$, as shown in the inset of Figure 2.3.

Another important noise component is flicker or *1/f* noise which is due to non-equilibrium fluctuations. A weighted summation or superposition of many G-R processes (Lorentzian spectra) with a smooth distribution of characteristic times then leads to a *1/f* noise spectrum,[58] where the intensity is proportional to the number of trap centers. The name *1/f* noise arises because a large class of fluctuations show a noise PSD that has $1/f^{\alpha}$ frequency dependence

with $\alpha \approx 1$. If different traps have a statistical weight $g(\tau)d\tau = \frac{c}{\tau}d\tau$, then the summation of G-R spectra yields the relation

$$S_{\frac{1}{f}}(f) = \int_0^c S_n(f)\frac{c}{\tau}d\tau = 4c\langle(\Delta n)^2\rangle\frac{1}{f}. \quad (2.5)$$

McWhorter[63] proposed this physical model of homogenous distribution of traps in an oxide layer in the semiconductor with the required $1/\tau$ dependence, and it is widely used for the noise in Metallic Oxide Semiconductor Transistors (MOSTs).

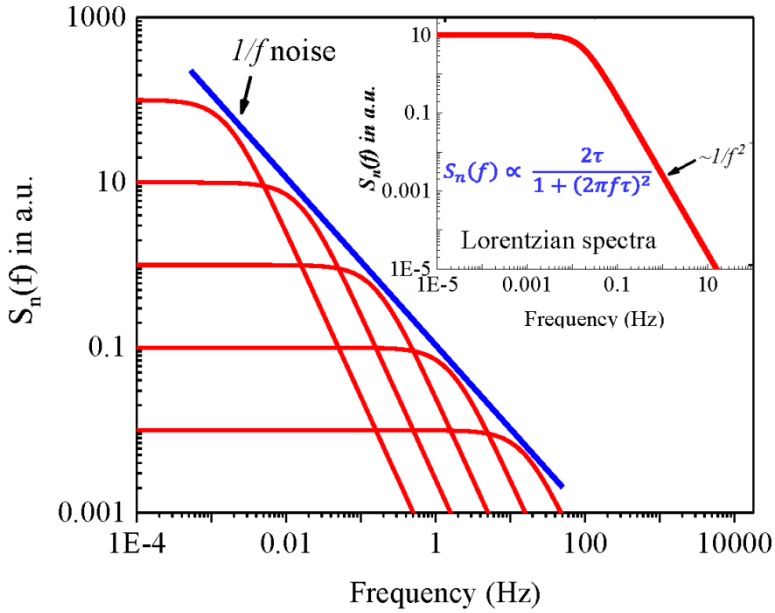

Figure 2.3 A weighted summation of many G-R noise (or Lorentzian spectra) with smoothly varying relaxation time leads to 1/f noise.

The origin of $1/f$ noise is still a point of debate and often explained by two models: noise related to mobility fluctuations $(\Delta\mu)$, and noise related to carrier density fluctuations (Δn). Hence, these fluctuations in either mobility or carrier number density will be manifested as fluctuations of the conductance $\boldsymbol{\sigma}$, or resistance $\mathcal{R}$, of a semiconductor that also fluctuates with a l/f spectrum[71]. The conductance fluctuations of an ohmic sample can be measured as voltage

fluctuations when a constant current I is passed through the sample, or as current fluctuations when the voltage drop V across the sample is kept constant. The low-frequency $1/f$ noise behavior is expressed simply by the equation:[71]

$$\frac{S_R(f)}{\mathcal{R}^2} = \frac{S_I(f)}{I^2} = \frac{S_V(f)}{V^2} = \frac{A_{1/f}}{f}, \tag{2.6}$$

where $A_{1/f}$ is a measure of the relative amplitude of the noise of the sample, and $S_{\mathcal{R}}(f)$, $S_V(f)$, and $S_I(f)$ are the noise power spectral densities of resistance, voltage, and current, respectively. If the G-R noise (equation (2.5)) may be associated with multiple trap levels of different relaxation times τ_i, which are assumed to be uncorrelated, then the corresponding terms can be added. The total noise power spectral density is a combination of $1/f$ noise, G-R noise, thermal noise, and shot noise, and can be described by the equation:[71]

$$S(f,T) = \frac{A(T)I^2}{f^{\alpha}} + \sum_{i=1}^{n} \frac{B(T)\tau_i}{1+(2\pi f\tau_i)^2} + S_{white} \tag{2.7}$$

where α is the frequency exponent in $S(f) \propto 1/f^{\alpha}$, and S_{white} can be either thermal, shot or a combination of these noise mechanisms. The second expression on the right-hand side of equation (2.7) represents the noise power spectral density of the G-R term resulting from a sum of n distinct trap levels. *A (T)* and *B (T)* are parameters related to the amplitude of *1/f* and G-R noise at a given temperature, respectively.

The dark current is an important property that brings about noise and a degradation of sensitivity of detectors. Hence, the analysis of experimentally measured noise begins with analysis of dark current. Figure 2.4 shows that, at low temperatures ($\approx 78\,K$), and low biases ($-1\,V < V\,(\text{bias}) < 0\,V$ with the negative bias applied to the top contact, or $0\,V < V\,(\text{bias}) < \sim 6.2\,V$ in the positive bias), the dark current is low, below 8×10^{-11} A. At higher biases, however, both the dark current and its noise to be discussed later, increase with bias and

temperature. At low bias voltages and temperatures, the device stays predominantly in the high resistivity state where the dark noise current is low and independent of frequency (G-R or shot noise).

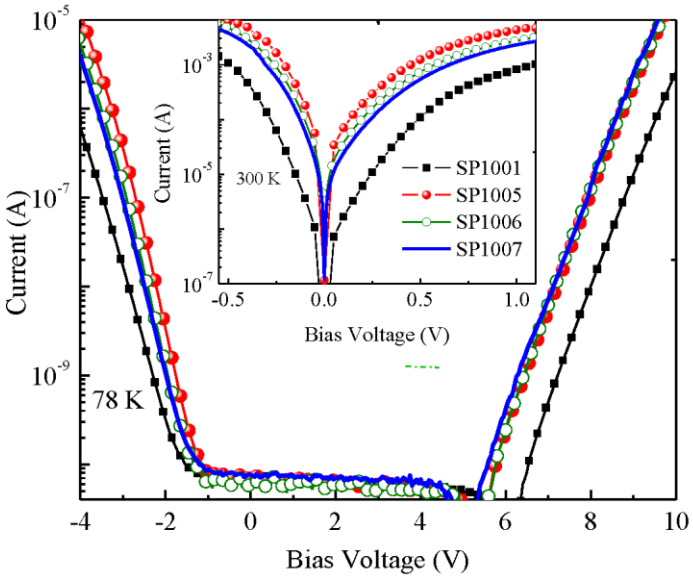

Figure 2.4 The dark IV characteristics of the four samples (SP1001 to SP1007) at 78 K and 300 K. The lowest dark current is observed in SP1001. Modified after reference 66.

The dark noise current calculated from the measured dark current and differential resistance of these devices is then dominated by noise resulting from the DC current supplied and has negligible contribution from thermal excitations. 1/*f*, shot, and G-R noises are all, however, current dependent. Since high resistance at low temperature is characterized by very small numbers of activated carriers in the device, 1/*f* noise for low DC current is not expected. But, the dominant source of G-R noise is from trap and defect sites, creating fluctuations in the carrier density throughout the detector. Experimental result reveals[73] that the noise power densities of these devices are dominated by G-R noise at lower bias and lower temperatures. The power

spectral density of G-R noise has a Lorentzian form as shown in the inset of Figure 2.3. However, at low frequencies, the plateau of Lorentzian power spectral density[16] has the

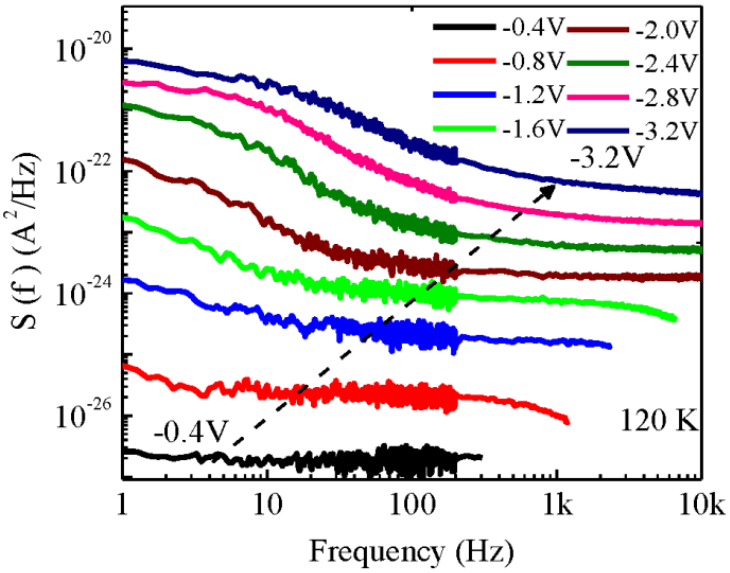

Figure 2.5 The noise power spectral density, S (f) at 120 K under different bias voltages for sample SP1005. At lower bias, the noise spectral density is independent of frequency. Modified after reference 66.

form $S_n(f) = 4qI_d g_n \Delta f$, which is frequency independent, up to a cut-off frequency located in the GHz range (in the case of DUT), above which the noise power spectral density rolls down as $1/f^2$.

The noise spectral density, S (*f*), at 120 K under different bias voltages for one of the graded samples with intermediate thickness (SP1005) is shown in Figure 2.5. At lower bias, i.e., higher resistance, the dominant noise is G-R with the cut-off frequency outside the band width, and hence the noise spectral density is independent of frequency. As the temperature increases from 78 K to 300 K (Figure 2.4) and/or the bias voltage increases (Figure 2.5), however, the system steadily switches to the low resistivity state, leading to other components of noise being

observed, including 1/*f* noise with a bias dependent cut off frequency ranging from ~10 to ~1000 Hz (Figure 2.5), and Johnson noise.[58]

The dark current-voltage, I-V, characteristics of the devices at liquid nitrogen and room temperature are shown in Figure 2.4. The asymmetry in the I-V trace is due to the asymmetry in the structure caused by both the graded barrier, and the different heights and widths of the upper and lower barriers. The device SP1001 (which has a constant barrier) has the lowest dark current.

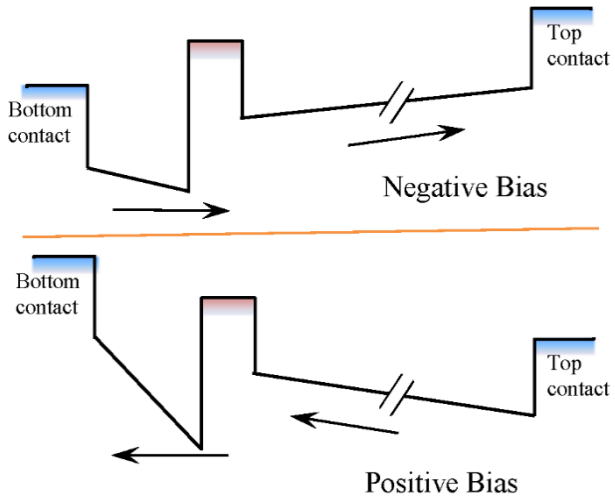

Figure 2.6 Graded barrier structure with valence band alignments under applied positive and negative electric field. Modified after reference 66.

The higher dark current in the graded barrier structure under negative bias can be explained by referring to the energy band alignments under applied electric field (Figure 2.6). Under negative bias, the valence band (VB) energy of the bottom contact will move down, making the graded barrier flatter, and hence the effective barrier height will be lowered. Therefore, a higher dark current can be expected compared to the constant barrier structure. At low positive bias, a charge builds up in the graded barrier structures will lower the valence band energy at the bottom contact, compared to the fixed or flat barrier height sample, and hence, once again, cause a

higher dark current as compared to the flat barrier. Furthermore, given the constant barrier sample (SP1001) has a larger percentage of aluminum compared to other SP100X series samples, where the graded barriers have an average mole fraction of ~ 0.60, SP1001 has the highest resistance, supporting the experimental observation of lower noise levels.

In Figure 2.7 (a), it can clearly be seen that the noise power spectral density, S (*f*), of SP1001 is lower than in the graded barrier structures. In all cases, the noise power spectral density increases with (negative) bias voltage and temperature owing to a decreasing dynamic resistance of the device as illustrated in Figures 2.7 (b), and 2.8 (a), respectively, for SP1005. It is also found that all devices have higher noise power spectral density for negative biases than the corresponding positive bias (inset of Figure 2.7 (b)).

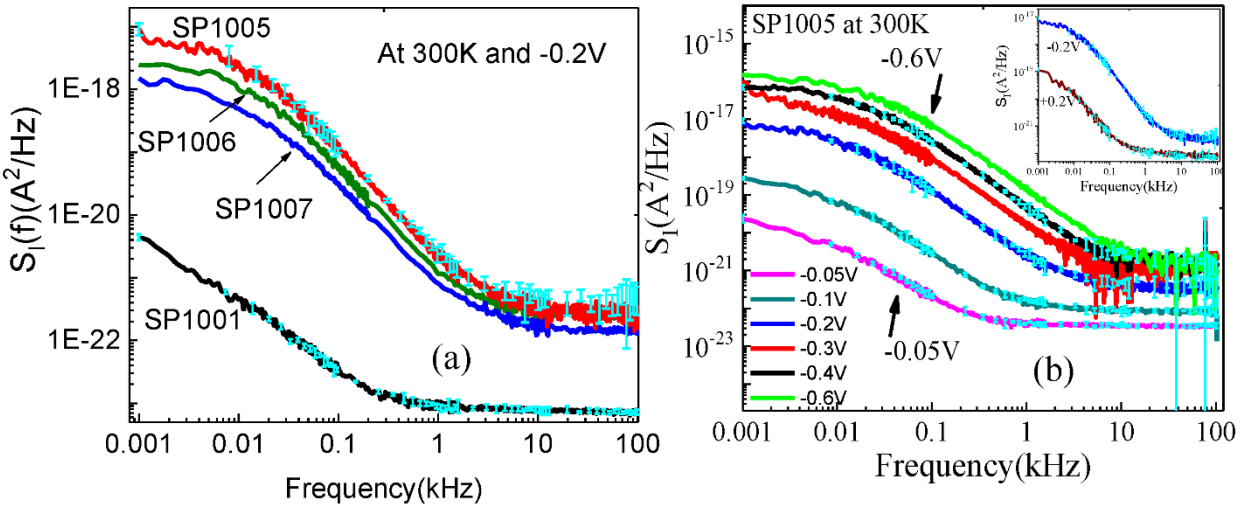

Figure 2.7 (a) The noise power spectral density (S (*f*)) of the wafers under a constant bias voltage of 200 mV. The detector with flat barrier (SP1001) has the lowest noise spectral density. (b) The variation of noise power spectral density with bias for SP1005. Increasing biases shift the corner frequency toward higher frequencies. The inset shows the comparative noise power spectral density for positive and negative biases. Modified after reference 66.

Figure 2.7 (b) shows, for bias voltages higher than - 0.4 V and frequencies higher than ~ 10 kHz, that the detector exhibits white noise spectra that are very close to the noise level of the measurement system, and hence it is difficult to see a bias dependence. However, at room

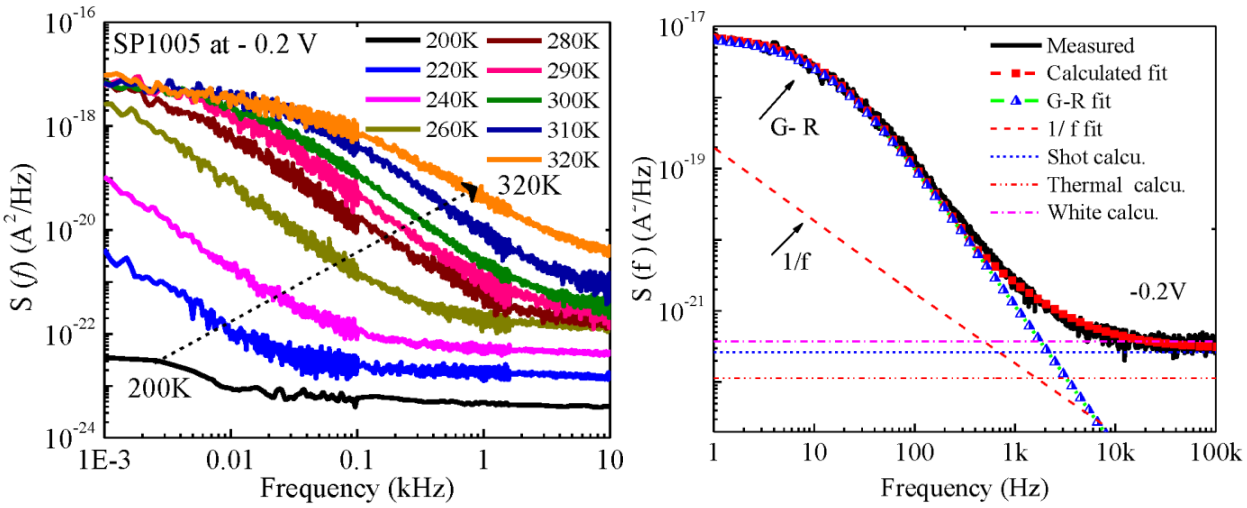

Figure 2.8 (a) The noise current spectral density S (f) measured for a temperature range from 200 K to 320 K at a bias - 0.20 V for SP1005. At higher temperatures, the G-R noise starts to appear. (b) Theoretical and calculated fits of different components of noise to the experimentally measured noise spectra. Modified after reference 66.

temperature, based on the noise power spectral density measured at - 0.2 V, and its calculated fit, it is possible to recognize the four types of noise: 1/*f*, G-R, shot, and thermal noise (Figure 2.8 (b)). In the region, where the excess noise ($1/f^{\alpha}$) is dominant (Figure 2.7 (b)), α is found to be 1 ± 0.1 at a bias voltage of - 50 mV. As the bias increased, α then varied from 1.0 to 1.5. No significant differences were, however, observed in spectral noise density for different emitter thicknesses (Figure 2.7 (a)).

The G-R noise shown in Figure 2.8 (b) is characterized by a Lorentzian spectrum with the time constant, τ given by[74]

$$\tau = \tau_o \, exp\left(\frac{E_a}{k_B T}\right) \tag{2.8}$$

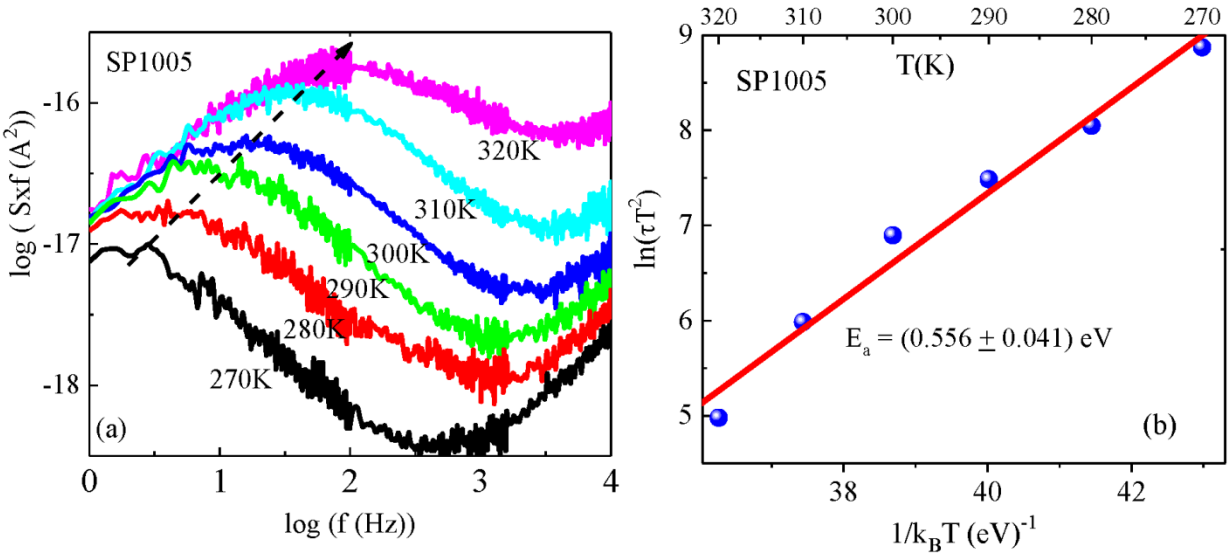

Figure 2.9 (a)The logarithm of S(f) × f versus logarithm of f for different temperatures at 200 mV. (b) The Arrhenius plot of time constants for the Lorentzian peak (G-R).

where E_a is the thermal activation energy, and $\tau_o = (V_{th}\sigma_T N_V)^{-1}$, $V_{th} \propto T^{1/2}$ is the average drift velocity of carriers, σ_T is the capture cross section of traps, $N_V \propto T^{3/2}$ is the density of states in valence band. In Figure 2.9 (a), log (f × S_I (f)) versus log(f) reveals the Lorentzian peak due corresponding to time constant τ to each trap level at different temperatures, and the dashed line shows the change in corner frequency with the temperature. The peak or corner frequency $f_c = \frac{1}{2\pi\tau}$, can be extracted by fitting the Gaussian amplitude at different temperatures. Then, equation 2.4 allows us to extract the activation energy of traps from the Arrhenius plot of logarithm of time constant times the Square of temperature vs $1/k_BT$. This Arrhenius plot reveals trap activation energy levels at 0.556 ± 0.041 eV for SP1005. Similarly, the activation energy of traps in SP1001 and SP1007 are 0.584 ± 0.060 and 0.581 ± 0.043 eV, respectively. The origin of this

trap level is not known yet. However, with less than 5 % marginal error, these results agree with the hole trap level reported in the literature at 0.554 eV for beryllium doped AlGaAs films,[75] which implies possible dopant migration into the barrier layers from the highly doped emitters. Krispin, et al[76] also shows similar deep level, that exhibit properties identical to those of well-known hole traps in GaAs, which are associated with Cu and Fe atoms on Ga sites, respectively for *p*-type GaAs/Ga (As, N)/GaAs heterojunctions.

One can assume that dark current and background photon noise limit the performance of photoconductive detectors. In the dark current limited condition, fluctuations in the number of mobile carriers via trapping and escape processes control the dark current, and therefore, the noise associated with the dark current is G-R in nature. The noise current I_n in the device is, related to the corresponding dark current I_d by:[77]

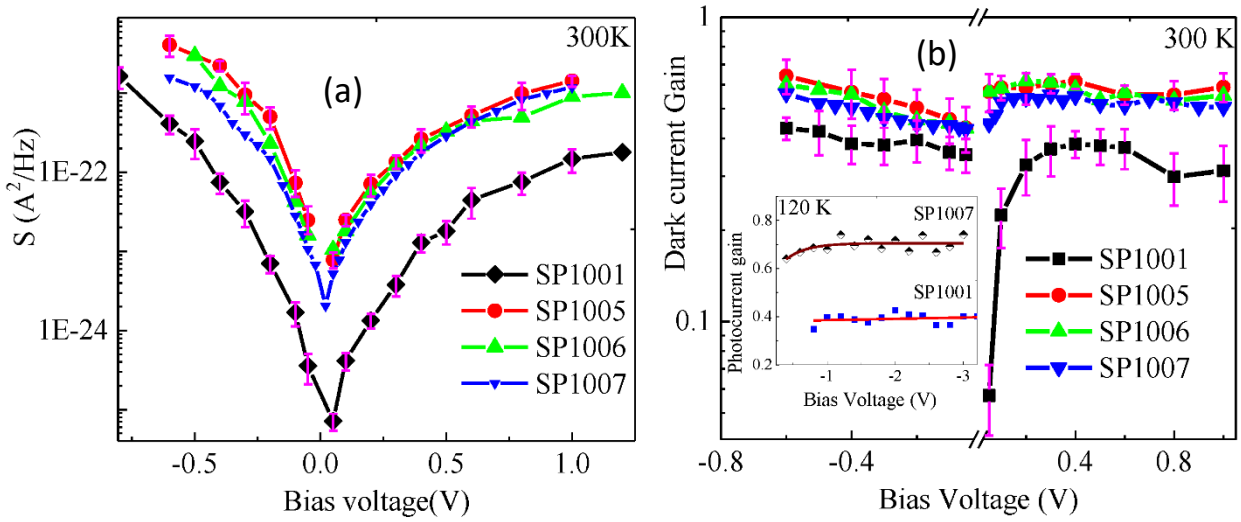

Figure 2.10 (a) A comparison between the measured noise power spectral densities for different structures at ~ 10 kHz. The detector with constant barrier (SP1001) has the lowest noise power spectral density, and for graded structures there is hardly any change with different emitter thickness. (b) Comparison of dark current gains for the three different wafers. In the inset, solid lines are the best fits to experimental data and show comparisons of photocurrent noise gain for flat and graded barrier heterojunctions at 120 K. Modified after reference 66.

$$I_n^2 = 4qI_d g_n \Delta f, \tag{2.8}$$

where q is charge of carrier, g_n is the dark current noise gain and Δf is the bandwidth of the measurement. According to Liu,[77] the expressions for dark noise current gain, g_n, and photocurrent gain, g_p, are given by:

$$g_n = \frac{1}{Np_c} \text{ and } g_p = \frac{1-p_c}{Np_c}, \tag{2.9}$$

respectively, where p_c is the capture probability of carriers traversing an emitter and N is the total number of emitters (or absorbers). If the capture probability $(p_c) \ll 1$, the difference between the noise current gain and photocurrent gain may be ignored, and they are both given by $1/Np_c$. If we neglect tunneling, the capture probability for transport of carriers associated with dark current and photoelectrons are the same, i.e., except for the emission mechanism; both dark current and photocurrent follow the same path. Hence, analysis of the experimentally measured dark current noise will help us understand the photoconductive gain.

For a detector in the background limited performance (BLIP) condition, the intrinsic noise of the detector is negligible compared to the noise due to the fluctuations of the number of incident background photons. As a result, the total noise is determined by the photocurrent under background illumination. Hence, the detector noise associated with background radiation is given by:[78, 79]

$$I_{Bn}^2 = 4q g_n I_p \Delta f, \tag{2.10}$$

where the total current in background limited operation is given by $I_p = e\eta g_p \phi_B$ (where ϕ_B is the incident photon flux and η is the total photoionization efficiency). The dark current can be written as $I_{dark} = g_n i_{em}$, where i_{em} is the thermal emission current from the structure. The

specific detectivity is $D^* = R\sqrt{A\Delta f}/I_n$, where R is the responsivity and A is the area of the detector. If the detectivity is normalized by the detector area and bandwidth of measurement, then $D^* \sim I_p/\sqrt{S(0)} \sim \eta g_p/\sqrt{g_n I_p}$ where, $S(0) = I_{Bn}^2$. Hence, in background limited operation, the detectivity is:

$$D_{Blip}^* \sim \sqrt{\eta \frac{g_p}{g_n}} = \sqrt{\eta(1-p_c)}\,. \tag{2.11}$$

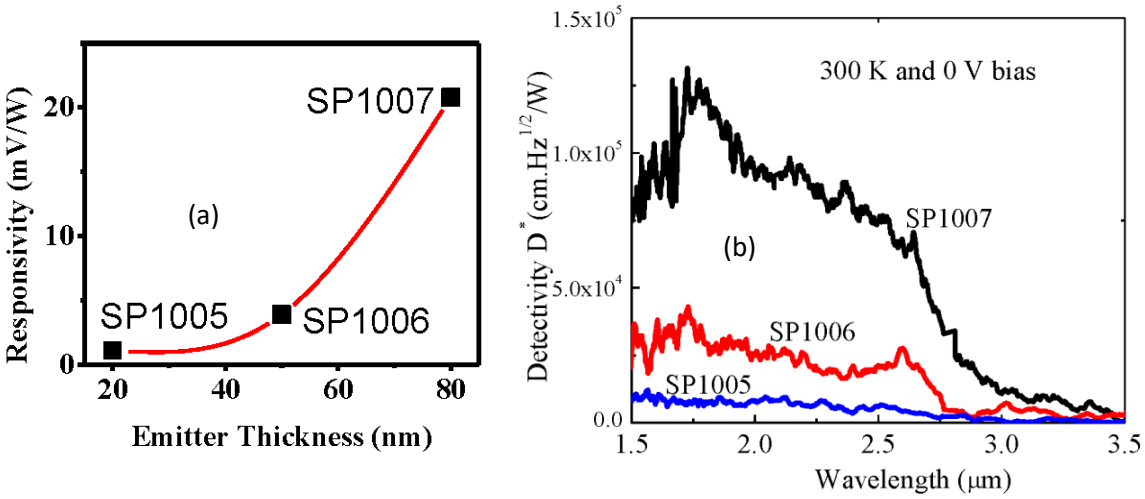

Figure 2.11 (a) The responsivity increases with the emitter thickness (20 nm, 50 nm, and 80 nm). (b) Comparison of detectivities for different emitter thickness. The thickest emitter (SP1007) has relatively the highest detectivity. After reference 66.

Assuming constant photoionization efficiency, the background-limited detectivity increases with the decrease of capture probability. In general, the capture probability p_c and escape probability p_e can be related as p_c = 1 - p_e, and hence if $p_e \rightarrow 1$, then $p_c \rightarrow 0$, and the detectivity is determined by the dark current noise. In this non-background limited condition, the total current is due to the dark current, and its magnitude is determined by the carrier concentration and drift velocity. Thus, in this case:

$$D^*_{dark} \sim \eta g_p / \sqrt{g_n} \cong \eta \sqrt{1/p_c}, \quad (2.12)$$

and the dark current limited detectivity also increases with decrease of capture probability, p_c.

Trapping of the carriers in the emitter/barriers leads to a significant charge buildup in the emitter/barriers and hence reduces the response. Grading the barrier, however, produces an offset between the barrier and emitter that reduces the recombination mechanism, and increases the gain owing to a higher momentum of the carriers.[70, 80] As shown in Figure 2.10 (b), and its inset, based on equation 2.9, a comparison of the dark current and photocurrent noise gains confirm that the escape probability of carrier is enhanced by grading the barrier, which results in further enhancement of specific detectivity (see equations 2.11 and 2.12). Increasing the emitter thickness for graded barriers then increases the response owing to increased absorption (Figure 2.11 (a)). At the same time, the escape probability of carriers decreases with increasing emitter thickness[18] due to limited carrier life time. Hence, the dark current slightly decreases and the specific detectivity increases with increasing emitter thickness (Figure 2.11 (b)). At room temperature, even though the responsivity is low (≈ 8 μA/W), a moderate specific detectivity (D*) ≈ 1.25 × 10^5 Jones for SP1007 was observed owing to the low noise spectral density, S (*f*). To increases this further, the design of detector needs optimization for higher absorption, and lower dark current.

2.5 Summary

In conclusion, the noise levels in *p*-type GaAs/AlGaAs heterostructures have been measured with both flat and graded barriers. At low temperature and low bias, the frequency independent G-R shot noise prevails whilst as temperature rises, both 1/*f* and Johnson types add to the shot noise. Comparisons of dark and photocurrent noise gains confirm that the escape probability of

carriers is enhanced by grading the barrier, whilst the graded barrier also reduces the recombination mechanism owing to the higher momentum of carriers. Despite only a very small change in noise density with increasing emitter thickness, the specific detectivity (or responsivity) does increase significantly owing to higher absorption efficiency. Thus, optimizing the emitter thickness of graded barrier detectors to enhance the absorption efficiency and increase the escape probability and lower the dark current, enhances the specific detectivity of detectors.

3. NOISE, GAIN, AND CAPTURE PROBABILITY OF *p*-Type InAs-GaAs QUANTUM-DOT AND DOT-IN-WELL INFRARED PHOTODETECTORS

3.1 Introduction

Quantum dots (QDs) based infrared photodetectors have attracted a lot of attention due to sensitivity to normally incident radiation which is hardly possible without optical coupling in quantum well infrared photodetector (QWIP) and for multiple band detections in the infrared (IR).[81, 82] The HgCdTe photodetectors have been successfully used for infrared detections. However, HgCdTe materials growth issues limit the spatial uniformity and production yield, which, in turn, increase the cost of HgCdTe focal plane arrays. Hence, III-V materials Quantum dot infrared photodetectors are subject current to researches as a good alternative technology to replace quantum well and HgCdTe infrared photodetectors.

As has been discussed in detail in chapter 1, in QDs structures, the detection mechanism is based on the intersubband photoexcitation of the charge carriers from confined states in the dots to the continuum or quasi-bound states. In bulk semiconductors, such as *p*-doped (1×10^{19} cm^3) GaAs, the relaxation time is very short ~ 0.1 ps, while QDs and DWELLs have longer carrier lifetimes (up to nanoseconds),[50, 52, 83] which leads to efficient collection of photo-excited carriers and ultimately leads to higher photoconductive gain[50, 83] and higher operating temperatures.[84] The optical nonlinearities and the gain dynamics in the QD based detectors are dependent on the carriers' emission-capture dynamics of the QDs.[50] Hence, the capture probability and relaxation mechanisms of carriers in QDs deserve further research for improvement of the performance of the QDs based detectors.

Therefore, the gain, capture probability, and carrier lifetime were theoretically analyzed and calculated from the noise power spectral density and dark current measurements. The

fundamental noise components, shot noise (G-R) and thermal noise, are frequency independent. The analysis of G-R and thermal noise which change with bias voltage and temperature help us understand carrier transport and emission/capture mechanisms such as capture probability which is critical in determining responsivity of detectors.

To realize high-performance (higher quantum efficiency, responsivity and detectivity) detectors, the noise power spectral density, carrier lifetime, and photoconductive and dark current gain are the most important parameters that need to be better understood and optimized. The *p*-type InAs/GaAs QD structures discussed here are based on holes as charge carriers instead of electrons. The energy levels (or density of states) of holes in a QD are much more closely spaced than those of electrons due to larger effective mass of holes. The hole-capture dynamics in QD-based structures is important for future information processing and storage devices.[85] Thus, this chapter focuses on comparisons between *p*-type QDIP and DWELL's dark current gain and capture probabilities, using directly measured noise power spectral density and dark current.

In highly *p*-doped QD structures, photoexcited holes can undergo several processes. First, the holes can relax back into the ground state of the QD. The unipolar nature of a QDIP greatly reduces electron-hole scattering. Photoexcited carriers have longer lifetimes due to reduced hole–phonon scattering because of the phonon bottleneck.[83] The dominant hole–hole scattering process is usually not a very fast process. Therefore, the photoexcited holes that escape from the QD driven by electric field, either relax into a different quantum dot or will be collected at the contact. Hence, the effective carrier lifetime, the capture probability, and the number of quantum dot layers are very important parameters in determining the gain and responsivity of the detector.

When the carrier is excited from the QD, the time that the photoexcited carrier takes before relaxing back into the QD state is the effective carrier lifetime. Depending upon the QD structure, the material, applied bias, and temperature, high values of photoconductive gains of *n*-type QDIPs have been reported,[86-89] with the gain values ranging from ~ 1 to ~ 10^6. High electron mobility in the barrier materials,[86] the low carrier capture probability or long carrier life time,[89] and avalanche mechanisms[87, 88] are some of the mechanisms proposed for the large measured gain values. There are many gain measurements for *n*-type QDIPs while very few attempts, such as *p*-type GaAs/AlGaAs QWIP[90] and Ge/Si QDIP,[45] have been made so far to study the gain experimentally for *p*-type detectors. In this chapter, I present a study of the noise, noise gain and capture probability of holes in highly *p*-doped InAs QDs based DWELL and QDIP. The capture probability of holes in DWELL is found to be about two times higher than the corresponding QDIP.

3.2 Detector structures and experimental procedures

The detectors were grown by molecular beam epitaxy (MBE), consisting of 10 stacks of quantum dot and dot-in-a-well structures sandwiched between two highly doped p^+-GaAs contact layers, grown on a semi-insulating GaAs substrate. The only difference between QDIP and DWELL is that in DWELL, the InAs QDs are placed in a 6-nm thick $In_{0.15}Ga_{0.85}As$ QW which in turn is surrounded by GaAs barrier layers. The dot density is about 5×10^{10} cm^{-2}. A δ-doping technique is used, with a sheet density of 5×10^{11} cm^{-2} *p*-type Be-dopants, placed above the 13-nm thick GaAs spacer which introduces about 10 free holes in each QD. The QD layers are separated by thick (~ 80 nm) GaAs barriers to suppress the tunneling emissions between adjacent layers. The QDs have nearly pyramidal shape with the average base widths of ~ 20 - 25 nm and height of ~ 5 nm. The detectors were fabricated into square mesas of 400×400 μm^2 with

an optical window of 260 × 260 μm^2 which allows front-side illumination. Other details of both detectors are given in Lao, et al.[30, 31]

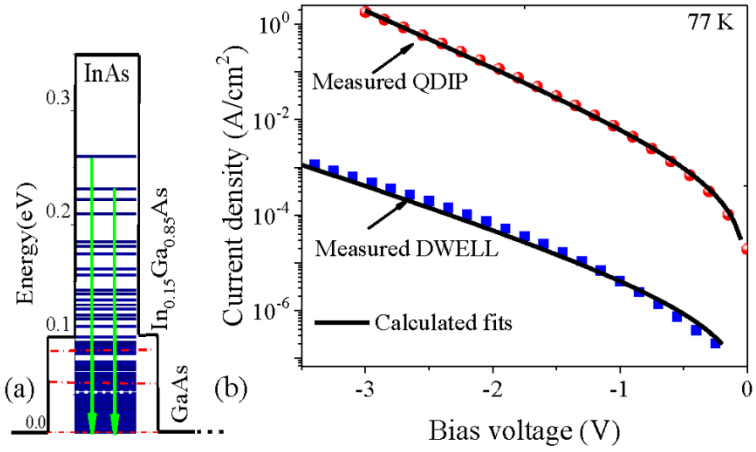

Figure 3.1 (a) The valance band structure of DWELL (G12-134) without the spin orbit split off band. The dominant bound to continuum (heavy hole (HH) to HH) transitions are indicated by arrows. QDIP (G12-133) has a similar valence band structure as DWELL except in DWELL the InAs QDs are placed in 6 nm thick $In_{0.15}Ga_{0.85}As$ QW. (b) Dark current density of DWELL (■) and QDIP (●) at 77 K. The solid lines are the corresponding calculated fits. After reference 43.

To characterize the detector, the square mesas and the ohmic contacts on the top and bottom layers were fabricated using standard wet chemical etching. Then the detector was mounted on the cold head of a liquid nitrogen-cooled Dewar and liquid helium-cooled cryostat to allow measurements of noise power spectral density and dark current. The voltage and current noise spectra were then amplified using a Stanford Research System, SR560 low-noise voltage amplifier with a fixed gain of G = 1000 or an SR570 low-noise current preamplifier with right sensitivity, respectively, and measured using an HP SRS-SR785 fast Fourier transform spectrum analyzer.

The *p*-type In(Ga)As/GaAs QDIP and DWELL are based on valence-band intersublevel hole transitions as opposed to conventional electron transitions. Two response bands observed at ~ 1.5 – 3 and ~ 3 – 10 μm are due to transitions from the heavy-hole to spin-orbit split-off QD level and from the heavy-hole to heavy-hole level, respectively. The dominant bound to continuum (heavy hole (HH to HH) transitions are indicated by arrows in Figure. 3.1 (a). At 78 K, both QDIP and DWELL displays promising results, such as a specific detectivity of ~ 1.8×10^9 Jones and 1.4×10^9 Jones, and maximum quantum efficiency of 17 % and 9 %, respectively, without employing optimized structures, such as the dark current blocking layers. At temperatures higher than ~ 100 K, THz response up to 70 μm is observed. In order to compare between QDs based and other heterostructures, a 30 period of 18.8 nm *p*-doped GaAs emitter and 60 nm $Al_{0.28}Ga_{0.72}As$ barrier heterostructures[91] were measured. Both QDIP (and DWELL) and GaAs/$Al_{0.28}Ga_{0.72}As$ display nearly the same response wavelength in the range from ~ 2 – 10 μm and the gain (or responsivity) of QDs based detectors are higher than that of the GaAs/$Al_{0.28}Ga_{0.72}As$ heterostructure.

3.3 Results and discussion

3.3.1 Dark current and Noise power spectral density

The dark current characteristics and temperature dependence for QDIPs and DWELLs have been investigated and compared to the corresponding noise power spectral density in the detectors to calculate the gain. An important property that brings about noise and a degradation of detector sensitivity is the dark current. Dark current causes noise and a lower dark current lead to a higher detector sensitivity. Hence, insight to noise begins with analysis of dark current. Thermalized carriers transition from bound state in the QD to quasi-bound or continuum state

and contribute to the formation of dark current. Thus, the dark current density can be estimated as,[92]

$$\langle J_d \rangle = 2ev \left(\frac{m^* k_B T}{2\pi\hbar^2}\right)^{3/2} exp\left(-\frac{E_a}{k_B T}\right), \quad (3.1)$$

where e is the electronic charge, v is the drift velocity of holes, k_B is the Boltzmann constant, T is the temperature, $\hbar$ is the reduced Planck constant, and E_a is the activation energy. The transport effective mass m* of holes can be written as[93]

$$m^* = \left(\frac{m_{lh}^{3/2} + m_{hh}^{3/2}}{m_{lh} + m_{hh}}\right)^2 \quad (3.2)$$

The activation energy depends on the total energy of hole transport,[94, 95] and it can be calculated as

$$E_a = E_0 - \beta F, \quad (3.3)$$

where F is the applied electric field intensity, E_0 is the activation energy at zero bias (F = 0 kV/cm), and β is a scaling parameter in the presence of the electric field. The drift velocity is essentially dependent on the electric field,[96] and can be expressed as

$$v = \mu F \left(1 + \left(\frac{\mu F}{v_s}\right)^2\right)^{-1/2} \quad (3.4)$$

where v_s is the saturation velocity of holes and μ is the mobility of holes. Substituting Eq. (3.3) and (3.4) into Eq. (3.1) yields

$$\langle J_d \rangle = 2e\mu F \left(1 + \left(\frac{\mu F}{v_s}\right)^2\right)^{-1/2} \left(\frac{m^* kT}{2\pi\hbar^2}\right)^{3/2} exp\left(-\frac{E_0 - \beta F}{kT}\right) \quad (3.5)$$

This equation 3.5 is fitted to the experimentally measured dark current density for DWELL and QDIP at 77 K as shown in Figure 3.1 (b). The fitting parameters of dark current density for

DWELL and QDIP at 77 K are given in Table 3.1. The values of mobility are in the range of hole mobility for InAs.[97] The saturation velocities are also within the range of saturation velocities of holes for InAs or GaAs.[98]

Table 3.1 Fitting parameters for dark current density at 77 K for DWELL and QDIP structures in the negative bias region. After reference 43.

	DWELL	QDIP
μ (cm^2/V.s)	245	253
V_s (10^6 cm/s)	1.53	2.36
β (10^{-27} m.C)	1.70	2.71

At low temperature, intersubband detectors like QDIP and DWELL usually show no $1/f$ noise contribution due to the unipolar nature of the detectors and the maturity of III-V technology.[99] Hence, the two major noise contributions are Johnson noise and shot or generation-recombination (G-R) noise. Johnson noise is caused by the random thermal motion of charge carriers and at the bias voltage V can be expressed as

$$I_{th}^2 = 4kT\Delta f/\mathcal{R}\,, \tag{3.6}$$

where $\mathcal{R} = \frac{dV}{dI_d}$, I_d is the dark current, T is temperature in degrees Kelvin and Δf is the measurement bandwidth. The excited carrier from the QD levels below the Fermi level can escape to the quasi-bound levels near the continuum, and then tunnel or thermally escape out of the QD; then travel either to the contact or get trapped in another QD or in a shallow barrier state, normally a wetting layer state, from which the carrier can easily escape again. The trapping

can also take place in the excited states of the QD from which the carrier escapes and recombines into the lower QD levels. These emissions and captures are the main cause of the fluctuating number of mobile carriers (or G-R noise) in the dot and well structures where the noise current is related to gain g via the general theoretical description given by Beck[100] as

$$I_{g-r}^2 = 4eg\left(1 - \frac{p_c}{2}\right) I_d \Delta f, \tag{3.7}$$

where p_c is the capture probability of carriers and for N periods, the photoconductive gain is given by $g = 1/Np_c$. If G-R noise and Johnson noise are statistically independent, the total measured white noise power spectral density $S_I(f)$ of photodetector, is given by $S_I(f) = I_{g-r}^2 + I_{th}^2$. However, the thermal noise at the temperatures as low as 78 K (for the case of our detectors) is negligible and hence equation (3.7) yields

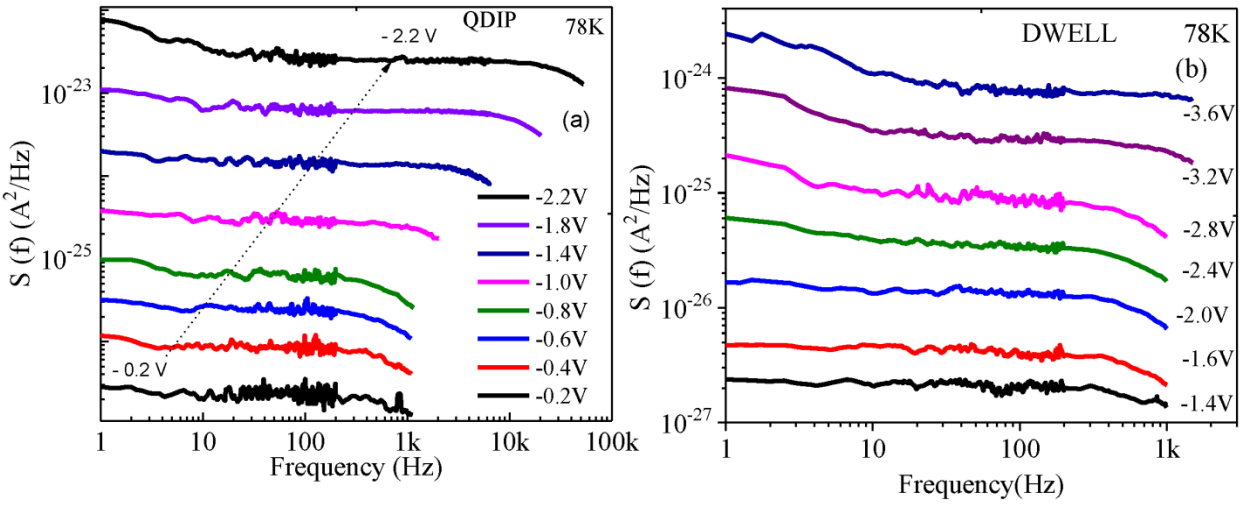

Figure 3.2 Noise power spectral densities of QDIP (a) and DWELL (b) at 78 K for different biases. Both structures display similar noise behavior except the DWELL has lower power spectral density below the noise floor of noise measurement set up for bias voltage below - 1.4V. These noise spectral densities exhibit a linear dependence with external bias voltage; that is shot (G-R) noise. The decreasing tendency of noise spectral density at the highest measurable frequency is due to the bandwidth limitation of low-noise pre-amplifier. Modified After reference 43.

$$g = \frac{I_{g-r}^2}{4eI_d\Delta f} + \frac{1}{2N}. \tag{3.8}$$

The low-frequency current noise power spectral density is usually estimated within the G-R model as,

$$S(f) = 4eg\, I_d. \tag{3.9}$$

It is valid in the range of electric fields and temperatures where statistical correlations between the elementary trapping-detrapping events from quantum dots are negligible. At low temperatures, where $\hbar\omega \gg k_B T$, the quantum zero-point fluctuations will play a more dominant role than the thermal fluctuations. Therefore, at low temperature and low bias, the noise current

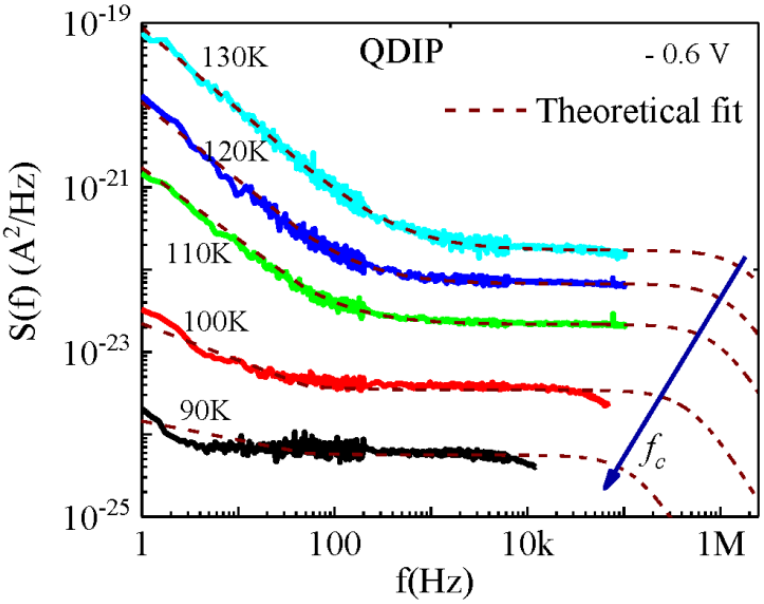

Figure 3.3 Noise power spectral density of QDIP at - 0.6 V and different temperatures. As the temperature increases, *1/f* noise at lower frequency and thermal noise currents will have significant contributions to the noise power spectral density. Similar behavior was seen for DWELL which is not shown here. The dashed lines represent the theoretical fits based on equation 3.10. The arrow shows theoretically fitted cut-off frequency f_c for G-R noise which decreases with decreasing temperature. After reference 43.

appears to be proportional to the dark current and is essentially independent of frequency as shown in Figure 3.2 (a) and (b). Hence, thermally activated G-R processes from the quantum dots, are negligible at low temperature. As a result, the G-R noise, which is characterized by random fluctuations in the current density, is the dominant noise source for QDs based detectors.[89] However, as the temperature increases from ~ 100 K to 130 K, in addition to the G-R noise, the 1/f noise current at lower frequencies and thermal noise currents make significant contributions to the noise power spectral density of the QDIP as shown in Figure 3.3. The noise spectral density has generally a form

$$S(f) = {}^{A}/_{f} + 4qI_d g\left(\frac{1}{1+(f/f_c)^2}\right) + \frac{4k_B T}{\mathcal{R}}, \tag{3.10}$$

where A is a constant (or strength) of 1/f, f_c is the cut-off frequency for G-R noise. The theoretical fits, in Figure 3.3, show that the cut-off frequencies are beyond the bandwidth of experimental measurements. This theoretical fit enables us to predict the cut-off frequency for G-R noise. As temperature decreases from 130 K to 90 K, the cut-off frequency decreases from 2.03×10^6 Hz to 1.45×10^5 Hz as shown by arrow in Figurer 3.3. The noise power spectral density (PSD) of thermal noise is an order of magnitude less than the G-R noise for temperatures shown in Figure 3.4. The PSD of thermal noise at temperatures 90 K, 100 K, 110 K, 120 K, and 130 K are 5.5×10^{-26} A^2/Hz, 4.7×10^{-25} A^2/Hz, 1.5×10^{-24} A^2/Hz, 7.2×10^{-24} A^2/Hz, and 2.1×10^{-23} A^2/Hz, respectively.

Table 3.2 The value of cut-off frequency for fitting parameter A in equation 3.10. The strength of 1/*f* (or A) increases with decreasing cut-off frequency.

Temp(K)	**A (A^2)**	**f_c (HZ)**
90	9.62×10^{-24}	9.45×10^{4}
100	5.62×10^{-23}	1.35×10^{5}
110	1.02×10^{-22}	7.07×10^{5}
120	1.14×10^{-21}	9.25×10^{5}
130	6.51×10^{-20}	1.04×10^{6}

Comparison between the calculated thermal noise limit and measured noise power spectral density of G-R noise at - 0.6 V, 90 K and 100 K for QDIP and DWELL is shown in Figure 3.4. The thermal noise limit is from 1 to 2 orders of magnitudes less than the measured noise power spectral density. As seen in Figure 3.4 (a) or QDIP, the calculated thermal noise limit at - 0.6 V and 100 K is 4.7×10^{-25} A^2/Hz while the corresponding measured noise power spectral density is ~ 3.9×10^{-24} A^2/Hz. Similarly, as seen in Figure 3.4 (b) or DWELL, the calculated thermal noise limit at - 0.6 V and 100 K is 1.4×10^{-27} A^2/Hz while the corresponding measured noise power spectral density is ~ 3.4×10^{-26} A^2/Hz. Based on equation (3.10), for a given temperature, the measured noise power spectral density or the dominant G-R noise depends on dark current I_d, and gain. However, since the gain $g \sim \frac{S_{G-R}}{I_d}$, and the noise spectral density, $S_{G\text{-}R}$ is nearly proportional to the dark current I_d, lowering the dark current do not lead to sigificant change in the gain. Hence, to get the noise spectral density to the level of thermal noise limit, the dark current of the detector must be lowered to the level where the noise spectral density is close or eaqual to the thermal noise limit. However, the thermal noise limit will decrease with the decreasing dark current while the thermal noise limit increases with inceasing temperature.

Therefore, minimizing the noise spectral density to the level of thermal noise limit can be achieved by obtimizing the dark current and operating temperature .

The dark current of QDIP and DWELL can be lowered by growing InAs QDs directly on an AlAs layer of a GaAs/AlAs super lattice, which offers additional miniband confinement. The

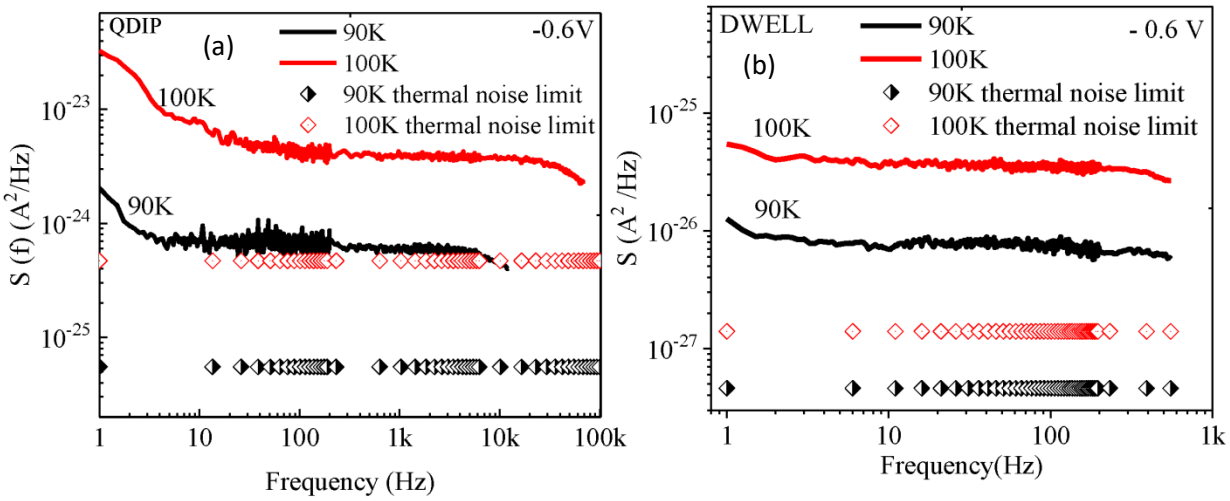

Figure 3.4 (a) Comparison between the calculated thermal noise limit and measured G-R noise at - 0.6 V, 90 K and 100 K for QDIP. (b) Comparison between the calculated thermal noise limit and measured G-R noise at - 0.6 V, 90 K and 100 K for DWELL.

additional minibands confinement due to Al(Ga)As will enhances 3 – 5 μm responses and lower dark current (or enhances detectivity and elevate operating temperatures). In addition to low dark current, in the growth process, due to the reduced mobility of Al compared to In, the dot density increased as a result of the altered adatom kinetics.[101, 102] QD layers grown on AlAs under similar growth conditions demonstrated dot density ten times higher than that on GaAs.[19]

Another structural design that minimize the dark current is an optimized Al(Ga)As dark current blocking layer with little effect on photocurrent (responsivity). Thin Al(Ga)As blocking layer reduces the dark current much more than the response signals.[19, 103] The dark current is reduced by over three orders of magnitude using a thin AlGaAs current blocking layer.[103]

To get further insights into the detector capture or relaxation properties, we measured the noise power spectral density, S(*f*) which is nearly proportional to dark current. Then, extract the gain from the experimentally measured G-R noise and dark current using equation (3.8). The band width of measurement is limited by Low-noise pre-amplifier gain that rolls off at higher frequencies. The gain roll-off frequency of pre-amplifier depends on the impedance to be measured. Therefore, at low bias and low temperature, where the impedance of detectors is as high as ~ 1 - 10 M-ohm, the bandwidth of the measurement is limited to a frequency of ~ 100 Hz as shown in Figure 3.2. However, for low impedance conditions (high temperature and high bias), up to 102.4 kHz band width is measured as shown in Figure 3.3.

3.3.2 Carrier scattering in heterostructures versus that in QDs based detectors

The carrier scattering or capture probability determines the responsivity through the photoconductive gain. In a typical semiconductor, the electrons and holes scatter via longitudinal optical (LO) phonon and longitudinal acoustic (LA) phonon emission. But the LO phonons are highly monochromatic (~ 30 meV in InAs, ~ 36 meV in GaAs, and ~ 46 meV in AlAs)[104]. Thus, the carrier relaxation probability through LO phonon scattering is largely reduced in QD structures due to discrete energy levels, and the carrier's relaxation time from excited states increases. Acoustic phonon scattering is also reduced because of the conservation of both energy and momentum between discrete energy levels within a QD (The LA phonon energy is 3 meV when the wavelength of the acoustic phonon is of approximately the QD diameter).

In GaAs/AlGaAs heterostructures where there is no energy confinement, both LO and LA phonon emissions cannot be ruled out. Hence, the key advantage of QDs based detectors is the longer carrier relaxation time due to the existence of discrete energy levels that hamper phonon assisted carrier scattering,[104, 105] the so-called ‘‘phonon bottleneck”. Experimental results

showed that carriers within heterostructures relax much faster than that in QDs and consequently they have lower gain. Figure 3.5, shows a comparison of measured dark current gains between QDs based structures and GaAs/$Al_{0.28}Ga_{0.72}$ As heterostructures. Due to the suppression of the phonon scattering mechanism in QD structures, carriers in both QDIP and DWELL have higher

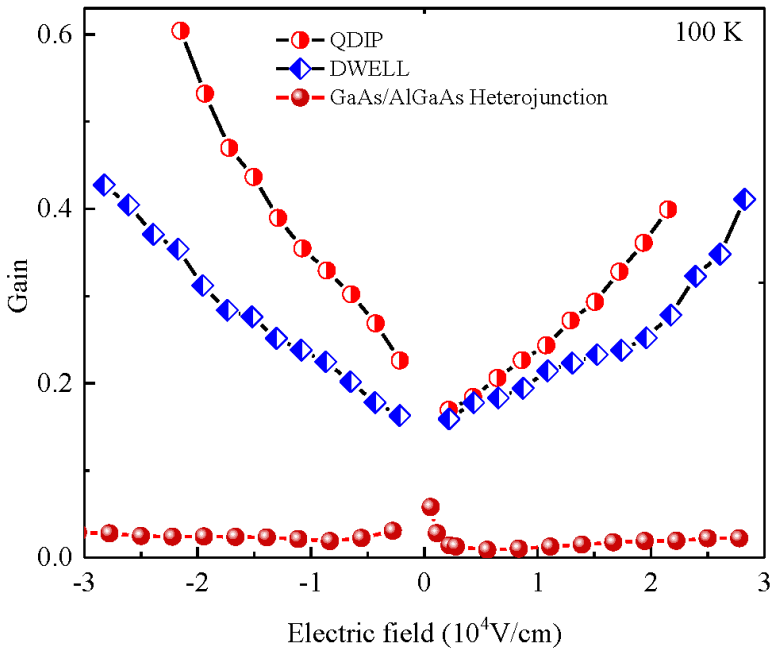

Figure 3.5 Comparison of experimentally measured gain between QDs structures and GaAs/$Al_{0.28}Ga_{0.72}$As heterostructure. Since the phonon scattering mechanism is reduced in QD structures, both QDIP and DWELL exhibit higher gain as compared to the GaAs/$Al_{0.28}Ga_{0.72}$As heterostructure due to the longer carriers' lifetime. After reference 43.

lifetime as compared to heterostructures with a similar response wavelength range, ~ 2 μm – 10 μm. Thus, the experimentally measured gain of QDIP and DWELL is significantly larger than that of GaAs/$Al_{0.28}Ga_{0.72}$As (Figure 3.5). Similarly, comparison of responsivity between QDs based and GaAs/AlGaAs heterostructure detectors is shwon in Figure 1.5 (b).

3.3.3 Gain and capture probability

The crucial characteristics of QDs based IR detectors are determined almost entirely by the photo-generation rate of carriers out of the QDs and the recapture (or capture probability) into the QDs and QWs. The capture probability (p_c) determines the responsivity through the photoconductive gain. The gain and hole capture probability can thus be calculated using equation (3.7) and (3.8). Figure 3.6 shows the experimentally measured gain comparison between QDIP and DWELL. The gain values of QDIP are higher than the corresponding DWELL sample. DWELL has additional confinements in the well that result in additional transitions between bound to bound states, which has higher capture probability as compared to

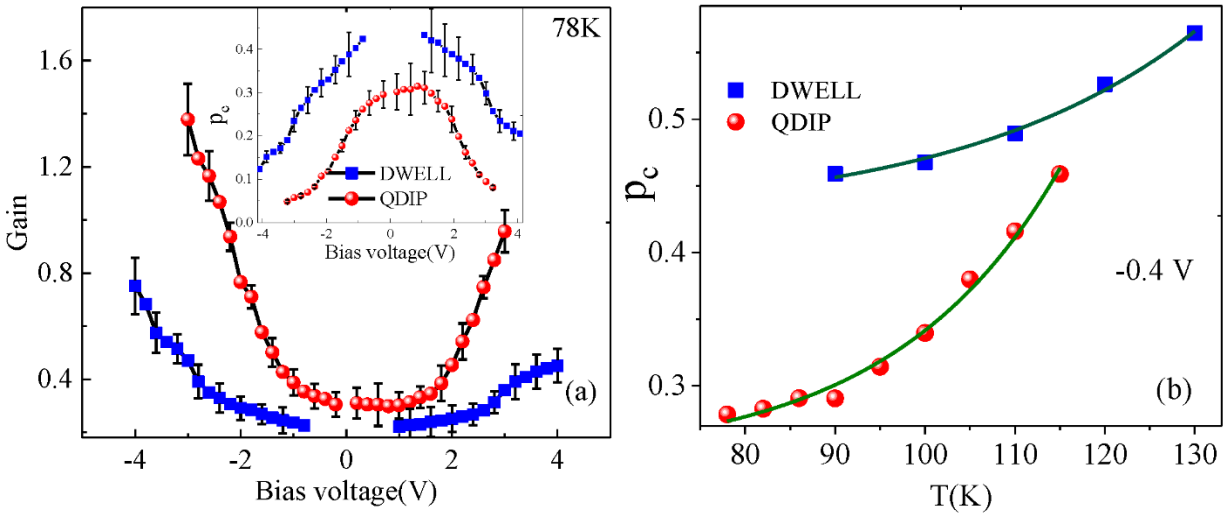

Figure 3.6 Comparison of gain between QDIP and DWELL. QDIP has higher gain values as compared to DWELL. The inset shows DWELL has higher capture probability (p_c) than the corresponding QDIP. (b) Experimentally measured capture probability (dotted lines) of holes at bias voltage - 0.4 V and different temperature. The solid line is the exponential fits of capture probabilities of QDIP and DWELL. Hence, the capture probability increases exponentially with temperature. Modified after reference 43.

transition between bound to quasi-bound or continuum. Thus, DWELL has about two times higher capture probability than the corresponding QDIP as shown in Figure 3.6 inset. As

indicated in Figure 3.6 (b), the capture probability, p_c increases as the temperature increases. Although the total number of states remain constant, due to thermal emission, the number of unoccupied hole states in the QDs increases with temperature, and hence p_c increases with a rate proportional to e^{E_i/k_BT}.

The capture probability can also be defined as $p_c = {\tau_t}/{\tau_{rec}}$, where τ_t is the sweep-out or transit time and τ_{rec} is the recombination time (lifetime). The transit time is given by[106, 107],

$$\tau_t = h_{QD}\frac{\sqrt{1+\left({\mu F}/{v_s}\right)^2}}{\mu F}, \tag{3.11}$$

where h_{QD} is QD height, and v_s is saturation velocity of holes. The recombination (life) time is[107]

$$\tau_{rec} = \frac{(N+1)L}{\pi a_{QD}^2 h_{QD}\Sigma_{QD}V_t}, \tag{3.12}$$

where N is the number of QD layers, a_{QD} is the lateral dimension of QD, L is spacing between the QDs layers, Σ_{QD} is surface density of QDs and V_t is the capture rate of holes. In the case when $\tau_t \ll \tau_{rec}$, the capture probability p_c is low, and the gain has the conventional expression as,

$$g = \frac{\tau_{rec}}{N\tau_t} = \frac{(N+1)L\mu F}{N\pi a_{QD}^2 h_{QD}^2 \Sigma_{QD} V_t\left(1+\left({\mu F}/{v_s}\right)^2\right)^{1/2}}. \tag{3.13}$$

Based on equation 3.12, it is possible to see that optimizing the structural parameters such as the QDs density Σ_{QD}, barrier thickness L, number of QD layers N, QDs and barrier materials, and tuning the bias voltage *F(V)* allow to minimize the capture probability and improve the gain of QDIP and DWELL.

The 3D plot of capture probability (p_c) versus gain versus bias voltage for QDIP and DWELL for bias voltages from - 3.0 V to 3.0 V is shown in Figure 3.7. For QDIP, a maximum gain of 1.4 was obtained at - 3.0 V with capture probability (least) of 0.05; and a minimum gain of 0.31 was obtained at + 0.2 V with capture probability of 0.3. Similarly, DWELL's gain follows the same variation with capture probability except that DWELL has lower gain values as

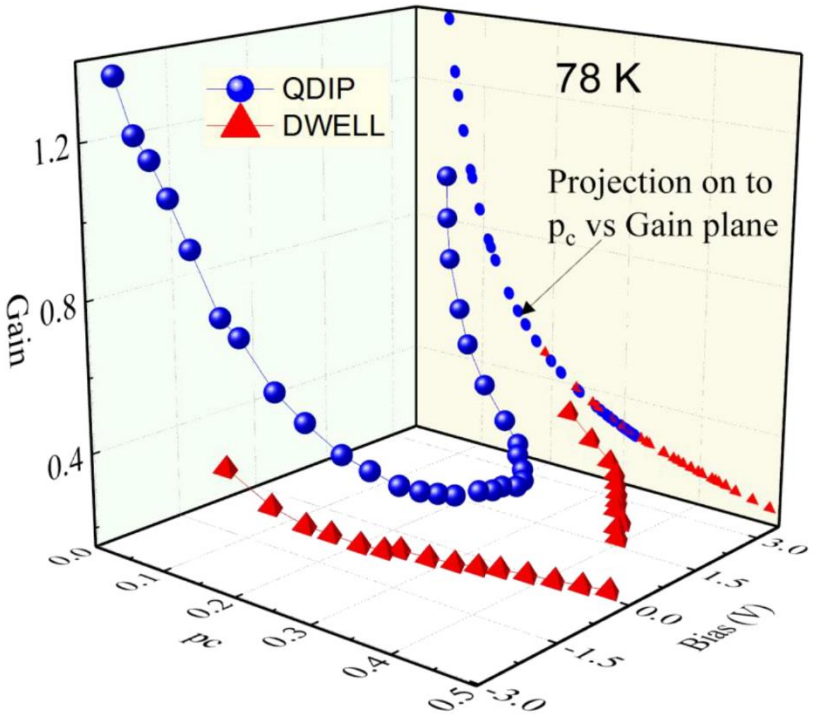

Figure 3.7 A 3D plot of capture probability (p_c) versus gain versus bias voltage for QDIP and DWELL for bias voltages from - 3.0 V to 3.0 V. For QDIP a maximum gain of 1.4 was obtained at - 3.0 V with the least capture probability of 0.05; and a minimum gain of 0.31 was obtained at + 0.2 V with capture probability of 0.3. Similarly, the reflection of 3D plot on gain-pc plane shows, DWELL's gain follows the same variation with capture probability except DWELL has lower gain values as compared to the corresponding QDIP.

compared to the corresponding QDIP as expected (see the reflection of 3D plot on gain-capture probability plane).

Since both gain and capture probability are expressed in terms of material and structural parameters in equations 3.13 and 3.14, it is possible to optimize the detector for higher gain (or responsivity, $R \propto g$). Hence, material with high mobility, greater number of QDs layers with optimized total thickness, thickness of barrier (80 nm for GaAs) are some of the parameters that improve detectors performance.

Combinations of equations (3.5), (3.9), and (3.13) yield the expression for noise power spectral density as

$$S(V) = \frac{8e^2\mu^2F^2(V)(N+1)LA\left(\frac{m^*kT}{2\pi\hbar^2}\right)^{3/2} exp\left(-\frac{E_0-\beta F(V)}{kT}\right)}{N\pi a_{QD}^2 h_{QD}^2 \Sigma_{QD} V_t\left(1+\left(\frac{\mu F(V)}{v_s}\right)^2\right)^{1/2}}. \quad (3.14)$$

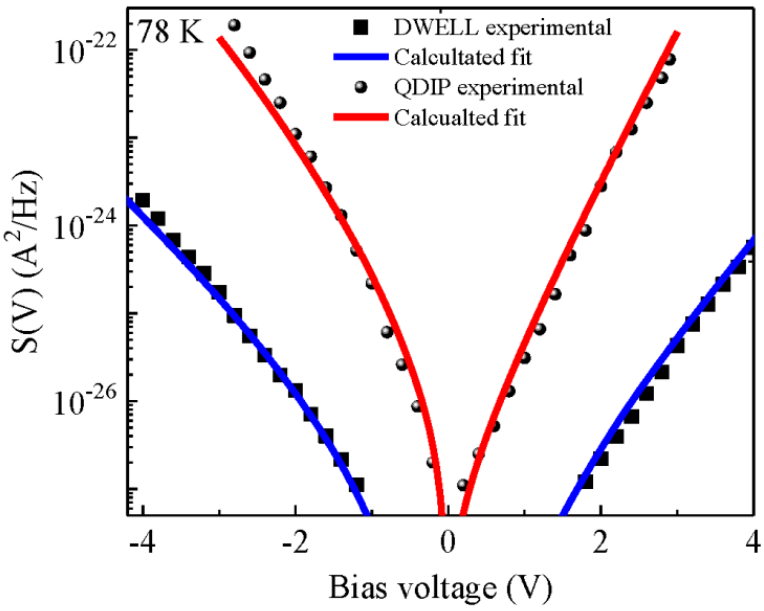

Figure 3.8 Theoretical fits to the experimental data for both QDIP (G12-133) and DWELL (G12-134) samples. The constant parameters are N = 10, L = 80 nm, a_{QD} = 20 nm, h_{QD} = 5 nm, Σ_{QD} = 5 × 10^{10} cm^{-2}, and $E_o = 0.254\ eV$. See Table 3.2 for the fitting parameters. The fitting parameters of the dark current density (Figure 3.1 (b)) and the noise power spectral density are nearly the same in each of the structures. After reference 43.

This theoretical expression for noise power spectral density for both negative and positive bias regions fits well with the experimental data with fitting parameters in Table 3.2 as shown in Figure 3.8.

The fitting parameters of the dark current density shown in Figure 3.1 (b) and the corresponding negative biases noise power spectral density in Figure 3.7 are nearly the same. The differences in the fitting parameters for negative (-ve) and positive (+ve) biases are due to unintentional asymmetry in the both QDIP and DWELL structures. In complex QDIP and DWELL structures, the values of mobility and saturation velocity determined by fitting are in the range of the corresponding values for bulk GaAs. Since both detectors have lower resistance for negative bias as compared to that of corresponding positive bias, the negative bias V_s and μ are higher than the corresponding positive bias.

Table 3.3 Fitting parameters for noise power spectral density of DWELL and QDIP at 78 K. After reference 43.

	DWELL(G12-134)		QDIP(G12-133)	
	-ve bias	+ve bias	-ve bias	+ve bias
μ (cm^2/V.s)	215	95	246	217
V_s(10^6 cm/s)	1.43	1.35	2.27	2.25
V_t (10^5 s^{-1}m)	200	195	2.98	2.40
β (m.C)	1.98	2.45	3.01	3.58

Furthermore, the theoretical fit to the noise power spectral density reveals that the capture rate of DWELL is higher than the corresponding QDIP, which agrees with the capture probabilities (inset of Figure 3.6) obtained from experimentally measured gain. However, DWELL architecture offers additional advantages over QDIP detectors, such as superior optical

quality of the quantum dots due to strain relaxation[108, 109] in the InGaAs QW, and the ability to independently control the ground state and excited state energy levels in obtaining the bound to quasi-bound transitions for optimizing the capture probability. Additionally, the optimized bound-quasibound transition based detector can be further improved by the introduction of confinement enhancing barriers, such as resonant tunneling barriers around the DWELL region[96], which selectively block the dark current while allowing the photocurrents of the desired wavelengths to pass. This implies that the asset of DWELL structures deserves further research on the relevant carrier capture and relaxation mechanisms to improve the gain.

3.4 Summary

The comparison between QDIP and DWELL based on noise power spectral densities and dark current gains are experimentally determined. At lower temperature (below ~ 100 K) and low bias, the noise current of these detectors is dominated by generation-recombination (G-R) noise. The dark current noise gain, capture probability and carriers' lifetime for bound-to-continuum or quasi-bound transitions in both DWELL and QDIPs structures are compared. The capture probability of DWELL is found to be more than two times higher than the corresponding QDIP. The structural parameters such as the numbers of active layers, the surface density of QDs, and the carrier capture or relaxation rate, type of material and electric field are some of the optimization parameters identified to improve the photoconductive gain of the detectors.

4. ACCURACY OF ACTIVATION ENERGY VALUES OBTAINED FROM ARRHENIUS PLOT AND TEMPERATURE-DEPENDENT INTERNAL PHOTOEMISSION SPECTROSCOPY

4.1 Introduction

In the infrared (IR) photodetectors, radiation incident on the sample excite the carriers (holes or electrons) from the ground or lower excited states to the edge of the barrier, where it either relax back to the lower energy state or cause the photocurrent in the growth direction. The minimum energy for the photoexcited carrier to overcome the barrier and contribute to the photocurrent is the activation energy Δ. The threshold wavelength, λ_t, is one of the most important parameters from a detector operational point of view. This wavelength threshold of a photodetector is related to activation energy, $\Delta(eV) = 1.24/\lambda_t(\mu m)$. The design for different threshold wavelengths in IR detectors involves the selection of an appropriate potential barrier[110] and adjusting the Fermi level by changing the carrier concentration[111] or doping. A high doping density not only decreases the activation energy or increases the threshold wavelength but also increases the impurity scattering for the photoelectrons.

The characteristics of the dark current and photocurrent depend up on the thickness, height, and type of materials of the barrier. High barrier or activation energy reduces the dark current and extends the dominant region of the thermionic emission current. This barrier height can be obtained from the current-voltage-temperature (*I-V-T*) properties, the capacitance-voltage-temperature (*C-V-T*) properties, and temperature-dependent internal-photoemission spectroscopy (TDIPS)[112] based on measured spectral responses or quantum yield. The comparison and differences between the apparent barrier heights obtained from *C-V-T* and *I-V-T* measurements are discussed in Song, et al[113, 114] and others.

In this study, I compared two methods of determining the threshold wavelength or activation energy of *p*-type GaAs/$Al_xGa_{1-x}As$ to underline their respective advantages and disadvantages. The first method is based on the well-known Arrhenius analysis (or Richardson's plot) of the experimentally measured *I*-*V*-*T* characteristics of the detectors. The thermionic emission (TE) model (Richardson-Dushman equation) for dark current at different temperature is used to investigate activation energy (threshold wavelength) at low electric field, while the Fowler-Nordheim (FN) or electric field emission (FE) models are briefly discussed at high electric fields.

The temperature dependence of *I*-*V* or the Arrhenius plot is utilized to extract the activation energy which provides information to predict the threshold wavelength for the spectral response of detectors without carrying out spectral measurements. However, the Arrhenius plot based on the standard thermionic emission theory predicts temperature independence of the barrier height[115] while this is not always the case experimentally. Hence, it is not always possible to determine the activation energy accurately for detectors displaying the non-Arrhenius behaviors, such as strong temperature dependence of barrier height, tunneling and diffusion limited currents.

The temperature dependence of band offset is evident and the effect of neglecting the temperature dependence of activation energy (band offset) was revealed[112, 116, 117] in the past decade and studied by internal photoemission (IPE) methods.[112, 118] The temperature-dependent internal-photoemission spectroscopy (TDIPS)[112] technique is one of the methods based on the IPE process. IPE spectroscopy has been extensively used[112, 119, 120] to determine the interfacial barrier height (Δ) of different materials which defines the detector cutoff wavelength, λ_t as a function of detector parameters, temperature, and applied voltage**.** TDIPS is currently the most

reliable[112] tool available and is used effectively to characterize the band offset parameters of different materials such as type-II InAs/GaSb superlattice (T2SL)[121, 122] and MCT detectors,[122-124] GaAs/AlGaAs heterojunctions,[112, 122, 125, 126] PtSi–Si diodes,[127] and a graphene-insulator-semiconductor structures.[119, 120]

The part of photons absorbed by a detector contributes to the excited holes or photocurrent while the other part relaxes back to its lower energy states. The IPE process can be characterized by the quantum yield, defined as the number of emitted carriers per absorbed photons. Hence, the quantum yield in TDIPS is proportional to the product of measured spectral responsivity and photon energy.[91] Then, to obtain the activation energy or photoemission threshold (Δ), fittings to the yield spectra can be carried out in the near-threshold regime at different temperatures. In the expression for quantum yield spectra, the transmission probability of carriers over the barrier, energy distribution function, and the temperature dependent band tailing effects are included. The carriers escape over the (AlGaAs in our case) barriers through an internal photoemission process and hence, TDIPS is sensitive to the temperature dependence of band offsets[112] (which is not possible in the Arrhenius analysis).

The advantage of TDIPS fittings is that only the spectral shape of measured quantum yield close to threshold wavelength determines the activation energy. Since the thermionic emission current is independent of the photon energy and only gives a constant background signal, the background can be distinguished from the yield spectra by fitting the theoretical expression to the measured photoemission yield component alone. Although our data is mainly based on GaAs/AlGaAs structure, the results are generally valid for any semiconductor detectors where the threshold wavelength depends on the activation energy.

Six *p*-type GaAs/$Al_xGa_{1-x}As$ detectors with different Al mole fractions and doping levels were investigated. The detailed intra-band transitions of holes in *p*-type GaAs/AlGaAs[91] and the temperature dependence of the band offset are revealed using the TDIPS fitting[112] technique. Therefore, the focus of this study is a comparison between the activation energies determined by Arrhenius analysis and TDIPS fittings to underline the advantages/disadvantages of one over another in different temperature ranges for different barrier heights. The significant discrepancy in the values of the activation energy determined by Arrhenius technique and TDIPS fitting for a detector with a long threshold wavelength ($\gg 9.3\ \mu m$) arises because the Arrhenius analysis does not take the band tailing effect (sensitive to temperature variation) in to account. In addition, the Fowler–Nordheim (FN) tunneling current cannot be ignored for shallow barrier heights, as is done for the thermionic emission model used for the Arrhenius analysis.

4.2 Detectors structures and experimental procedures

A set of six *p*-type GaAs/$Al_xGa_{1-x}As$ heterostructure samples were grown with molecular beam epitaxy. The detectors demonstrated here were heterojunction interfacial work function internal photoemission (HEIWIP) detector which consists of alternative layers of highly *p*-doped absorbing GaAs (emitters) and undoped $Al_xGa_{1-x}As$ barriers. The active GaAs/$Al_xGa_{1-x}As$ regions were sandwiched between top and bottom (p^+-GaAs) ohmic contact layers. The highly *p*-doped and 18.8 nm thick GaAs emitters have three-dimensional energy states and heavy holes (HH)/light holes (LH) which are excited by incoming radiations as reported by Lao, et al.[91] Then these carriers escape over the AlGaAs barriers through an internal photoemission process occurring at the emitter-barrier interface. The internal work function is defined by energy difference between the barrier bottom and the Fermi level (or the valence-band edge if the Fermi level is above it) of emitters, and it determines the threshold wavelength λ_t.

In GaAs/$Al_xGa_{1-x}As$ heterostructures, the doping density in the GaAs layers and the aluminum mole fraction (*x*), in the $Al_xGa_{1-x}As$ layers were some of the key factors that affect the mechanism or magnitudes of the dark current and photocurrent. Two important sets of experimental results based on doping and Al mole fraction had been compared (see Table 4.1). The first group was three heterostructures with the barrier having three values of *x*, which give rise to three different barrier heights. The Al mole fractions for the $Al_xGa_{1-x}As$ barrier in detectors SP1, SP2, and SP3 were 0.28, 0.37, and 0.57 respectively. In the second group, structures had three different doping levels. SP1, LH1001, and LH1003 had the doping levels of 3×10^{18} cm^{-3}, 8×10^{18} cm^{-3}, and 6×10^{19} cm^{-3} respectively, while the other parameters were kept the same. The valence band profile of the unbiased GaAs/$Al_xGa_{1-x}As$ is shown in Figure 4.1. All the important parameters for various detectors are summarized in Table 4.1.

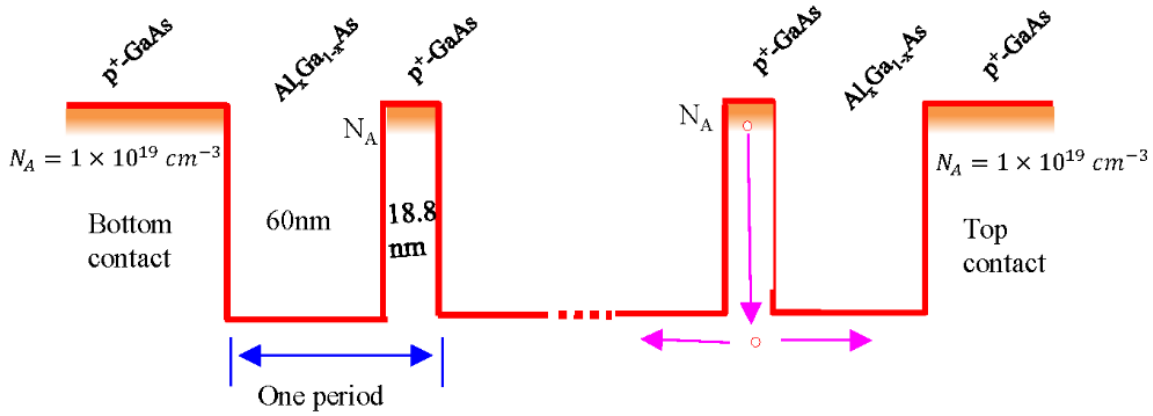

Figure 4.1 Schematic of the unbiased valence band profile for the *p*-type GaAs/$Al_xGa_{1-x}As$ heterostructures used to study the activation energy different barrier heights and doping levels at zero bias. There are 30 periods in all samples. The Al mole fraction *x* and doping levels N_A are given in Table 4.1.

The detectors were fabricated into square mesas of 400×400 μm^2 with an optical window of 260×260 μm^2 which allows front-side illumination. To characterize the detector, the square mesas and the ohmic contacts on the top and bottom layers were fabricated using standard wet

chemical etching. Then the detector was mounted on the cold head of a liquid nitrogen-cooled Dewar and liquid helium-cooled cryostat to allow measurements of spectral response and dark current. Spectral measurements in the IR region for normal incidence radiation were carried out using a Perkin Elmer System 2000 Fourier transform infrared (FTIR) spectrometer while the dark current measurements were performed using a Keithley 2400 source meter.

The temperatures were controlled and varied from 10 K to 300 K using a Lake Shore 330 Auto tuning Temperature Controller with an accuracy of ± 0.01 K. A calibration of the sample temperature may be required if absorption of infrared light and position of temperature sensor causes appreciable temperature variations in the samples. However, such a variation is negligible in our experiment, as our temperature controller typically has the stabilization accuracy of < ± 0.1 K.

Table 4.1 Parameters for samples under discussion. SP1, SP2, and SP3 vary only in Al mole fraction while SP1, LH1001, and LH1003 have nearly the parameters and vary in their doping levels.

Sample	Al Fraction	Barrier Thickness (nm)	Emitter Thickness (nm)	Doping $N_A(cm^{-3})$	Number of periods	Designed band offset(eV) at 78 K
SP1	0.28	60	18.8	3×10^{18}	30	0.157
SP2	0.37	60	18.8	3×10^{18}	30	0.207
SP3	0.57	60	18.8	3×10^{18}	30	0.319
LH1001	0.28	60	20	8×10^{18}	30	0.157
LH1003	0.28	60	20	6×10^{19}	30	0.157
LH1004	0.57	60	18.8	1×10^{19}	30	0.319

4.3 Results and discussion

The temperature dependent spectral responses and I-V curves were measured at different temperatures. The temperature dependent spectral response shows a red-shift of detector threshold wavelength with increasing temperature. The interfacial barrier height (activation energy) was extracted from the measured spectral response and I-V-T data using TDIPS fitting and Arrhenius analysis respectively. Arrhenius (or Richardson's plot) analysis gives valid results only for the temperature range where the thermionic emission is dominant and field emission (tunneling through the barrier) is negligible. For the holes, pure tunneling through 60nm (thick) AlGaAs barrier is assumed to be negligible. Therefore, different analytical dark current models, such as thermionic emission (TE), thermally assisted field emission (TFE) (or Fowler-Nordheim (FN) emission), and field enhanced thermal or Frenkel-Pool (FP) emission were briefly discussed for experimentally measured I-V-T data.

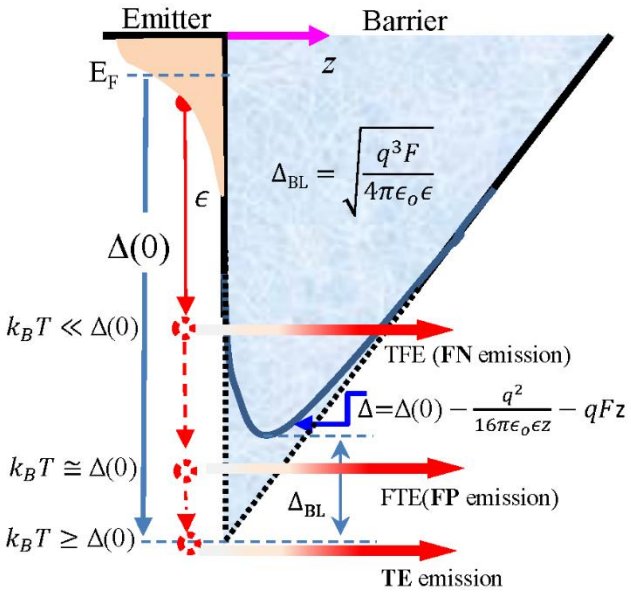

Figure 4.2 The highly *p*-type doped GaAs (emitter) and AlGaAs (barrier) interfacial valence band profile under the influence of an electric field. Assuming negligible pure tunneling current, the three transmission currents are due to thermally assisted (FN) emission, field enhanced (FP) thermal emission and thermal emission (TE).

4.3.1 Thermionic emission

Thermal emission is a process in which the thermal energy yields non-zero holes density at energies larger than the potential barrier allowing them to escape. At low electric fields, for pure ohmic behavior, the slope of ln(*J*) versus ln(*V*) approaches unity. At low field and high temperature, thermally excited carriers yield current with ohmic characteristics that exponentially dependent on temperature. The current-voltage characteristics may be essentially assumed by the Richardson-Dushman model of thermionic emission, in which the carrier acquires a thermal energy sufficient to cross the barrier because of the superposition of the external electric field and the image charge potential. This model is usually valid at lower fields and higher temperatures. The Richardson-Dushman model that physically justifies the temperature dependence of dark current density *J* is given by

$$J = AT^{3/2}\exp(-\Delta/k_B T), \tag{4.1}$$

where the Δ is the activation energy and *A* is effective Richardson constant. At higher fields, the barrier height for thermionic emission is reduced, thus lowering the barrier height (due to Field and image force). This effect is termed as Frenkel–Poole (FP) or Field-assisted thermal emission (FTE) as shown in Figure 4.2. The activation energy in equation (4.1), with image force lowering considered, may be written as

$$\Delta = \Delta(0) - \sqrt{\frac{q^3 F}{4\pi\epsilon_0 \epsilon}}, \tag{4.2}$$

where $\Delta(0)$, F, ε_o, ε are the interface potential barrier height or zero-field emission barrier height, the electric field, vacuum permittivity, and dielectric constant, respectively. As can be noted from equation (4.1), the slopes of $\ln(J/T^{3/2})$ versus $1/k_B T$ at different voltages should be

straight lines at high temperatures ranges. Hence, for a given electric field, the activation energy can be determined from experimentally measured *J-V* Arrhenius plot as

$$\Delta = \frac{d(J/T^{3/2})}{d(k_B T)}. \tag{4.3}$$

This method is particularly valid for thermionic emission dominated behavior over a wide temperature range where the temperature dependence of the activation energy and tunneling current can be neglected. The two possible hypotheses that explain non-linearity of the ln ($J/T^{3/2}$) vs $1/k_BT$ plot are a strong temperature dependence of barrier height which is not taken in to account in the 3D drift current density model of thermal emissions and electric field assisted tunneling current, and/or a combination of the two effects.

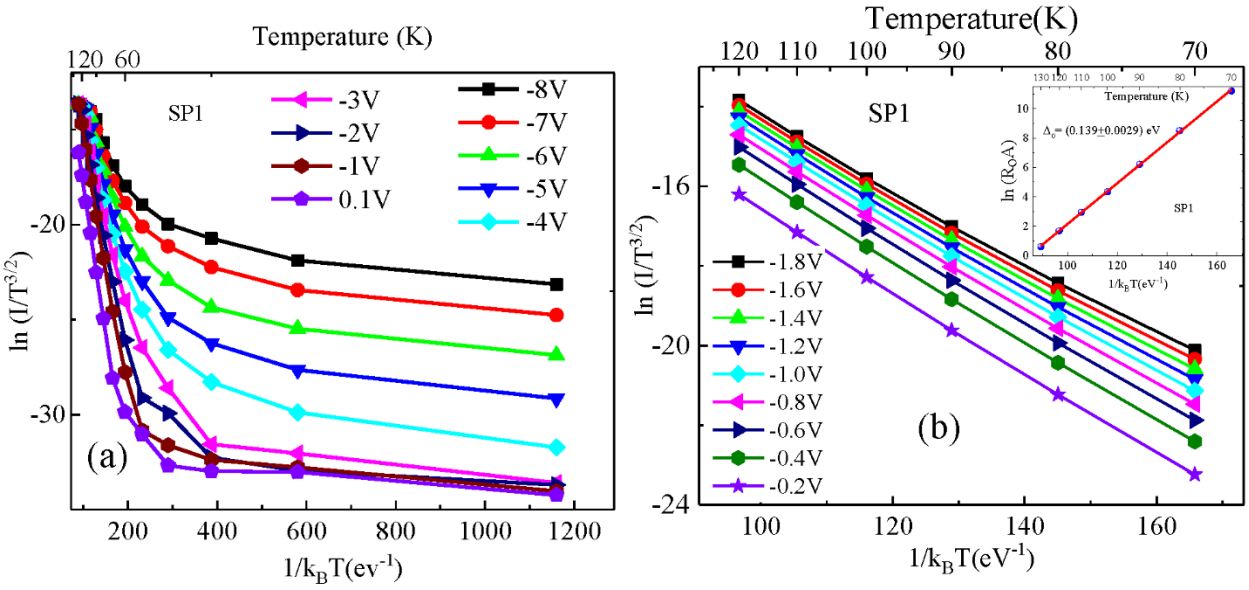

Figure 4.3 Arrhenius plot for SP1 which has an Al fraction of 0.28 for (a) the whole temperature ranges and (b) temperatures range from 70 - 120 K. The inset in (b) shows the Arrhenius plot for the relation $ln(\mathcal{R}_o A) \sim exp(-\Delta_0/k_B T)$.

Figure 4.3 (a) shows the ln ($J/T^{3/2}$) vs $1/k_BT$ characteristics for experimentally measured *I-V* for temperatures in the range10 – 130 K over a wide bias voltage range (0.1 - 8 V). For SP1 (x = 0.28) and for temperature higher than 70 K, excellent linear fits were obtained (see Figure 4.3 (b)) and this suggests that the exponential increase in the dark current with temperature is due to carrier thermal excitation to the higher energy states. In Figure 4.3 (a), for temperature lower than 70 K, the dark current density is relatively insensitive to temperature and is an attribute of phonon and electric field assisted tunneling. The activation energy of the dark current-voltage characteristics at zero electric field is also calculated using the Arrhenius plot for the relation $\mathcal{R}_o A \sim \exp(\Delta_0/K_B T)$ where $\mathcal{R}_o = \left(\frac{dJ}{dV}\right)^{-1}_{V=0}$ and A is the total area of the detector.

4.3.2 Temperature-Dependent Internal-Photoemission Spectroscopy (TDIPS)

To understand the magnitude of temperature dependence of the band offset $\frac{\partial \Delta E_V}{\partial T}$, or activation energy $\frac{\partial \Delta}{\partial T}$, the spectral responses were measured at different temperatures. The valence band offsets (ΔE_v) of *p*-type GaAs/$Al_xGa_{1-x}As$ heterostructures (Table 4.1) and their temperature dependence were obtained through analyzing quantum yield spectra calculated from measured responses at different temperatures. The quantum yield is proportional to the product of photon energy and measured spectral response.[91, 112] The spectral shape of the quantum yield near the threshold regime plays the crucial role to determine the activation energy. Therefore, the dominant processes affecting the energy distribution of carriers and their escape probabilities across the interface will lead to the required expression for the quantum yield. The quantum yield Y($h\nu$) in terms of the photoexcitation of holes in the emitter through inter-valence-band (IVB) transitions,[91] described by an energy distribution function $\rho(\epsilon, h\nu - E_F)$, and is given by the transmission of holes over the barrier, described by a probability function of $P(\epsilon, \Delta)$ reads as [112]

$$Y(h\upsilon) = Y_0(KT) + C_0 \int_{\Delta}^{\infty} \rho\,(\epsilon,\ h\nu - E_F)\ \ f(\epsilon,\ h\nu)\, P(\epsilon, \Delta) d\epsilon \qquad (4.4)$$

where C_0 is a constant independent of ϵ and $h\nu$. ϵ is the energy of photoexcited holes. Δ is the required activation energy. The energy is scaled downward with the zero reference at the Fermi level. Equation (4.4) describes the case of degenerate (highly) doped emitters (E_f lying within the VB). At non-zero temperature, carriers occupy energy states above the Fermi level in terms of the Fermi-Dirac (FD) statistics. An FD function $f(\epsilon, h\nu) = [1 + \exp(\epsilon - h\nu)\,/KT]^{-1}$ was used as the distribution function. This assumes that photoexcited holes remain in the same distribution as that before photoexcitation, with the only difference being energy $h\nu$.

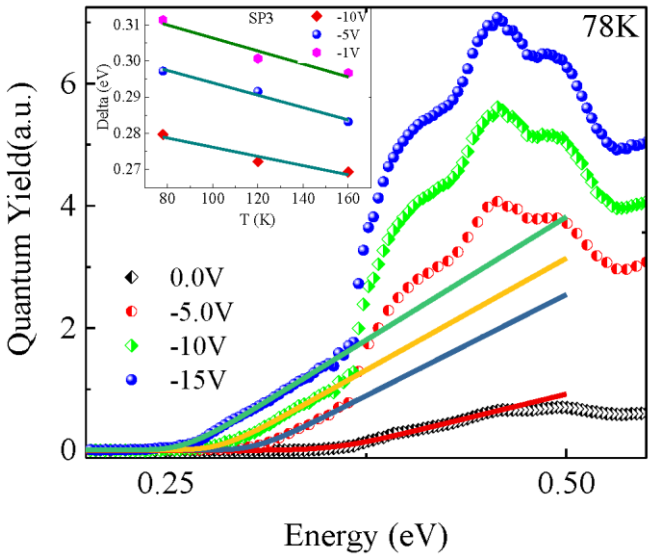

Figure 4.4 Solid lines are TDIPS fitting for spectral response of SP3 at 78 K for four different biases. The activation energy value was determined from TDIPS fitting to the lowest energy range of the measured quantum yield in arbitrary unit. Inset shows the temperature dependence of activation energy based on TDIPS fittings to the experimentally measured response spectra t different temperatures.

To obtain the photoemission threshold (Δ), fittings to the yield spectra (~ product of photon energy and response) were carried out in the near-threshold regime by using Equation (4.4) and

the Levenberg-Marquardt fitting algorithm, where Y_0, C_0, and Δ are regarded as fitting parameters. E_f was determined by carrying out an 8 × 8 ***k.p*** computation[128] and integrating the product of density of state by the FD distribution function over the entire range of energies.

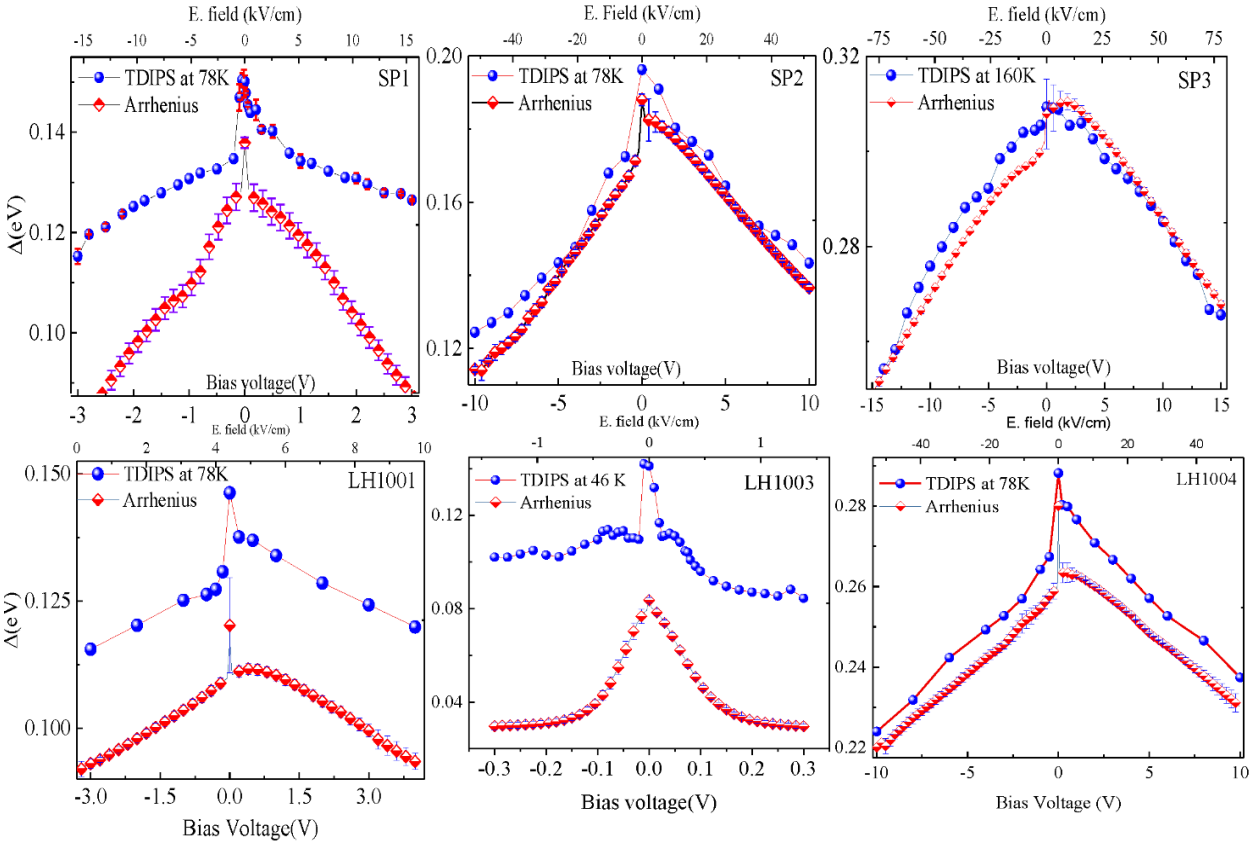

Figure 4.5 Comparisons between activation energies determined by TDIPS fitting and Arrhenius plot for samples with different Al fraction, and doping levels. SP1, SP2, SP3 have different Al fraction, and SP1 with least Al fraction (or least barrier height) displays significant disparity. SP1, LH1001, and LH1003 have different doping levels while nearly same other parameters. The threshold wavelengths for these devices are longer than ~ 9.3 μm and the activation energy determined by the Arrhenius plot is very different from the TDIPS fitting results. The activation energy determined by the Arrhenius plot for devices with shorter threshold wavelength (<< ~ 9.3 μm), SP2, SP3, and LH1004, agree well with the measured threshold spectral response.

Based on TDIPS fitting results, the valence band off-set of $GaAs/Al_xGa_{1-x}As$ heterostructures (in eV) is given by[112] $\Delta E_V = (0.57 - 1.39 \times 10^{-4} \times T)x$, where T is in Kelvin. The activation energy or photoemission threshold at 0V is then given by $\Delta(0V) = \Delta E_v - \Delta_{BL} - E_f$, where Δ_{BL} is the barrier lowering due to electric field and image force as shown in Figure 4.2. In Figure 4.4, the solid lines show TDIPS fittings to spectral responses of SP3 at 78 K for different bias voltages and the inset shows the temperature dependence of activation energy based on TDIPS fittings to experimentally calculated quantum yield from the measured spectral response.

The activation energy decreases (redshift) with the increase in bias in an exponential form, due likely to energy band bending[129, 130] and with increasing temperature due to band gap narrowing. Figure 4.5 shows the activation energies extracted from the Arrhenius plot and TDIPS fitting for samples described in Table 4.1.

4.3.3 Temperature dependent Fermi distribution and tail effect

The extrinsic carrier concentration or doping level is of fundamental importance to characterize the detector threshold wave length. For highly doped detector, the threshold wavelength increases with increasing carrier concentration or Fermi level (E_F). For highly doped HEIWIP, the temperature dependence of Fermi level E_F is given by[115]

$$E_v - E_F = k_B T \left[ln\left(\frac{p}{N_v}\right) + 2^{-\frac{3}{2}}\left(\frac{p}{N_v}\right)\right], \tag{4.5}$$

where p is the doping density (cm^{-3}) level, the temperature dependent density of states (cm^{-3}) for GaAs in the valence band is $N_v = 2\left(\frac{m^* k_B T}{2\pi\hbar^2}\right)^{\frac{3}{2}}$ and the density-of-state effective mass of valence

band[115] is $m^* = \left(m_{lh}^{3/2} + m_{hh}^{3/2}\right)^{2/3}$. Hence, $N_v = 1.87233 \times 10^{15}\, T^{3/2}$. At zero electric field, the temperature dependence of activation energy or effective barrier height $\Delta(T)$ is given by $\Delta(T) = \Delta E_v(T = 0K) - E_F(T)$, where $\Delta E_v(T = 0\,K)$ is the barrier height at 0 K. For a temperature change from 60 K to 120 K, the change in Fermi level is $\Delta E_F(T) \cong 0.0062\, eV$,

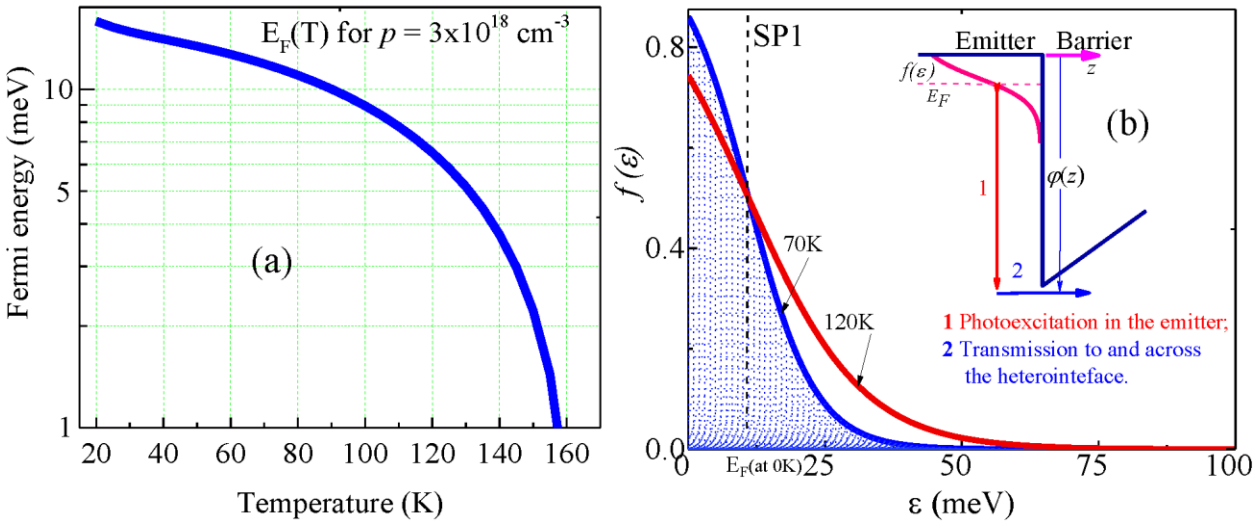

Figure 4.6 Temperature dependence of (a) Fermi level (b) Fermi distribution functions versus carriers' energy. The FD tail increases with temperature and extends up to ~ 100 meV for T = 120 K. The inset shows the photoexcitation in the emitter and the transition to and across the hetero-interface.

which is 4.2 %, 3.2 %, and 2.0 % of the barrier height calculated at intermediate temperature (80 K) for SP1, SP2, and SP3, respectively. This implies that the temperature dependence of Fermi level shown in Figure 4.6 (a), has little effect on these barrier heights. However, Figure 4.5 shows that, there are significant differences between the activation energy obtained from the Arrhenius plot and TDIPS fittings for structures with the least (0.28) Al mole fraction (SP1, LH1001, and LH1003) and highest doping level (LH1003; 6×10^{19} cm^{-3}). This disparity of the two results may be attributed to the non-linear temperature dependence of Δ over a wide range of

temperatures, and hence, is due to the temperature dependent band tailing effect shown in Figure 4.6 (b). The Fermi-Dirac occupation probability $f(\epsilon)$ of carriers with energy ϵ, is given by

$$f(\epsilon) = [1 + \exp(\epsilon - E_F/k_BT)]^{-1}.$$

The Fermi-Dirac distribution (FD) shows a very small tail above the Fermi level even at low temperatures (5 - 10 K). As the temperature increases, the occupation probability of carriers above the Fermi level at 0 K increases and the tail extends near to the edge of the small barrier heights such as SP1 (with Al mole fraction of 0.28) and LH1003 (highest doping levels (6×10^{19} cm^{-3})) as shown in Figure 4.6 (b). Hence, this tail has some profound effects on thermionic emission for temperature as high as 70 K and 120 K for SP1, LH1001, and LH1003 structures. As has been shown in the inset of Figure 4.6 (b), this significant change in the tail for temperature as high as 70 K, affect the activation energy of photoexcitation in the emitter.

4.3.4 Field emission

Thermally assisted field emission, also called Fowler-Nordheim (FN) tunneling, is the process whereby holes/electrons tunnel through a barrier in the presence of a high electric field. Field emission is a quantum mechanical tunneling process. The non-Arrhenius behavior of longer threshold wavelength detectors can also be explained by thermally assisted field emission or Fowler-Nordheim tunneling current. The current density *(J_{Tun})* induced by holes tunneling in the z- or growth direction through a barrier shown in Figure 4.2 is given by

$$J_{Tun} = \frac{qm^*k_BT}{2\pi^2\hbar^3}\int_0^\infty T(\epsilon_z, F)\, ln\left(1 + e^{(\epsilon_z - E_f)/k_BT}\right)d\epsilon_z, \quad (4.6)$$

where the probability T(ϵ_z, F) of holes that can penetrate through a “slowly" varying potential[115, 131, 132] barrier of height $\varphi(z)$ is given by the well-known Wentzel-Kramer-Brillouin (WKB) method as

$$T \cong exp\left(-2\int_{z_0}^{z_1}\sqrt{\frac{2m^*}{\hbar^2}(\varphi(z)-\epsilon_z)}dz\right) = exp(-B(\epsilon_z)). \quad (4.7)$$

This approach yields a value of T = 1 for energies above the maximum value of qV, but it does not include quantum mechanical reflection in these cases. This means that it overestimates the

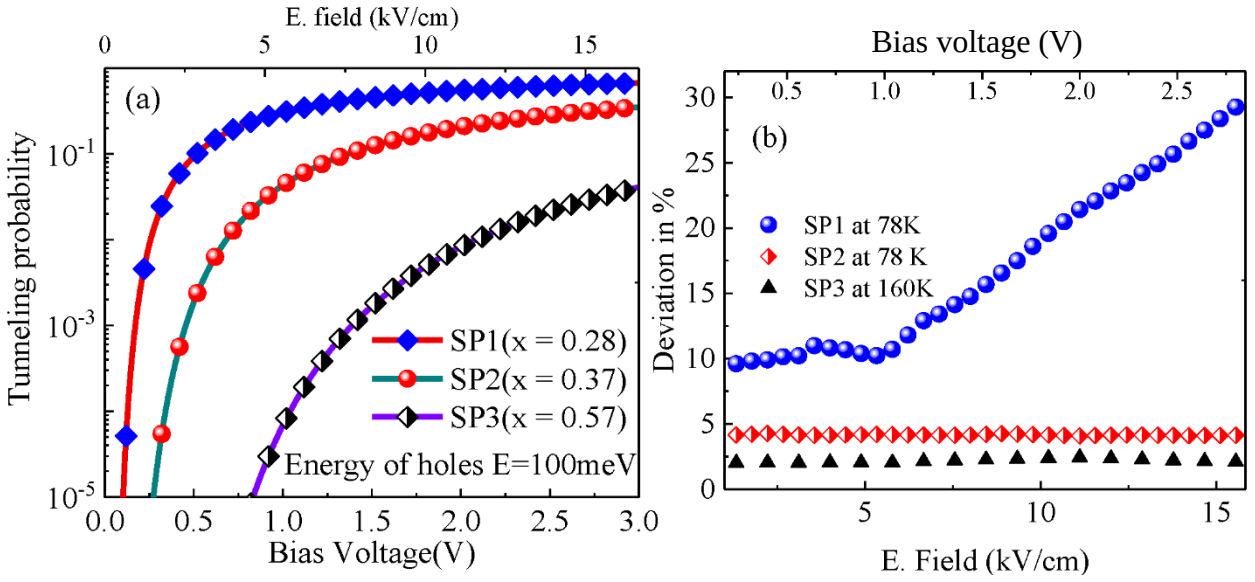

Figure 4.7 (a) The tunneling probability of holes with 100 meV energy as a function of bias voltage for three different barrier heights. (b) The deviation of activation energy as determined by the Arrhenius plot compared to that from TDIPS.

current for shallow barriers and cannot handle the case of a zero barrier at the interface. An alternate method of derivation of the transmission probability yields an expression with identical exponent but slightly different from equation 4.7.[133] This alternate expression is far more accurate near and above the top of the barrier.[134]

$$T(\epsilon, F)_{WKB\ type} \cong \frac{1}{1+exp(-B(\epsilon))} \quad (4.8)$$

In general, this expression is not often used because when multiplied by another function it is often un-integrable. However, with a series of reasonable approximations, it becomes a very

useful method. The tunneling current is proportional to transmission probability. The tunneling probability shown in Figure 4.7 (a) and (b), where the deviation between methods increases with bias voltage confirms that the FN tunneling current cannot be ignored for the lower barrier height of SP1 (x = 0.28). Similarly, Yang, et al[135] mentioned that tunneling currents in InAs/(GaIn)Sb superlattice photodiodes are important issues for photodetectors operating in the long-wavelength ($\gg$ 8 μm) range.[135-137]

The temperature range for the thermionic current to be dominant (or only thermionic) varies with bias voltage (electric field) and barrier height. One can roughly estimate the minimum average temperature for which thermionic current starts to be dominant. Figure 4.3 (b) shows the linear part of plots in Figure 4.3 (a), where the dark current is dominant or only due to thermionic emission. Then the Arrhenius plot can be used to extract the activation energy for the temperature range starting from this minimum average temperature (column two of Table 4.2) to the highest temperature within maximum current limit (~ 1 mA) of the measurements. Based on the experimental results shown in Figure 4.4 and Table 2.2, the percentage deviation of activation energy of the Arrhenius plot from the corresponding TDIPS fitting values at (or near) zero bias and at bias voltage of 1 V (5.4 kV/cm), except 0.1 V (0.54 kV/cm) for LH1003, is related to the threshold wavelength of the detectors. For SP1, SP2, and SP3, the activation energy increases with increasing Al mole fraction (x = 0.28, 0.37, and 0.57, respectively). However, for SP1, LH1001 and LH1003, the activation energy decreases with increasing doping levels (3×10^{18} cm^{-3}, 6×10^{18} cm^{-3}, 6×10^{19} cm^{-3}, respectively).

Table 4.2 The percentage deviation of Arrhenius Δ from the corresponding TDIPS Δ near zero bias and at bias voltage of 1 V (5.4 kV/cm), except 0.1 V (0.54 kV/cm) for LH1003. As the threshold wavelength increases from 4 μm to 12.9 μm, the deviation of activation energy determined by Arrhenius plot from TDIPS fitting values increases.

Sample	Minimum Average Temp (K) for Arrhenius	Temp. (K) for TDIPS Δ	λ_t (μm) at 1.0V (5.4kV/cm)	Near zero bias voltage			At 1.0V (5.4 kV/cm) except 0.54 kV/cm for LH1003.		
				Arrhenius Δ(eV), $\frac{\partial(\ln(R_o A))}{\partial(\frac{1}{k_B T})}$	TDIPS Δ(eV)	| Arrh-TDIPS | Δ	Arrhenius Δ(eV), $\frac{\partial(\ln(J/T^{1.5}))}{\partial(\frac{1}{k_B T})}$	TDIPS Δ(eV)	| Arrh-TDIPS | Δ
SP3	140	160	4.03±0.01	0.303±0.002	0.309	1.9%	0.309±0.003	0.307±0.001	0.3%
LH1004	120	78	4.48±0.02	0.280±0.003	0.288	2.8%	0.266±0.002	0.277±0.001	4.0%
SP2	120	78	6.53±0.03	0.188±0.002	0.196	4.0%	0.182±0.002	0.190±0.001	4.2%
SP1	70	78	9.32±0.21	0.139±0.003	0.150	7.3%	0.120±0.002	0.133±0.003	9.7%
LH1001	60	78	9.61±0.22	0.120±0.006	0.146	17.8%	0.110±0.003	0.129±0.003	15.4%
LH1003	40	46	12.92±0.40	0.084±0.005	0.141	40.4%	0.048±0.003	0.096±0.003	50.6%

As the threshold wavelength increases from 4 μm to 12.9 μm, the deviation of activation energy determined by the Arrhenius plot from the corresponding TDIPS fitting values increases; for example, from 0.3 % (at 160 K for SP1) to 50.6 % (at 46 K for LH1003). A summary of this results is shown in Table 4.3. For detectors with ~ 6.5 μm or shorter threshold wavelength, the Arrhenius analysis yields the values of activation energy within 5 % deviation from that of TDIPS fitting values. Even though the Arrhenius plot is valid in general at low field (near zero volts) over a certain temperature range, a significant deviation from TDIPS fitting values are observed due to the Fermi distribution tail (see Figure 4.6 (b)) that extends up to the edge of lowest band offset (0.157 eV) (detectors, SP1, LH1001 and LH1003) for the minimum average temperatures of thermionic current shown in the second column of Table 4.2. The Arrhenius plot used to extract the activation energy of detectors with threshold wavelength longer than ~ 9.3 μm, where the FN tunneling, and Fermi tailing effects cannot be ignored, such as in SP1,

LH1001, and LH1003, does not lead to precise values, nor does it represent any parameters of carriers' energy.

Table 4.3 Summary of results: The validity of activation energy extracted from TDIPS fitting and Arrhenius plot for different wavelength ranges. The accuracy of the Arrhenius plot is expressed in terms of deviation from the corresponding TDIPS fitting. The accuracy of TDIPS fitting depends on the accuracy of spectral response measurement.

λ_t (μm)	TDIPS	Arrhenius Plot
3 - ~ 5 (MIR)	Valid at any operating temperature	Deviates up to a maximum of ~ 5 % at temp. higher than ~120 K.
5 – ~ 9.3	Valid at any operating temperature	Deviates up to a maximum of ~ 10 % at temp higher than ~70 K and e. field F << 5.4kV/cm.
> 9.3	Valid at any operating temperature	Not valid irrespective of temperature and electric field.

4.4 Summary

GaAs/AlGaAs heterostructures with different barrier heights were evaluated. As the threshold wavelength of detector increases from 4 μm to 12.9 μm, the deviation of activation energy determined by the Arrhenius plot from the corresponding TDIPS fitting value increases. For detectors with ~ 6.5 μm or shorter threshold wavelength, the Arrhenius analysis yields the values of activation energy with less than 5 % deviation. However, for detectors with longer threshold wavelength (>> 9.3 μm), the Arrhenius plot used to extract activation energy leads to energy values with deviation higher than ~ 10 %. The higher percentage deviation (> 10 %) of activation energy determined by the Arrhenius plot from the corresponding TDIPS values results from the temperature dependent Fermi distribution tailing effect and Fowler–Nordheim tunneling current. Therefore, if a precise band offset characterization of a long threshold wavelength

detector is needed, it is necessary to avoid the Arrhenius method. In that case, TDIPS or another method, taking the temperature effects on the band offset into account needs to be considered. However, the Arrhenius plot method is simple and is a reasonable tool to characterize detectors with a shorter threshold wavelength ($\ll 9.3\ \mu m$).

5. EXPERIMENTAL SETUP AND ERROR ANALYSIS FOR MEASURED DATA

5.1 Electrical characterization

5.1.1 Current-Voltage-Temperature (I-V-T)

In this study, a fully automated *I-V-T* measurement setup was used, which consists of a Keithley 2400 Source Meter, Keithley 2701 switch system, Lake Shore 330 Auto tuning Temperature Controller and close cycle refrigerator as shown in Figure 5.1. The detectors in a

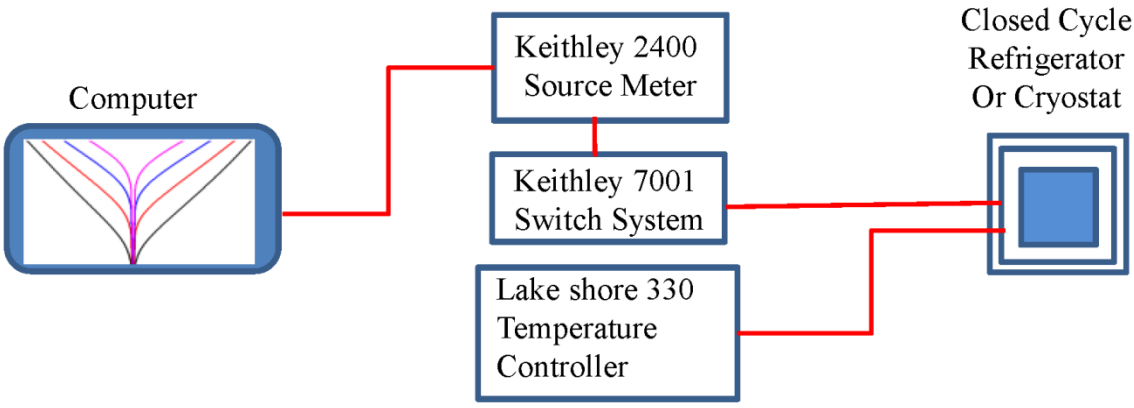

Figure 5.1 Block diagram of the experimental setup for *I-V-T* measurements. up to 10 mesas can be mounted in close cycle at a time and alternatively switched to the source meter automatically.

wafer were mounted on chip carriers with silver epoxy and individual detectors or mesas were wire bonded to separate leads of the carriers. This chip carrier was then mounted in a variable temperature cryostat (6.5 K-300 K). The *I-V-T* characteristics were then measured using Keithley 2400 Source Meter. Up to 10 mesas or individual detectors can be mounted and measured with one at a time with the help of automated switch system, Keithley 7001. The temperatures were controlled and varied from 10 K to 300 K using a Lake Shore 330 Auto tuning Temperature Controller with an accuracy of ± 0.01 K.

5.1.2 Noise measurement

To determine the dark current gain, photoconductive gain and the specific detectivity for the detector, the noise power spectral density measurements were performed, in addition to dark currents and responsivity of the detector. The noise spectral density of samples was measured with a dual channel Fast Fourier Transform (FFT) signal analyzer (HP SRS- SR785) and a low noise pre-amplifier, either low noise voltage amplifier SR560 or low noise current amplifier

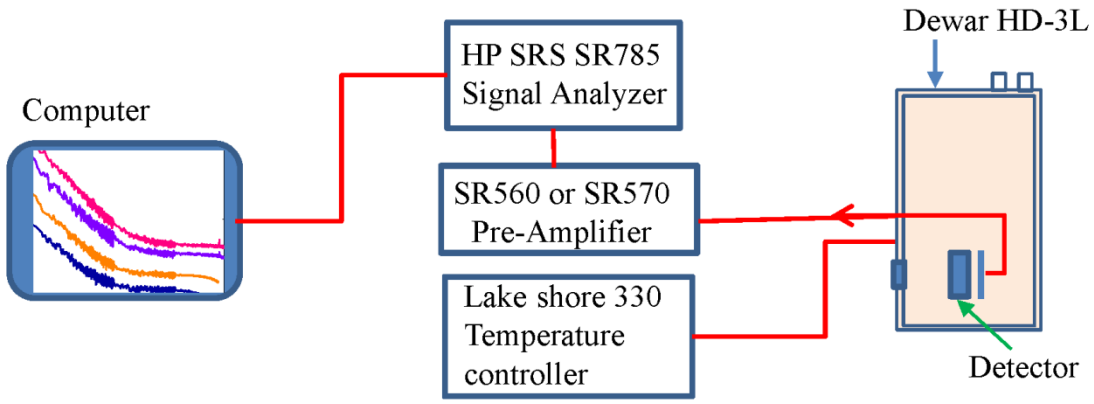

Figure 5.2 Block diagram for Noise measurements. The pre-amplifier represents SR 560 Low-noise voltage amplifier or SR 570 Low noise current amplifier.

SR570 as shown in Figure 5.2. The detector was mounted inside the Dewar and a thick copper plate was used as the radiation block in the optical window to provide the dark conditions for the measurements. The measurement techniques are briefly described as follows. Both SR570, a low-noise current amplifier and SR560, Low noise voltage amplifier were powered by a battery to ensure optimal noise performance and to minimize the 60 Hz pickup (which still appears, though to a smaller extent, in the noise spectrum because the HP SRS-SR785 spectrum analyzer was powered from the mains) and its harmonics from the mains. The gain and sensitivity settings of the SR560 Low-noise voltage amplifier and SR570 Low-noise current amplifier affected the frequency roll-off of the measurement setup due to the finite gain-bandwidth of the measurement

system. Any measured data corresponding to frequencies beyond the roll-off were inaccurate. Hence, it was necessary to select an appropriate sensitivity setting for the SR570 current pre-amplifier according to its nominal gain versus bandwidth performance. This was done to ensure that the frequencies of interest occur before the roll-off frequency. In this work, the sensitivity setting of the SR570 current amplifier was set at 1 μA/V, giving a frequency roll-off at about 2 kHz. The maximum frequency sweep range for the noise spectrum was set so as not to exceed 1 kHz. For low noise level (~ 10^{-26} A^2/Hz), the SR570 current pre-amplifier has relatively higher bandwidth that the corresponding SR560 voltage pre-amplifier while the voltage pre-amplifier is more stable and has higher precision for relatively higher noise levels. The SR560 voltage pre-amplifier was used with the voltage gain in the range of 100 to 1000 that provide amplification before the signal was fed into the HP SRS-SR785 dynamic signal analyzer. Details of experimental procedures are discussed in section 2.3 and then the power spectral density obtained in V^2/Hz was calibrated to voltage and current spectral density using equation (2.1) and (2.2) respectively.

5.2 Spectral Response Measurements and Calibration

The responsivity measurements of detectors were made using a Perkin Elmer System 2000 Fourier Transform Infrared Spectrometer (FTIR). The spectral measurement was carried out from 0.8 - ~ 300 μm with temperatures varying from 4 K to room temperature. A block diagram showing the spectral measurement setup is shown in the Figure 5.3.

In this setup, the detector under test was compared to a Si composite bolometer under the same conditions. The spectral response of the detector was measured under normal incidence configuration with a Perkin Elmer System 2000 Fourier Transform Infrared Spectrometer (FTIR). An electrically heated silicon carbide globar was used as IR source. Like the response

measurement of the detector, the spectrum of the globar IR source was measured using the Si composite bolometer of known sensitivity. The two spectra for the detector under test and the

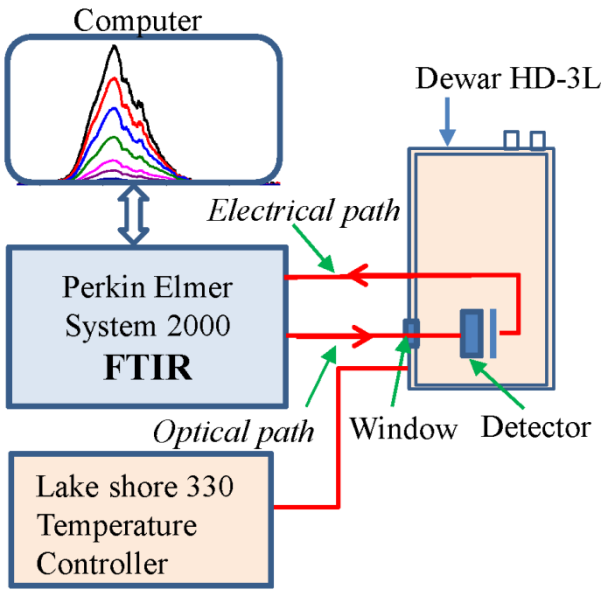

Figure 5.3 Block diagram of the experimental setup for IR spectral measurements using a FTIR spectrometer. Optical and electrical paths are denoted by arrows.

globar IR source were obtained concurrently with the same combination of optical windows, beam splitters, and filters, providing identical optical path. The detector spectrum (I_d) was then divided by the IR source spectrum measured by bolometer (I_b) and multiplied by the bolometer sensitivity (S_0) to obtain the voltage responsivity of the detector:

$$R\left(\frac{V}{W}\right) = \mathcal{G}\frac{I_d S_o}{I_b} \tag{5.1}$$

Here $\mathcal{G}$ is a geometrical factor which corrects for differences in the radiation-incident area of the detector and the bolometer. To obtain the current responsivity, the voltage responsivity was divided by the effective resistance of the detector and load resistance. As the detector and the load resistor (see Figure 2.2) act as a voltage divider, the effective resistance $\mathcal{R}_e$ is the parallel

combination of the load resistance $\mathcal{R}_l$ and the detector dynamic resistance $\mathcal{R}_d = dV/dI$, yielding $\mathcal{R}_e = \mathcal{R}_l\mathcal{R}_d/(\mathcal{R}_l + \mathcal{R}_d)$. The final current responsivity is given by

$$R\left(\frac{A}{W}\right) = \mathcal{G}\frac{I_d S_o}{I_b}.\frac{(\mathcal{R}_l+\mathcal{R}_d)}{\mathcal{R}_l\mathcal{R}_d}. \tag{5.2}$$

The specific detectivity (D^*) of the detectors at different temperatures and applied bias voltage was obtained from the measured peak (or highest value of) responsivity R_p and noise power spectral density, S_i. The value of D^* was calculated from

$$D^*(cm\sqrt{Hz}/W) = R_p A^{1/2} / S_i^{1/2}, \tag{5.3}$$

where A is the illuminated area of the detector.

5.3 Error analysis of experimental data

In this work, electronic noise, I-V-T, and responsivity of detectors were experimentally measured. It is a known fact that performing noise measurements is not an easy task. Special precautions must be taken, and accurate measurement methods must be developed and observed. Dark noise spectral density measurements were performed using the SRS SR560 low noise voltage preamplifier with the gain value from 100 to 1000 and using the SR785 in the power spectrum (PS) mode. To get the most accurate data, from 5 to 10 data sets (with each about 100 scans or average of 100 measurements) were collected. After the data are calibrated based on procedures mentioned in section 2.3, the error bar for noise spectral density, S(f) is calculated as the standard deviations $\delta S(f)$, of the data as shown in Figure 5.4.

$$\delta S(f) = \sqrt{\frac{1}{N-1}\sum_{i}^{N}(S_i - \bar{S})^2}$$

Hence, the measured spectral density is given by $S(f) = \overline{S(f)} \pm \delta S(f)$.

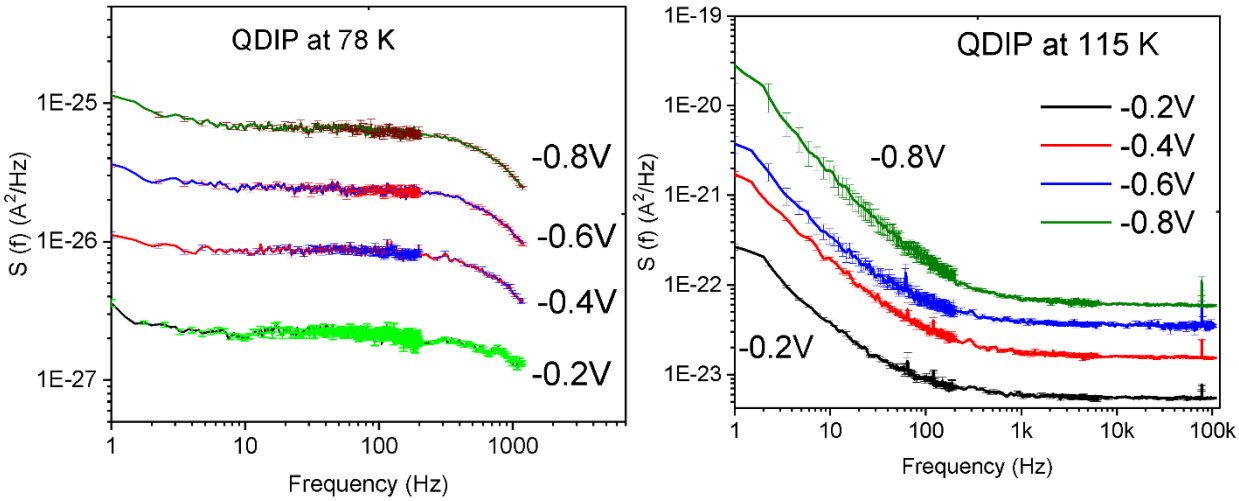

Figure 5.4 Shows the measured dark noise spectral density of QDIP at 78K and 115 K. These measurements are the average of 10x100 scans. Such high number data sets minimize the error bars as shown. The value of noise spectral density used to calculate the gain lies in the linear part of measurements.

The sensitivity and gain settings of the SR570 and 560 current and voltage amplifiers affect the frequency roll-off of the measurement setup due to the finite gain-bandwidth product of the measurement system. Any measurement data that correspond to frequencies beyond the roll off are inaccurate. Hence, it is necessary to select an appropriate sensitivity setting for the SR570 current amplifier according to its nominal gain versus bandwidth performance. This is to ensure that the frequencies of interest occur before the roll off frequency as shown in Figure 5.4.

Then the corresponding average gain with propagated errors can be calculated using equation

$$\bar{g} = \left(\frac{\overline{S(f)}}{4e\overline{I_d}} + \frac{1}{2N}\right)\left[1 \pm \left(\frac{\delta s(f)}{S(f)} + \frac{\delta I_d}{I_d}\right)\right],$$

where N (10 for QDIP and DWELL) is the number of active layer, $\delta S(f)$ and δI_d are the standard deviation of noise spectral density and dark current respectively. Similarly, the

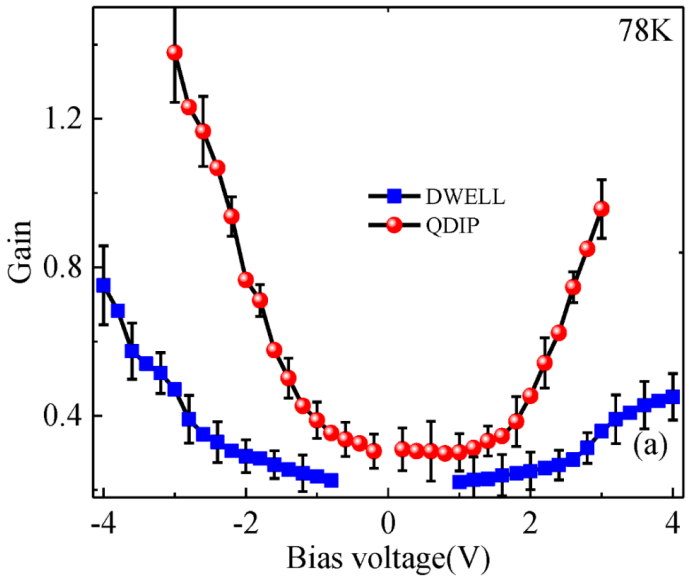

Figure 5.5 Comparison of gain for QDIP and DWELL with the error bars.

uncertainty of capture probability $p_c = \frac{1}{N\,g}$ is calculated as

$$p_c = \bar{p_c}\left(1 \pm \frac{\delta g}{g}\right).$$

For QDIP at 2 V, $S(f) = 1.3 \times 10^{-24} \pm 6.75 \times 10^{-26}\, A^2/Hz$, and $I_d = 4.97 \times 10^{-6} \pm 4.89 \times 10^{-7} A$, the corresponding gain and capture probability were determined to be 0.454±0.079 and 0.198± 0.017 (see Figure 5.5).

Unlike the noise measurements, our standard I-V-T and spectral response measurements are more stable and accurate. And hence, several repeated measurements will not lead to appreciable deviation from the mean as shown in Figure 5.6.

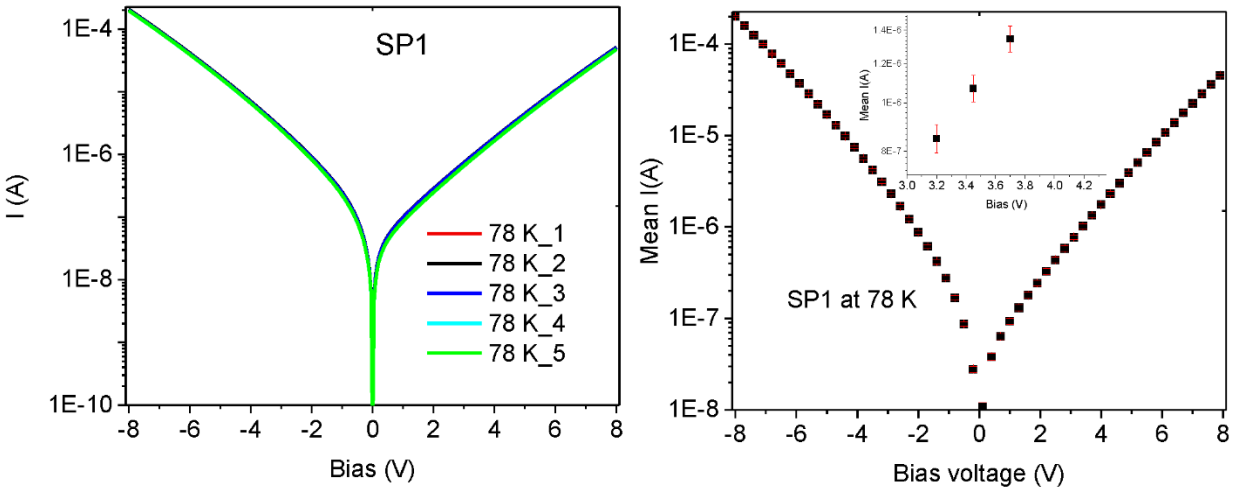

Figure 5.7 5 × 10 scans of I-V measurement of SP1 at 78 K. Almost all the measurements are overlapping. The second figure shows the mean I (A) value with error bars. Since the error bar is very small in this scale, it is very difficult to see the error bar and that is why the inset show the zoomed-out scale of the mean I (A). Hence most of dark current measurements are not including the error bars.

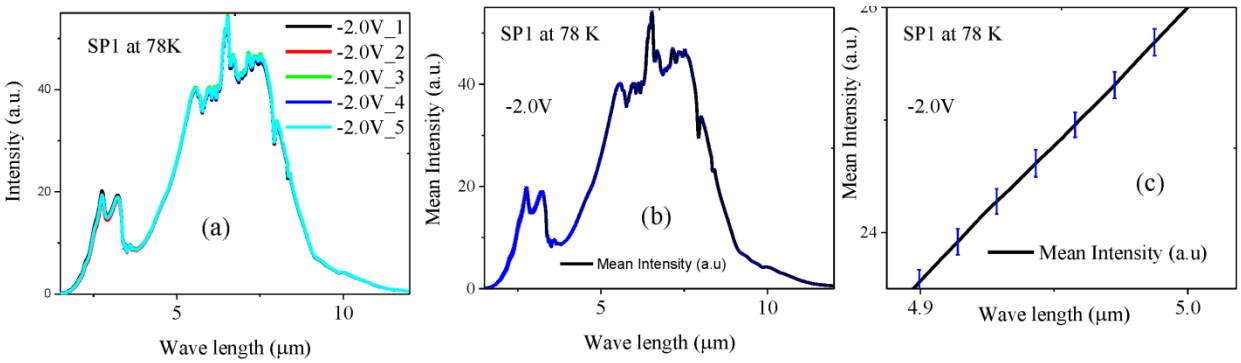

Figure 5.6 (a) Five raw data set for response measurements of 50 scans for SP1 at 78 K and - 2.0 V. (b) The mean value with error bar for the raw data in (a) are shown. (c) For the wave length from 4.9 to 5 μm, the mean intensity in (b) is zoomed out to show the error bars.

Similarly, the response measurements were made for SP1 at 78 K and - 2.0 V. Five raw data sets of 50 scans each were measured as shown in Figure 5.7 (a). Within the wavelength shown in Figure 5.7, the number of measurements for a given experimental setup and optimization was not yield the significant fluctuation or error bar in FTIR measurement. The mean value with the error bar is shown in Figure 5.7 (b). In the scale shown in Figure 5.7 (b), the error bar is too small to see and Figure 3.7 (b) zoomed out as shown in Figure 5.7 (c).

6. CONCLUSIONS AND FUTURE WORK

The *p*-type InAs/GaAs, MIR (λ_p ~ 5.2 μm) detector at 78 K, demonstrated the promise of using hole transitions to develop QDIP and DWELL, with a QE of 17 % and 9 % respectively.[31] Two response bands at 1.5 – 3 and 3 – 10 μm were confirmed as being due to hole transitions from the HH to SO level and from the HH to HH level,[30] respectively. Furthermore, a *p*-type THz (broad response with a peak response at ~ 9.2 THz) detector based on intersubband transitions in InAs/InGaAs QDIP/DWELL structures was demonstrated.[25] MIR peaks are associated with transitions from ground state of QD to continuum states or near-barrier QW state, whereas the THz responses originate due to higher temperatures (~ 100 K - 130 K).[25] Therefore, detector response was extended to THz range up to ~ 4.28 THz (~ 70 μm) at a highest operating temperature of 130 K.[25] Further optimization, such as doping level, width of the well, barrier thickness, using double barrier tunneling heterostructure or a thin dark current blocking layer to reduce dark current, could enhance and extend the response of terahertz detection at temperature higher than 130 K and improve detectivity.

In *p*-type GaAs/AlGaAs heterostructures with both flat and graded barriers at low temperature and low bias, the frequency independent G-R shot noise prevails whilst as temperature rises, both 1/*f* and Johnson noise add to the shot noise.[66] Comparisons of dark and photocurrent noise gains between the flat and graded barrier samples confirm that the escape probability of carriers is enhanced by grading the barrier, because the graded barrier reduces the recombination mechanism owing to the higher momentum of carriers.[66] Despite only a very small change in noise density with increasing optimized emitter thickness, the specific detectivity (or responsivity) does increase significantly owing to higher absorption efficiency. Thus, optimizing the emitter thickness of graded barrier detectors to enhance the absorption efficiency, and increase the escape probability and lower dark current, enhances the specific detectivity of detectors.

The noise power spectral densities of DWELL and QDIP, at lower temperature (below ~ 100 K) and low bias, the noise current of these detectors is dominated by generation-recombination (G-R) noise. The capture probability of DWELL is found to be more than two times higher than the corresponding QDIP.[43] Based on the analysis, structural parameters such as the number of active layers, the surface density of QDs, and the carrier capture or relaxation rate, type of material and electric field are some of the optimization parameters identified to improve the photoconductive gain of detectors.

Different barrier heights within the GaAs/AlGaAs heterostructures were evaluated. As the threshold wavelength of detector increases from 4 μm to 12.9 μm, the deviation of activation energy determined by the Arrhenius plot from the corresponding TDIPS fitting value increases. For detectors with ~ 6.5 μm or shorter threshold wavelength, the Arrhenius analysis yields the correct values of activation energy with less than 5 % deviation. However, for detectors with

longer threshold wavelength (>> 9.3 μm), the Arrhenius plot used to extract activation energy leads to energy values with deviations higher than ~ 10 %. The higher percentage deviation (> 10 %) of activation energy determined by the Arrhenius plot from the corresponding TDIPS values is attributed to the temperature dependent Fermi distribution tailing effect and the Fowler–Nordheim tunneling current. Therefore, if a precise band offset characterization of long threshold wavelength detector is needed, it is inevitable to avoid the Arrhenius method. In that case, TDIPS or another method, taking the temperature effect in to account needs to be considered. However, the Arrhenius method is simple and a reasonable tool to characterize detectors with shorter threshold wavelengths ($\ll 9.3\ \mu m$).

Generally, these studies mainly follow four papers published (one under review), in different journals. The discussions in Chapter 1 follow the Appl. Phys. Lett. paper by Wolde et al[25] and partly Lao, et al.[30, 31] The second chapter, that discusses the noise in GaAs/AlGaAs flat and graded barrier heterostructures follows the paper published in Infrared Physics &Technology by Wolde, et al.[66] The main discussion of chapter 3, is investigation of carrier photoconductive gain and capture probability which follows the paper published in J. of Appl. Phys., by Wolde, et al. [43] Chapter 4, which entails the advantages and disadvantages of the two important tools Arrhenius plot and TDIPS for characterizing photodetectors is submitted for publication and is under review.

In future, to achieve the desired wavelengths of detection and optimized performance, InAs QDs will be designed to grow directly on an AlAs layer of a GaAs/AlAs super lattice, which offers additional miniband confinement. Another structural design that improves detector performance employs an optimized Al(Ga)As dark current blocking layer with little effect on photocurrent (responsivity). The additional miniband confinement will enhances 3 – 5 μm

responses while the low dark current due to Al(Ga)As will enhance detectivity and elevate operating temperatures.

The key advantage of nanostructures is the suppression of the phonon scattering mechanism which results in longer carrier lifetimes. Therefore, the long effective carrier lifetime in QDIP and DWELL, ~100 ps (compared to ~1 ps for bulk GaAs [138]), confirmed by experiments [139, 140] can be utilized in the new design of the detectors with QWs and DWELLs (or QDs) based injector and absorber, respectively. Hence, nanostructures will increase the hot carrier lifetime (in both injector and absorber), enhancing hot-cold carrier energy transfer and extended wavelength photoresponse that leads to an improved performance and elevated operating temperature.

REFERENCES

1. A. Y. Pawar, D. D. Sonawane, K. B. Erande and D. V. Derle, Drug Invention Today **5**, 157 (2013).
2. I. M. Baker and C. D. Maxey, J. of Electronic Materials **30**, 682 (2001).
3. J. B. Varesi, R. E. Bornfreund, A. C. Childs, W. A. Radford, K. D. Maranowski, J. M. Peterson, S. M. Johnson, L. M. Giegerich, T. J. de Lyon and J. E. Jensen, J. of Electronic Materials **30**, 566 (2001).
4. A. Rogalski, *Infrared Detectors, Second Edition*. (CRC Press, 2010).
5. W. U. Huynh, J. J. Dittmer and A. P. Alivisatos, Science **295**, 2425 (2002).
6. V. I. Klimov, A. A. Mikhailovsky, S. Xu, A. Malko, J. A. Hollingsworth, C. A. Leatherdale, H.-J. Eisler and M. G. Bawendi, Science **290**, 314 (2000).
7. P. V. V. Jayaweera, P. K. D. D. P. Pitigala, J. F. Shao, K. Tennakone, A. G. U. Perera, P. M. Jayaweera and J. Baltrusaitis, IEEE Transactions on Electron Devices **57**, 2756 (2010).
8. A. V. Barve, S. Sengupta, J. O. Kim, Y. D. Sharma, S. Adhikary, T. J. Rotter, S. J. Lee, Y. H. Kim and S. Krishna, Appl. Phys. Lett. **99**, 191110 (2011).
9. D. Pachinger, H. Groiss, H. Lichtenberger, J. Stangl, G. Hesser and F. Schäffler, Appl. Phys. Lett. **91**, 233106 (2007).
10. S. Krishna, S. Raghavan, G. von Winckel, A. Stintz, G. Ariyawansa, S. G. Matsik and A. G. U. Perera, Appl. Phys. Lett. **83**, 2745 (2003).
11. P. Bhattacharya, X. Su, S. Chakrabarti, G. Ariyawansa and A. Perera, Appl. Phys. Lett. **86**, 191106 (2005).
12. U. Bockelmann and G. Bastard, Phys. Rev. B **42**, 8947 (1990).

13. G. Ariyawansa, A. G. U. Perera, X. H. Su, S. Chakrabarti and P. Bhattacharya, Inf. Phys. & Technology **50**, 156 (2007).

14. E. Hanamura, Phys. Rev. B **37**, 1273 (1988).

15. D. Pan, E. Towe and S. Kennerly, Appl. Phys. Lett. **73**, 1937 (1998).

16. O. Qasaimeh, K. Kamath, P. Bhattacharya and J. Phillips, Appl. Phys. Lett. **72**, 1275 (1998).

17. H. C. Liu, M. Gao, J. McCaffrey, Z. R. Wasilewski and S. Fafard, Appl. Phys. Lett. **78**, 79 (2001).

18. L. Jiang, S. S. Li, N.-T. Yeh, J.-I. Chyi, C. E. Ross and K. S. Jones, Appl. Phys. Lett. **82**, 1986 (2003).

19. S. Chakrabarti, A. D. Stiff-Roberts, X. Su, P. Bhattacharya, G. Ariyawansa and A. G. U. Perera, J. Phys. D: Appl. Phys. **38**, 2135 (2005).

20. H. Lim, S. Tsao, W. Zhang and M. Razeghi, Appl. Phys. Lett. **90**, - (2007).

21. A. L. Betz, R. T. Boreiko, B. S. Williams, S. Kumar, Q. Hu and J. L. Reno, Opt. Lett. **30**, 1837 (2005).

22. M. B. M. Rinzan, A. G. U. Perera, S. G. Matsik, H. C. Liu, Z. R. Wasilewski and M. Buchanan, Appl. Phys. Lett. **86**, 071112 (2005).

23. G. Huang, W. Guo, P. Bhattacharya, G. Ariyawansa and A. G. U. Perera, Appl. Phys. Lett. **94**, 101115 (2009).

24. G. Ariyawansa, A. G. U. Perera, G. S. Raghavan, G. von Winckel, A. Stintz and S. Krishna, Photonics Technology Lett., IEEE **17**, 1064 (2005).

25. S. Wolde, Y.-F. Lao, A. G. U. Perera, Y. H. Zhang, T. M. Wang, J. O. Kim, T. Schuler-Sandy, Z.-B. Tian and S. Krishna, Appl. Phys. Lett. **105**, 151107 (2014).

26. P. T. Greenland, Contemporary Physics **54**, 263 (2013).

27. B. F. Levine, J. Appl. Phys. **74**, R1-R81 (1993).

28. J. R. Hoff, M. Razeghi and G. J. Brown, Phys. Rev. B **54**, 10773 (1996).

29. X. H. Su, J. Yang, P. Bhattacharya, G. Ariyawansa and A. G. U. Perera, Appl. Phys. Lett. **89**, 031117 (2006).

30. Y.-F. Lao, S. Wolde, A. G. U. Perera, Y. H. Zhang, T. M. Wang, H. C. Liu, J. O. Kim, T. Schuler-Sandy, Z.-B. Tian and S. S. Krishna, Appl. Phys. Lett. **103**, 241115 (2013).

31. Y.-F. Lao, S. Wolde, A. G. U. Perera, Y. H. Zhang, T. M. Wang, J. O. Kim, T. Schuler-Sandy, Z.-B. Tian and S. S. Krishna, Appl. Phys. Lett. **104**, 171113 (2014).

32. Y. Tu and J. Tersoff, Phys. Rev. Lett. **93**, 216101 (2004).

33. B. J. Spencer, P. W. Voorhees and S. H. Davis, Phys. Rev. Lett. **67**, 3696 (1991).

34. J. A. Venables, G. D. T. Spiller and M. Hanbucken, Reports on Progress in Physics **47**, 399 (1984).

35. V. M. Ustinov, N. A. Maleev, A. E. Zhukov, A. R. Kovsh, A. Y. Egorov, A. V. Lunev, B. V. Volovik, I. L. Krestnikov, Y. G. Musikhin, N. A. Bert, P. S. Kop'ev, Z. I. Alferov, N. N. Ledentsov and D. Bimberg, Appl. Phys. Lett. **74**, 2815 (1999).

36. X. Lu, in *Handbook of Nanophysics* (CRC Press, 2010), pp. 1-16.

37. Z. Y. Xu, Z. D. Lu, X. P. Yang, Z. L. Yuan, B. Z. Zheng, J. Z. Xu, W. K. Ge, Y. Wang, J. Wang and L. L. Chang, Phys. Rev. B **54**, 11528 (1996).

38. Y.-Y. Hu, Dissertation, International Max Plank Research Schools, Germany, 2013.

39. K. Sanjay, J. of Phys. D: Appl. Physics **38**, 2142 (2005).

40. H. Jiang and J. Singh, Phys. Rev. B **56**, 4696 (1997).

41. S. L. Chuang, *Physics of Optoelectronics devices*. (Wiley, New York, 1995).

42. W. Sheng and J.-P. Leburton, Appl. Phys. Lett. **80**, 2755 (2002).

43. S. Wolde, Y.-F. Lao, A. G. U. Perera, Y. H. Zhang, T. M. Wang, J. O. Kim, T. Schuler-Sandy, Z.-B. Tian and S. Krishna, J. of Appl. Phys. **121**, 244501 (2017).

44. S. Kabi and A. G. U. Perera, J. of Appl. Phys. **117**, 124303 (2015).

45. A. I. Yakimov, V. V. Kirienko, V. A. Armbrister, A. A. Bloshkin and A. V. Dvurechenskii, Appl. Phys. Lett. **107**, 213502 (2015).

46. M. A. Cusack, P. R. Briddon and M. Jaros, Phys. Rev. B **54**, R2300-R2303 (1996).

47. A. V. Barve, T. Rotter, Y. Sharma, S. J. Lee, S. K. Noh and S. Krishna, Appl. Phys. Lett. **97**, 061105 (2010).

48. A. Schliwa, M. Winkelnkemper and D. Bimberg, Phys. Rev. B **76**, 205324 (2007).

49. Y.-F. Lao, S. Wolde, A. G. U. Unil Perera, Y. H. Zhang, T. M. Wang, H. C. Liu, J. O. Kim, T. Schuler-Sandy, Z.-B. Tian and S. S. Krishna, Appl. Phys. Lett. **103**, 241115 (2013).

50. B. Kochman, A. D. Stiff-Roberts, S. Chakrabarti, J. D. Phillips, S. Krishna, J. Singh and P. Bhattacharya, Quantum Electronics, IEEE J. of **39**, 459 (2003).

51. A. G. U. Perera, W. Z. Shen, S. G. Matsik, H. C. Liu, M. Buchanan and W. J. Schaff, Appl. Phys. Lett. **72**, 1596 (1998).

52. M. R. Matthews, R. J. Steed, M. D. Frogley, C. C. Phillips, R. S. Attaluri and S. Krishna, Appl. Phys. Lett. **90**, 103519 (2007).

53. S. D. Gunapala, S. V. Bandara, C. J. Hill, D. Z. Ting, J. K. Liu, S. B. Rafol, E. R. Blazejewski, J. M. Mumolo, S. A. Keo, S. Krishna, Y. C. Chang and C. A. Shott, Infr.Phys. & Technology **50**, 149 (2007).

54. G. Huang, J. Yang, P. Bhattacharya, G. Ariyawansa and A. Perera, Appl. Phys. Lett. **92**, 011117 (2008).

55. M. Ershov and A. N. Korotkov, Appl. Phys. Lett. **71**, 1667 (1997).

56. R. A. Rupani, S. Ghosh, X. Su and P. Bhattacharya, Microelectron. J. **39**, 307 (2008).

57. A. G. U. Perera, V. G. Silvestrov, S. G. Matsik, H. C. Liu, M. Buchanan, Z. R. Wasilewski and M. Ershov, J. of Appl. Phys. **83**, 991 (1998).

58. V. Palenskis, J. Matukas, S. Pralgauskaitė, D. Seliuta, I. Kašalynas, L. Subačius, G. Valušis, S. P. Khanna and E. H. Linfield, J. of Appl. Phys. **113**, 083707 (2013).

59. F. N. Hooge, Phys. Lett. A **29**, 139 (1969).

60. F. N. Hooge and L. K. J. Vandamme, Phys. Lett. A **66**, 315 (1978).

61. H. Mikoshiba, IEEE Trans. on Electron Dev. **29**, 965 (1982).

62. A. Van Der Ziel, in *Advances in Electronics and Electron Physics*, edited by L. Marton and C. Marton (Academic Press, 1979), Vol. 49, pp. 225-297.

63. A. L. McWhorter, in *Semiconductor surface physics* (University of Pennsylvania Press 1957), pp. 207.

64. S. Kalem and G. E. Stillman, Jpn J. of Appl. Phys. **33**, 6086 (1994).

65. J. Szatkowski, E. Płaczek-Popko, K. Sierański and O. P. Hansen, J. of Appl. Phys. **86**, 1433 (1999).

66. S. Wolde, Y. F. Lao, P. K. D. D. P. Pitigala, A. G. U. Perera, L. H. Li, S. P. Khanna and E. H. Linfield, Infr. Physics & Technology **78**, 99 (2016).

67. J. Szatkowski, K. Sierański, A. Hajdusianek and E. Płaczek-Popko, Physica B: Condensed Matter **340**, 345 (2003).

68. C. Kayis, J. H. Leach, C. Y. Zhu, W. Mu, X. Li, U. Ozgur, H. Morkoc, X. Yang, V. Misra and P. H. Handel, Electron Dev. Lett. IEEE **31**, 1041 (2010).

69. A. G. U. Perera, S. G. Matsik, P. V. V. Jayaweera, K. Tennakone, H. C. Liu, M. Buchanan, G. Von Winckel, A. Stintz and S. Krishna, Appl. Phys. Lett. **89**, 131118 (2006).

70. P. K. D. D. P. Pitigala, Y. F. Lao, A. G. U. Perera, L. H. Li, E. H. Linfield and H. C. Liu, J. of Appl. Phys. **115**, 063105 (2014).

71. F. Pascal, S. Jarrix, C. Delseny, G. Lecoy and T. Kleinpenning, J. of Appl. Phys. **79**, 3046 (1996).

72. F. N. Hooge, T. G. M. Kleinpenning and L. K. J. Vandamme, Rep. on Prog. in Phys. **44**, 479 (1981).

73. Y. Paltiel, N. Snapi, A. Zussman and G. Jung, Appl. Phys. Lett. **87**, 231103. (2005).

74. A. Van Der Ziel, *Noise in Solid State Devices and Circuits*. (Wiley, 1986).

75. R. H. Mari, M. Shafi, M. Aziz, A. Khatab, D. Taylor and M. Henini, Nanoscale Research Lett. **6**, 180 (2011).

76. P. Krispin, S. G. Spruytte, J. S. Harris and K. H. Ploog, J. of Appl. Phys. **89**, 6294 (2001).

77. H. C. Liu, Appl. Phys. Lett. **61**, 2703 (1992).

78. M. Ershov and H. C. Liu, J. of Appl. Phys. **86**, 6580 (1999).

79. D. G. Esaev, M. B. M. Rinzan, S. G. Matsik and A. G. U. Perera, J. of Appl. Phys. **96**, 4588 (2004).

80. S. G. Matsik, P. V. V. Jayaweera, A. G. U. Perera, K. K. Choi and P. Wijewarnasuriya, J. of Appl. Phys. **106**, 064503 (2009).

81. G. Huang, J. Yang, P. Bhattacharya, G. Ariyawansa and A. G. U. Perera, Appl. Phys. Lett. **92**, 011117 (2008).

82. S. Adhikary, Y. Aytac, S. Meesala, S. Wolde, A. G. U. Perera and S. Chakrabarti, Appl. Phys. Lett. **101**, 261114 (2012).

83. V. Ryzhii, Semiconductor Sci. and Technology **11**, 759 (1996).

84. A. Stiff-Roberts, S. Krishna, P. Bhattacharya and S. Kennerly, J. of Vac. Sci. & Techn. B **20**, 1185 (2002).

85. A. Marent, T. Nowozin, J. Gelze, F. Luckert and D. Bimberg, Appl. Phys. Lett. **95**, 242114 (2009).

86. D. Pan, E. Towe and S. Kennerly, Appl. Phys. Lett. **75**, 2719 (1999).

87. A. D. Stiff, S. Krishna, P. Bhattacharya and S. Kennerly, Appl. Phys. Lett. **79**, 421 (2001).

88. S. Raghavan, P. Rotella, A. Stintz, B. Fuchs, S. Krishna, C. Morath, D. A. Cardimona and S. W. Kennerly, Appl. Phys. Lett. **81**, 1369 (2002).

89. Z. Ye, J. C. Campbell, Z. Chen, E.-T. Kim and A. Madhukar, Appl. Phys. Lett. **83**, 1234 (2003).

90. B. F. Levine, J. of Appl. Phys. **74**, R1-R81 (1993).

91. Y. F. Lao, P. K. D. D. P. Pitigala, A. G. U. Perera, H. C. Liu, M. Buchanan, Z. R. Wasilewski, K. K. Choi and P. Wijewarnasuriya, Appl. Phys. Lett. **97**, 091104 (2010).

92. H. C. Liu, Optoelectronics Review **11(1)**, 1-6 (2003).

93. V. Mitin, Phys. Rev. B **31**, 2584 (1985).

94. H. Liu and J. Zhang, Optics & Laser Technology **44**, 1536 (2012).

95. L. Lin, H. L. Zhen, N. Li, W. Lu, Q. C. Weng, D. Y. Xiong and F. Q. Liu, Appl. Phys. Lett. **97**, 193511 (2010).

96. X. Su, S. Chakrabarti, P. Bhattacharya, G. Ariyawansa and A. G. U. Perera, IEEE J. of Quant. Elect. **41**, 974 (2005).

97. M. Sotoodeh, A. Khalid and A. Rezazadeh, J. of appl. Phys. **87**, 2890 (2000).

98. R. Quay, C. Moglestue, V. Palankovski and S. Selberherr, Mat. Sci. in Semiconductor Processing **3**, 149 (2000).

99. A. Delga, L. Doyennette, M. Carras, V. Trinité and P. Bois, Appl. Phys. Lett. **102**, 163507 (2013).

100. W. A. Beck, Appl. Phys. Lett. **63**, 3589 (1993).

101. L. Jiang, S. S. Li, N.-T. Yeh, J.-I. Chyi, C. E. Ross and K. S. Jones, Appl. Phys. Lett. **82** (12), 1986-1988 (2003).

102. K. Pierz, A. Miglo, P. Hinze, F. J. Ahlers, G. Ade, I. Hapke-Wurst, U. Zeitler and R. J. Haug, physica status solidi (b) **224**, 119 (2001).

103. S. Y. Wang, S. D. Lin, H. W. Wu and C. P. Lee, Appl. Phys. Lett. **78**, 1023 (2001).

104. H. Benisty, C. M. Sotomayor-Torrès and C. Weisbuch, Phys. Rev. B **44**, 10945 (1991).

105. J. Urayama, T. B. Norris, J. Singh and P. Bhattacharya, Phys. Rev. Lett. **86**, 4930 (2001).

106. H. Liu and J. Zhang, Appl. Opt. **51**, 2767 (2012).

107. A. Mahmoodi, H. D. Jahromi and M. H. Sheikhi, IEEE Sensors J. **15**, 5504 (2015).

108. A. Stintz, G. Liu, A. Gray, R. Spillers, S. Delgado and K. Malloy, J. Vac. Sci. & Technol. B **18**, 1496 (2000).

109. Z. Ye, J. C. Campbell, Z. Chen, E.-T. Kim and A. Madhukar, J. Appl. Phys. **92**, 7462 (2002).

110. H. Schneider, *Quantum well infrared photodetectors*. (Springer, Berlin,, 2007).

111. A. G. U. Perera and W. Shen, Opto-electronics rev. **7** (3), 153 (1999).

112. Y.-F. Lao and A. G. U. Perera, Phys. Rev. B **86**, 195315 (2012).

113. Y. P. Song, R. L. Van Meirhaeghe, W. H. Laflère and F. Cardon, Solid State Elect. **29**, 633 (1986).

114. R. Kumar and S. Chand, Solid State Sciences **58**, 115 (2016).

115. S. M. Sze and K. K. Ng, *Physics of Semiconductor Devices*. (Wiley, 2006).

116. K. J. Malloy and J. A. V. Vechten, Appl. Phys. Lett. **54**, 937 (1989).

117. C. R. Becker, V. Latussek, A. Pfeuffer-Jeschke, G. Landwehr and L. W. Molenkamp, Phys. Rev. B **62**, 10353 (2000).

118. J. S. Helman and F. Sánchez-Sinencio, Phys. Rev. B **7**, 3702 (1973).

119. R. Yan, Q. Zhang, W. Li, I. Calizo, T. Shen, C. A. Richter, A. R. Hight-Walker, X. Liang, A. Seabaugh, D. Jena, H. G. Xing, D. J. Gundlach and N. V. Nguyen, Appl. Phys. Lett. **101**, 022105 (2012).

120. Y. Hikita, M. Kawamura, C. Bell and H. Y. Hwang, Appl. Phys. Lett. **98**, 192103 (2011).

121. Y.-F. Lao, P. K. D. D. P. Pitigala, A. G. U. Perera, E. Plis, S. S. Krishna and P. S. Wijewarnasuriya, Appl. Phys. Lett. **103**, 181110 (2013).

122. Y. F. Lao and A. G. U. Perera, Advances in OptoElectronics **2016**, 18 (2016).

123. Y.-F. Lao, A. G. U. Perera and P. S. Wijewarnasuriya, Appl. Phys. Lett. **104**, 131106 (2014).

124. A. G. U. Perera, Y. F. Lao, P. S. Wijewarnasuriya and S. S. Krishna, J. of Electronic Materials **45**, 4626 (2016).

125. Y.-F. Lao, A. G. U. Perera, Y. H. Zhang and T. M. Wang, Appl. Phys. Lett. **105**, 171603 (2014).

126. A. G. U. Perera, Progress in Quantum Electronics **48**, 1-56 (2016).

127. B. Aslan and R. Turan, Infrared Phys. & Technol. **43**, 85 (2002).

128. T. B. Bahder, Phys. Rev. B **41**, 11992 (1990).

129. A. G. U. Perera, S. G. Matsik, B. Yaldiz, H. C. Liu, A. Shen, M. Gao, Z. R. Wasilewski and M. Buchanan, Appl. Phys. Lett. **78**, 2241 (2001).

130. D. H. Zhang and W. Shi, Appl. Phys. Lett. **73**, 1095 (1998).

131. D. A. B. Miller, *Quantum mechanics for scientists and engineers*, 7th ed. (Cambridge University Press, New York, , 2014).

132. E. L. Wolf, in *Tunneling Spectroscopy: Capabilities, Applications, and New Techniques* (Springer US, Boston, MA, 1982), pp. 71.

133. S. C. Miller and R. H. Good, Phys. Rev. B **91**, 174 (1953).

134. R. G. Forbes and J. H. B. Deane, Proceedings of the Royal Society A: Mathematical, Physical and Engineering Science **463**, 2907 (2007).

135. Q. Yang, F. Fuchs, J. Schmitz and W. Pletschen, *Investigation of trap-assisted tunneling current in InAs/(GaIn)Sb…Sb superlattice long-wavelength photodiodes*. (2002).

136. L. Bürkle, F. Fuchs, E. Ahlswede, W. Pletschen and J. Schmitz, Phys. Rev. B **64**, 045315 (2001).

137. M. B. Reine, A. K. Sood and T. J. Tredwell, in *Semiconductors and Semimetals* (Elsevier, 1981), Vol. 18, pp. 201-311.

138. S. Gupta, S. Sethi and P. K. Bhattacharya, Appl. Phys. Lett. **62** (10), 1128-1130 (1993).

139. B. Kochman, A. D. Stiff-Roberts, S. Chakrabarti, J. D. Phillips, S. Krishna, J. Singh and P. Bhattacharya, IEEE J. of Quantum Electronics **39** (3), 459-467 (2003).

140. M. R. Matthews, R. J. Steed, M. D. Frogley, C. C. Phillips, R. S. Attaluri and S. Krishna, Appl. Phys. Lett. **90** (10), 103519 (2007).